Development and Characterization of Bioceramic Coatings for Medical and Dental Applications

By

Steven Mudenda

A thesis submitted in fulfillment of the requirements for the degree of

MAGISTER SCIENTIAE in the Department of Physics,

University of the Western Cape

Supervisor: Prof. Daniel Adams

Co-supervisor: Prof. James W Mayer

November 2007

Declaration

I declare that *Development and Characterization of Bioceramic Coatings for Medical and Dental Applications* is my own work, that it has not been submitted before any degree or presentation in any other university, and that all the sources I have used or quoted have been indicated and acknowledged as complete reference.

Full Name: **Steven Mudenda** Date: 14 November 2007

Signed

Keywords

Hydroxyapatite

Sol-gel

Crystallinity

Interface

Implantation

Micro-pattern

Adhesion

Densification

Microstructure

Cells

Abstract

"Development and Characterization of Bioceramic Coatings for Medical and Dental Applications"

Steven Mudenda

MSc. Thesis, Department of Physics, University of the Western Cape

Hydroxyapatite (HA), which is a natural component of bone tissue, is already being marketed as a coating for the metal shafts of hip implants as well as dental screws and other endoprostheses with the expectation of improved bonding to bone through osseointegration. Coatings prepared by the more widely used and commercial method, Plasma spraying technique suffer from poor adhesion or delamination from the substrate. The high temperatures involved in the preparation also results in a number of unstable decomposition phases compared to the more crystalline phase. The stringent demands on the *in vivo* performance requirements of such coating call for controlled surface roughness, porosity and adhesion strength to allow optimum in-growth of bone cells as well as for sufficient resorption resistance to guarantee the survival of the bioactive hydroxyapatite coating layer beyond the early stages of the healing process after implantation. Also, reduction of residual coating stresses, resulting mainly from differences in coefficient of thermal expansion between ceramic coating and metallic substrate, must be assured and carefully controlled to minimize the risk of cracking and delamination of the inherently brittle coatings.

The main purpose of the present research was to prepare and characterize HA coatings using low temperature sol-gel method with the specific aims of improving adhesion on both the HA/metal and HA/bone interface which has been reported as failure modes of implants. This was done through the use of plasma immersion ion implantation (PIII), and geometrically configured substrates (GCS). In the use of PIII to improve adhesion and densification, approximately 400 nm of Ti, Cr and V films were deposited on the Si substrates. Implantation of argon ions was performed on the metals and then HA (~400 nm) was subsequently deposited on the metal substrates and then fired at 850 ^{o}C. Using the tape test, an improvement in the adhesion was

observed on the implanted samples compared to un-implanted samples. Furthermore, the samples prepared by first depositing HA on the metal followed by implantation and then firing, showed using Rutherford backscattering spectroscopy, higher densification than the as-prepared samples

In the use of GCS to understand the effect of substrate geometry to HA microstructure evolution, Sol-gel derived hydroxyapatite (HA) was deposited on two different types of micro-patterned titanium substrates (sharp and tapered-edge channels) to obtain thin films of thickness of ~400 nm. Crystallinity was obtained by firing at temperatures ranging from 650-850^{o}C for five minutes. Rutherford backscattering spectrometry (RBS), X-ray diffraction (XRD) and Atomic force microscopy (AFM) were used to characterize the films.

Calculated crystallite sizes from XRD show that micro-patterned substrates contained larger grains than the un-patterned substrates. Furthermore, the tapered-edge channels contained larger grains than the sharp-edge channels. AFM results confirm and give visual results from XRD. Patterned substrates clearly showed great deal of roughness compared to the un-patterned substrates. The results further revealed that the inside of the channels contained larger grains than the outside of the channels. It is germane at this point to say that this finding elucidates one of the explanations from a materials science perspective why there is a preferential growth of cells on geometrically configured substrates. This is because the effect of the geometry on the underlying HA microstructure evolution correlates well with cell growth on micro-patterned substrates from other findings.

Acknowledgments

My profound gratitude goes to my supervisor Prof. Daniel Adams for bringing me into this interesting and promising area of research. His continuous encouragement, sagacious guidance and financial support during my study is greatly appreciated and treasured.

Dr Kenneth Streib for his advice during my study and also going over my thesis and advising me both in science and language. Your pickiness refined my write-up and is highly appreciated.

I also extend my thanks to the following:

The late Dr. TK Marais, Dr. Gerald Malgas now at CSIR, Theo Muller for guidance and helping settle during my first year, Mrs. Angela Adams for all the administrative work. I know I made too much trouble for you,

Dr. G Munyeme from the University of Zambia for introducing me to my supervisor and academic advice. Your advice is highly treasured and appreciated,

Dr. Basil Julies and Adrian Josephs from Electron Microscopy Unit for help and advice in SEM measurements,

People at the Materials Research Group, ITHEMBA LABS who include; Dr. Rudzani Nemutudi for expert advice in AFM measurements, Dr. Chris Theron (now at Element6) and Dr. Mira Topic for help in plasma immersion implantation, Przybylowicz WJ, Mesjasz-Przybylowicz and Msimanga Mandla for the help in PIXE, Lindi Vilakazi and Moses Mlungisi for E-beam deposition and Phillip Sechogela for RBS. Thanks for your patience and accommodating me in your busy schedules,

The Centre for Solid State Electronics Research (CSSER) and the Dept. of Chemical, Bio and Materials Engineering at Arizona State University, USA for the help in lithography and XRD respectively. Your help is greatly appreciated.

My friends, Jackson Phiri, Ian Siluyele, Nyumbu Chishwashwa, Kamohelo George Tshabalala, Ngcali Tile and Aaron Malape for valuable discussions,

Thanks also go to my family and Kasamba for their patience and encouragement. They have been waiting for this day for so long,

Financial support of the National Research Foundation of South Africa Canon Collins Education Trust for Southern Africa and the Mayer family is highly appreciated and treasured and

The ALMIGHTY GOD for the health, life and all the privileges I enjoyed during my study period. The list is endless. I thank you all.

TABLE OF CONTENTS

List of Figures

List of Tables

Chapter 1

Introduction

1.1 Current Trends and Socio-economic Effects

There has been an enormous increase in the number of patients requiring and receiving biomedical implants as a result of being subjected to unacceptable levels of trauma. Since the first successful Charnley Total Hip Joint (THJ) replacement in the 1960s was made, more than 500 000 joint replacements are performed each year in the United States alone with many more hundreds of thousands being performed worldwide with increasing frequency [1-3]. The same pattern prevails regarding the number of dental implant fixation. These figures are expected to rise due to demographic changes, such as, population increases and improvements in longevity. The increasing demand of hard tissue load-bearing replacements is the result of the wear and tear the hip and knee joints are subjected to during a human lifetime [4]. It is for this reason that techniques to regenerate and restore bone tissue to its functional state have become a clinical necessity [4]. However, the long term picture of endoprostheses is less promising because of implant failures.

1.2 Fixation of Implants and Inherent Failures

One of the challenges in orthopedic implantology is the fixation of implants to bone. Currently there are two clinically proven methods of fixation that are applied to improve longevity of implanted prostheses components. These are cemented fixations and cementless fixations [5]. Cementless fixations are achieved through mechanical fixation (morphological fixation), biological (porous ingrowth) fixation and bioactive fixation of surface-active interfacial bonding [5]. Mechanical fixation is accomplished via

mechanical interlock and press-fit [6]. However, despite their limited successes, they have their inherent failures. These failures are discussed in section 1.2.1 and 1.2.2 and 1.2.3.

1.2.1 Bone Cement Fixation

In the case of cemented implants, the prosthesis component is fixed in place in the bony implant bed using bone cement such as poly-methyl methacrylate (PMMA) [6]. The cement distributes the load evenly over a large area thereby reducing stress concentration on the bone. When this fixation is made, two interfaces arise; the bone/cement interface and the cement /implant interface. Studies have shown that failures of these implants are mainly due to loosening and occur at the interfaces. Statistics show that 10% of the failures for femoral prostheses are due to loosening at the cement/implant interface while 11% at the bone/cement interface [6]. Marx *et al* [7] reports that more than 80% of all clinical revisions are as a result of this loosening of the cemented implants. Histological and clinical studies by different researchers have shown that the beginning of the loosening process in femoral stems is found in the cement/implant interface (de-bonding) [7]. Capillary forces and diffusion cause water molecules to find their way into the bone cement and finally into the cement/implant interface thereby separating cement from the implant by hydrolytic degradation of the primary bond [7]. The inherent weakness of cement as a material and inclusion of pores contribute to the problem of loosening. Loosening, wear, fracture and late infection all contribute to implant failures. The chance of failure from each of these factors increases with time and each factor is additive and in many cases the complications are synergistic.

1.2.2 Cementless Fixation

Unlike the cement fixation, the prosthesis and the bone contact directly without cement. The following sections are brief descriptions of the three kinds of cementless fixation.

1.2.2.1 Mechanical Fixation

Mechanical (morphological) fixation applies to implants made of titanium and its alloys and non-bioactive coatings such as alumina. This morphologic fixation is intended to anchor implants in bone by mechanical interlocking and spread the load by increasing the surface area of the implant. Various combinations of grooves, ribs, holes and indentations have been investigated for improving morphological fixation as a means of increasing the surface area. In the press-fit implant (for the case of hip implants), the femoral canal is prepared so that the implant fits tightly within it [6]. It is an instantaneous mechanical fixation because immediate stability is achieved, though with subsequent problems. This has a mechanical problem which leads to cell necrosis because the bone (compact) is under stress as well as the trabecular bone because it is smashed at the base of the implant hence causing constant pain to the patient. These press-fit devices are also subject to creep and stress relaxation which can lead to remodeling of bone surrounding the implant hence bone loss.

1.2.2.2 Biological Fixation

This is a type of fixation which allows bone to bond directly to the implant system. This is a result of the ingrowth of bone tissue into porous implants or porous implant surfaces. The load can thus be transmitted from implant to bone over a large interfacial area and localized stress gradients can also be reduced [9]. Unlike the dormant cement/implant interface, the interface formed here is regarded “living” and remodels itself in response to stress variations over an indefinite period of time and interfacial loosening would be delayed or prevented [9]. It has however been reported that the interfacial strength decreases over a longer time interval than other fixation methods. This becomes a problem for young patients because they usually outlive the lifetimes of these implants and hence the need for revision. The concerns about the biological fixations include reduced strength and/or fatigue resistance of metal prostheses due to sintering of porous coatings and increased notch sensitivity of implants due to porous coatings [10].

1.2.2.3 Bioactive Fixation

Bioactive fixation requires implant materials to be bioactive so that they can establish bone bonding with living tissues by physio-chemical or cell-mediated biological processes. Currently there are two main bioactive materials for orthopedic and dental applications *viz*: Bioglass and hydroxyapatite (HA). Bioglass was invented by Hench in the 60's [11]. Surface-reactive Bioglass containing SiO_2, CaO, Na_2O and P_2O_5 is able to chemically bond with bone [6]. This type of bone/implant bonding is made possible by coating the metal shafts with hydroxyapatite (HA). These are then fitted in a well prepared femoral canal in the case of orthopedic implants or jaw in the case of dental implants. Bone then directly attaches to HA forming a strong bond. In this system two interfaces are created, the metal/HA interface and the HA/bone interface. Implant failures are reported to originate from the metal/HA interface. These implants then loosen in a similar manner as cemented implants.

1.2.3 Implant Failures

In addition to the failures discussed in the preceding sections, other probable failure mechanisms have been put forward. First, there is the problem of poor adhesion of metal substrates to ceramic coatings which leads to delamination and hence failure. This poor adhesion is made worse by residual stresses caused by differential thermal expansion between the ceramic coating and metal substrate introduced during manufacture.

Micromotion also occurs between the ceramic/bone interface leading to the formation of an undesirable fibrous connective tissue instead of bone ingrowth. Another problem is stress shielding. This happens when stress is not distributed evenly and in a way which is physiologically optimized such that the implant bears most of the load and less load to the bone. This results in loss of bone mass due to remodeling. There will be reduced activity of osteoblasts, cells which are responsible for bone formation and increased osteoclast action, cells responsible for bone resorption. This decrease in bone density subsequently leads to fracture and implant failure [2].

Because of these complications, the life span of implants has been compromised. Reports show that the average life span of an implant is about 10-15 years [1, 5].

Another point of importance in successful implant fixation and hence long term performance is to ensure bone ingrowth on the implant and hence interface homogeneity. This would greatly enhance fixation.

1.3 Concept of Biocompatibility

Materials incorporated into the human body must possess certain properties such that no negative effects occur with the living tissue. These materials which are designed to replace part or a function of the human body in a safe, economic, reliable and physiologically and aesthetically acceptable manner are called biomaterials [12]. These materials are said to be biocompatible. The concept of biocompatibility relates to various interactions on the cell and tissue levels a material is subjected to. By definition, biocompatibility is the ability of a material to perform with appropriate host response in a specific application [13].

1.3.1 Definition of Biomaterials and Tissue Interaction

The interaction of biomaterials with living tissue in increasing order of biocompatibility can be defined as follows [12]:

Incompatible Materials

These are materials that trigger negative reactions because of their tendency to release toxic substances to the body as well as the formation of antigens that may cause immune reactions like septic rejection, inflammation and other severe health consequences.

Biocompatible Materials

These materials release substances but not in toxic concentrations and these may only lead to benign tissue reactions such as formation of fibrous connective tissue or weak

immune reactions that often trigger formation of phagocytes. These materials are often called *biotolerant* because they are tolerated by the body tissues. These include austenitic stainless steels and bone cement consisting of polymethylmethacrylate (PMMA) etc.

Bioinert

These, neither release toxic constituents nor show a positive interaction with living tissue. The body responds to these materials by forming a non adherent capsule of connective tissue. Typical bioinert materials are titanium and its alloys, ceramics such as alumina, zirconia and titania, carbon and some polymers. This is why these materials are being used in the body for various applications.

Bioactive Materials

Bioactivity is defined as the property of the material to develop a direct, adherent and strong bond with the bone tissue. Bioactive materials show a positive interaction with tissues they come into contact with. This is in terms of differentiation of immature cells to become bone cells. In contrast to bioinert materials, bioactive materials allow a chemical bonding between them and bone at the interface. Bioactive materials are understood to have a very good affinity for bone growth mediating proteins. This leads to a bio-chemically mediated strong bonding osteogenesis. Typical bioactive materials are calcium phosphates such as hydroxyapatite (HA) and bioglass. The bioactivity of calcium phosphates is believed to be associated with the formation of carbonate HA (CHA). This is similar to the bone-like apatite [12]. This layer of CHA is believed to form on the surfaces of the implants when inside the living body. The bond to bone happens on this layer [12]. This effect was first observed by Hench and colleagues [14]. They observed that a calcium phosphate rich layer formed between the bioactive glass (silica based glass) and the bone tissue. In vitro, the bioactivity of materials has been attributed to the ability to form calcium phosphate on their surfaces when exposed to simulated body fluid (SBF). Titanium metal without any surface treatment is not bioactive but inert. When treated with NaOH however, a TiOH layer gives the metal implant the bioactive property [14]. This makes titanium a better choice than many other metals.

1.4 Biomaterials Used in Contact with Bone

1.4.1 Calcium Phosphate Bioceramics

As mentioned in earlier sections, biomaterials are materials used for making devices that can interact with biological systems for longer service with minimal failure. These should coexist with the tissue environment without any undesirable or inappropriate effect. Of the many biomaterials some of the most useful are the calcium phosphate ceramics. These are solid compounds of metals with non-metals. On their formation, a large amount of energy is released. These compounds are in a low energy state meaning that further spontaneous reactions are unlikely to occur, in other words, they are very stable. Because of this effect, ceramics are the most chemically and biologically inert of all materials [15]. Calcium phosphates (Ca-P) are highly biocompatible and due to their chemical similarity to natural bone, they have the ability to bond directly to bone [15, 16].

The calcium phosphate system is quite complex with many different possible phases interacting with each other. Some of these result from dissociation of one phase when subjected to high temperatures. The complete understanding of the kinetics and the thermodynamics of the system has not yet been fully realized [1, 17]. The calcium phosphates of biological interest are calcium salts or orthophosphoric acid [15]. There are basically seven principle calcium orthophosphates namely; monocalcium phosphate anhydrous (MCPA), dicalcium phosphate dihydrate (DCPD), dicalcium phosphate anhydrous (DCPA), octacalcium phosphate (OCP), β tricalcium phosphate (β -TCP), pentacalcium hydroxyl phosphate usually called hydroxyapatite (HA) and tetracalcium phosphate monoxide (TTCP) [15]. There are in addition many other phases possible and have been delineated by geologists and others [1]. Some have been included on the next page along with the above. Out of these seven principle calcium orthophosphates, the first four are too soluble to be used in biomaterials applications [15]. These resorb quickly when placed in a biological environment. Calcium phosphates are formed by calcining at high temperatures. The presence or absence of water indicates different phase

and hence the inclusion or exclusion of water vapor during sintering can alter the phase formation.

Section 1.4.1.1 gives a brief discussion of this family of the calcium phosphates [18].

1.4.1.1 Family of Ca-P

Below is the family of calcium phosphates [18, 19]:

Monocalcium phosphate anhydrous, MCPA, Ca $(H_2PO_4)_2$, is a highly soluble and acidic calcium phosphate. Due to its strongly acidic properties, it is incompatible with and nonexistent in an 'in vivo' environment (pH 7-7.4). Its Ca/P ratio is 0.50.

Dicalcium phosphate anhydrous (DCPA), $CaHPO_4$, and **dicalcium phosphate dihydrate**, **(brushite), (DCPD),** $CaHPO_4 \cdot 2H_2O$. Both are biocompatible, biodegradable, and osteoconductive materials. DCPD is a metastable compound and considered a precursor of HA in bone formation. They both have a Ca/P ratio of 1.00.

Octacalcium phosphate, OCP, $Ca_8H_2(PO_4)_6 \cdot 5H_2O$, is a metastable precursor of HA in teeth and bones with the Ca/P ratio of 1.33.

Alpha- and **beta-Tricalcium phosphate**, α-TCP, β-TCP, $Ca_3(PO_4)_2$, the two types have the same formula, but different crystallographic structures, with α-TCP more degradable than β-TCP. Both are widely used as bone substitutes as powders, granules, or blocks. Its Ca/P ratio is 1.50.

Hydroxyapatite, HA, $Ca_{10}(PO_4)_6$ $(OH)_2$, is an osteoconductive material, which is the most stable calcium phosphate at moderately acidic, neutral and basic pH. It is found in bone, dentine and teeth. It has a Ca/P ratio of 1.67.

Tetracalcium phosphate, TTCP, $Ca_4(PO_4)_2O$, is the most basic and soluble calcium phosphate below pH 5. TTCP is biocompatible, but poorly biodegradable. This has a Ca/P ratio of 2.00

Biphasic calcium phosphate, BCP, is a mixture of HA and β-TCP, which makes it more soluble compared to pure HA.

Oxyapatite, OHA, $Ca_{10}(PO_4)_6O$, is a decomposition or dehydroxylation product of HA. OHA is unstable. This is also apatitic. Its x-ray diffraction (XRD) is similar to OHA thus determining which structure is present in the film requires infra red (IR) techniques such as fourier transform infra red (FTIR) spectroscopy which determines atomic bonding. This technique is described in chapter 2.

Calcium-deficient hydroxyapatite, CDHA, $Ca_{10-x}(HPO_4)_x(PO_4)_{6-x}(OH)_{2-x}$, is similar to bone mineral but lacking the ionic substitutions. CDHA is a poorly crystalline material with a Ca/P ratio varying between 1.5 and 1.67; it is the main product of many calcium phosphate based cements.

Amorphous calcium phosphate, ACP, has various compositions, being especially involved in the *in vivo* biochemical transformations of calcium phosphate phases forming HA.

The phase diagram of a $CaO\text{-}P_2O_5$ system when in the absence of water vapor shows that the only calcium phosphate phases which form are tetracalcium phosphate and tricalcium phosphate [1]. It is also only in this system and in the presence of water that HA and dicalcium phosphate is formed. Figure 1.1 show the phase diagram of the $CaO\text{-}P_2O_5$ system in the absence of water vapor and Figure 1.2 is the system in the presence of water. In the precipitation reactions which lead to HA, more than one phase occurs. According to Ostwald's rule [19], which predicts that the least stable phase of highest solubility is formed preferentially during precipitation, it would be predicted that dicalcium phosphate dehydrate would form first. This phase dissolves quickly with

octacalcium phosphate being precipitated eventually. The dissolution of octacalcium phosphate will lead to the formation of HA and HA like phases [1, 20].

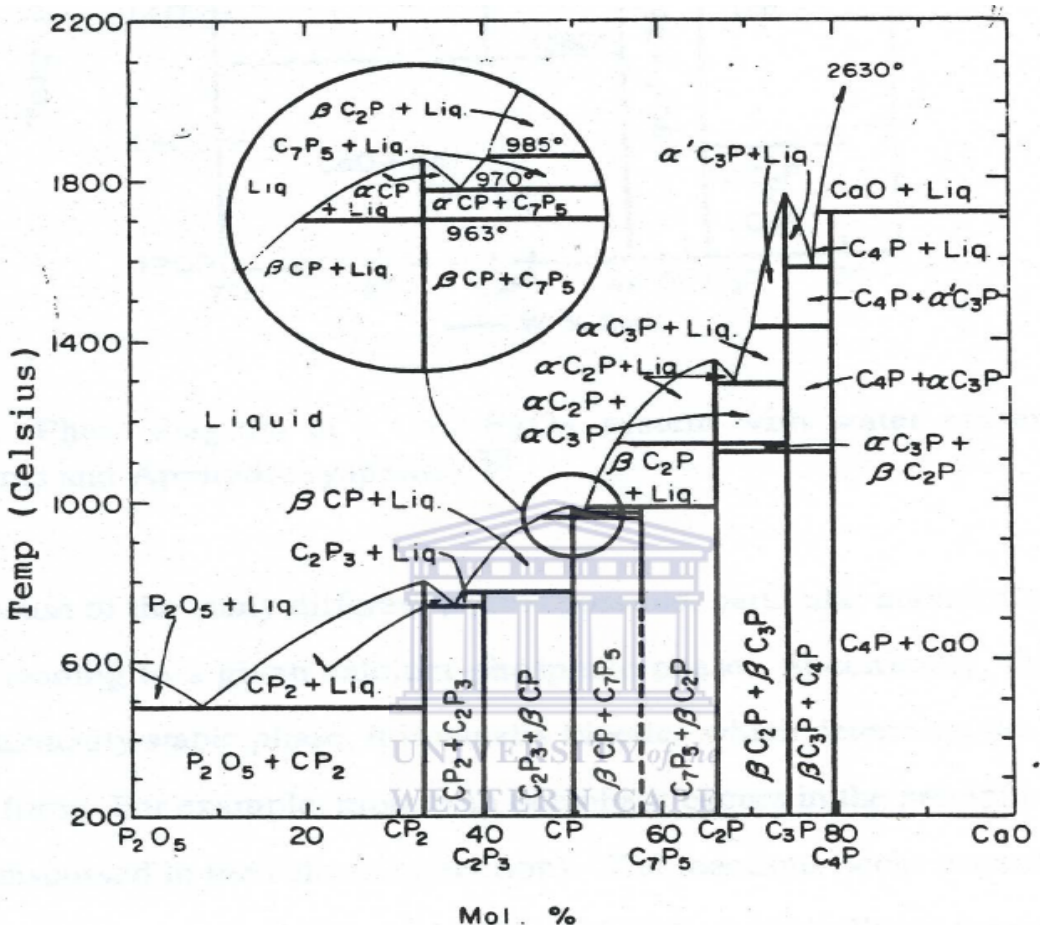

Figure 1. 1: Phase diagram of a CaO-P_2O_5 system in the absence of water [1].

In an aqueous environment at room temperature brushite (DCP) and HA are the two most thermodynamically stable phases. As to which phase will form, pH is the determining factor. At a pH < 4.2, DCP will be the predominant phase while the pH greater than 4.2 HA is the most stable phase. It follows therefore, that at physiological pH HA is the most stable. Many ionic substitutions may occur in HA, for example the hydroxyl group may be replaced by a fluoride, and the compound is then named fluorapatite. There can also be partial substitution of the OH^- and PO_4 groups with carbonate (CO_3) ions [21].

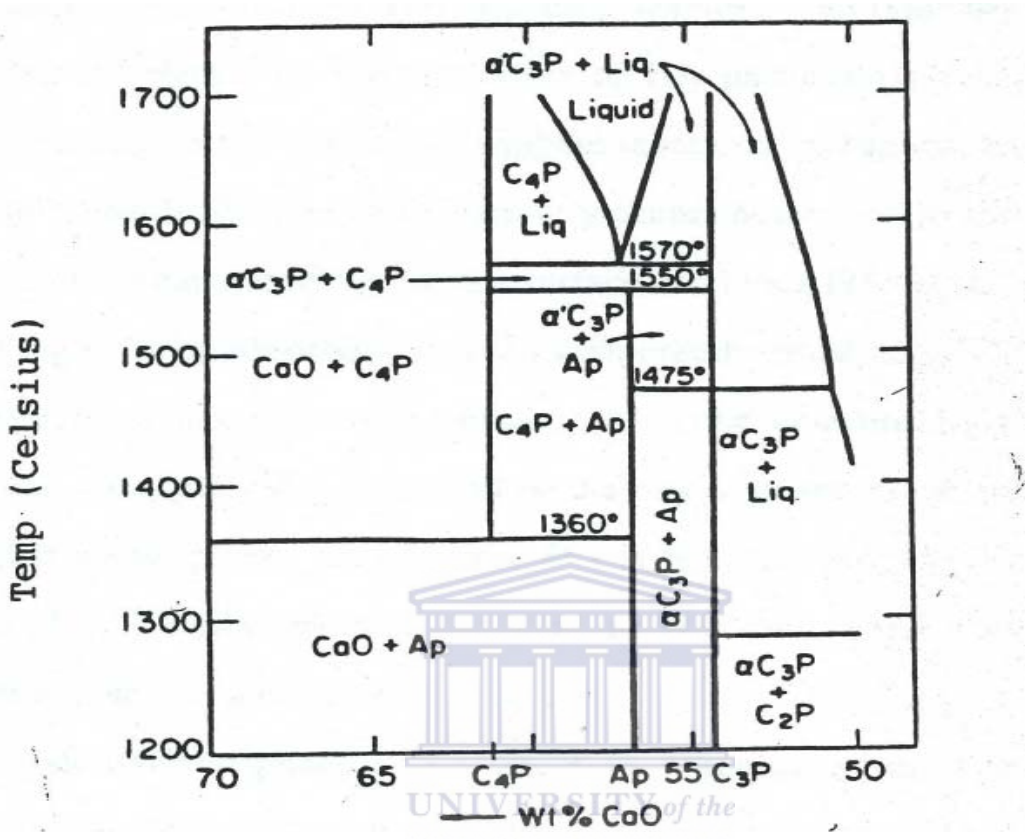

Figure 1. 2: Phase diagram of a CaO-P_2O_5 system in the presence of water [1].

Commercially available calcium phosphate systems formed by precipitation are amorphous in nature and are transformed to the crystalline apatite structure by firing. The firing is used to induce crystallinity because the more crystalline HA an implant coating contains, the more resistant the coating becomes to dissolution [22].

1.4.2 Most Used Calcium Phosphates

Beta-tricalcium phosphate and HA are the most commonly investigated calcium phosphates. They are the most frequently applied coatings for implants in the dental and orthopedic fields. A brief review of these is given in the next sections.

1.4.2.1 Tricalcium phosphate

The term tricalcium phosphate is used for any pure calcium phosphate with Ca/P ratio equal to 1.50. Tricalcium phosphate is a naturally occurring component of mineralized tissues. It is resorbed to a greater extent and more rapidly than HA [23]. It occurs in two forms namely α-TCP and β –TCP. β –TCP is a low temperature phase of TCP. It is currently used as bone graft replacement material. It has exceptionally good tissue compatibility, direct bonding to regenerated bone without intermediate connective tissue, faster bone regeneration and resorbability. Because of this resorbable characteristic, the porous TCP is regarded as an ideal material for bone substitutes that should degrade by advancing bone growth [24]. β –TCP is also considered as a major constituent of human dental calculus [25] and it is also found to occur in carious lesions [26]. β–TCP is however difficult to densify because high densification requires high temperatures but a sintering temperature beyond 1125 ^{o}C induces phase transformation to α-TCP which has a lower density than β –TCP (2.77 g cm^{-3} compared to 3.07 g cm^{-1} for β –TCP)[27].

Because of the rapid resorbability of TCP, HA is commonly used in the medical community because it is not readily bioresorbable in appropriate forms and it is therefore suitable for long term clinical applications. Due to these properties hydroxyapatite has been more thoroughly investigated than other calcium phosphate materials and is the one being studied in the present study.

1.4.2.2 Hydroxyapatite, HA

Hydroxyapatite, HA is a ceramic structure with chemical composition of $Ca_{10}(PO_4)_6(OH)_2$. Other apatites such as flourapatite, chlorapatite also exist, which all result from the substitution of the OH^- group with the respective halides. Hydroxyapatite has a hexagonal crystal system with a space group $P6_3/m$. In hexagonal close packing (HCP) the plane stacking sequence is ABABAB…, along the C axis. This type of arrangement results in continuous channels parallel to the C axis being formed and run the whole length of the crystal. In this system, 40% of the calcium ions occupy two-thirds of the channels while the remaining one-third is occupied by the hydroxyl ions

arranged in a chain. The remaining 60% of the calcium ions occupy the same channels as the hydroxyl ions [2]. Figure 1.3 shows the crystal structure of HA projected down the c-axis onto the basal plane.

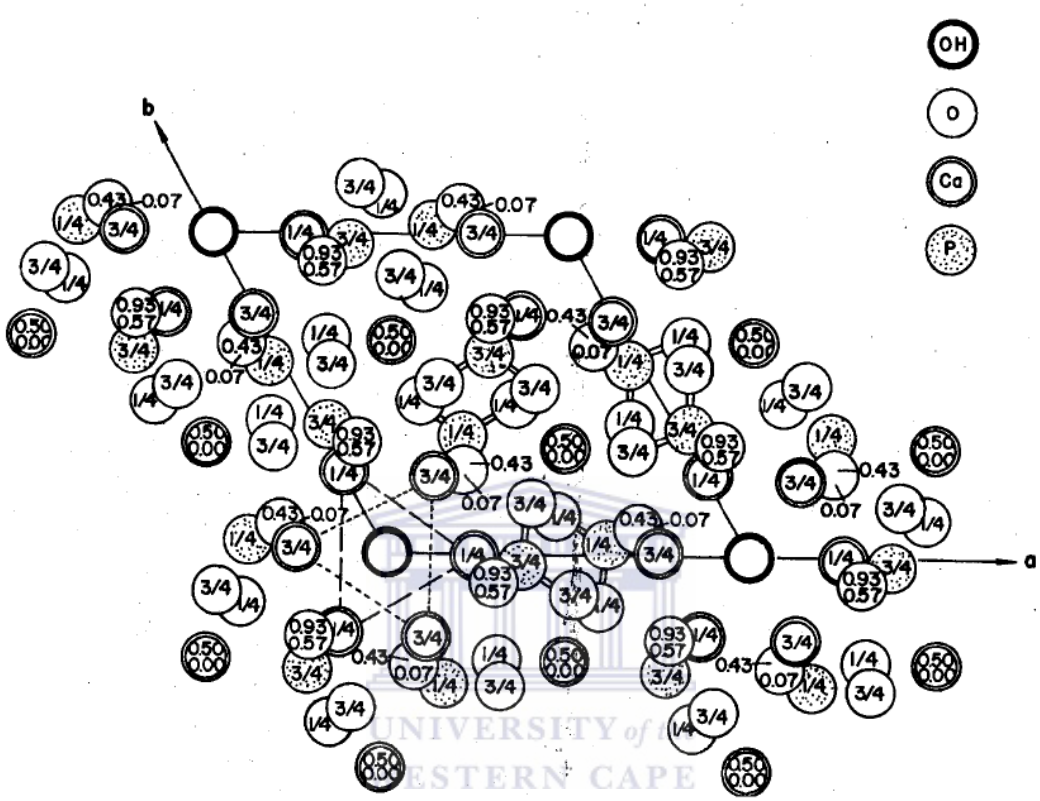

Figure 1. 3: HA structure projected down the c-axis onto the basal plane [10]

Hydroxyapatite is a ceramic with a melting point of 1550 ^{o}C with a calculated density of 3.219 g /cm^{3} [5]. Synthetic HA is a close approximation to the carbonated, calcium deficient apatite that comprises the mineral phase of bone [26]. Synthetic HA is classified as a polycrystalline ceramic since its material structure is derived from individual crystals that have been fused together by high temperature firing. Firing also induces densification by driving out the solvents and compacting the film.

XRD is one of the most recognized and accepted methods of determining the calcium phosphate phases which form. However, as has already been alluded to in the earlier sections, in cases where XRD doesn't give enough information FTIR gives refined

information on different phases. The standard XRD spectrum for HA is shown in the Figure 1.4.

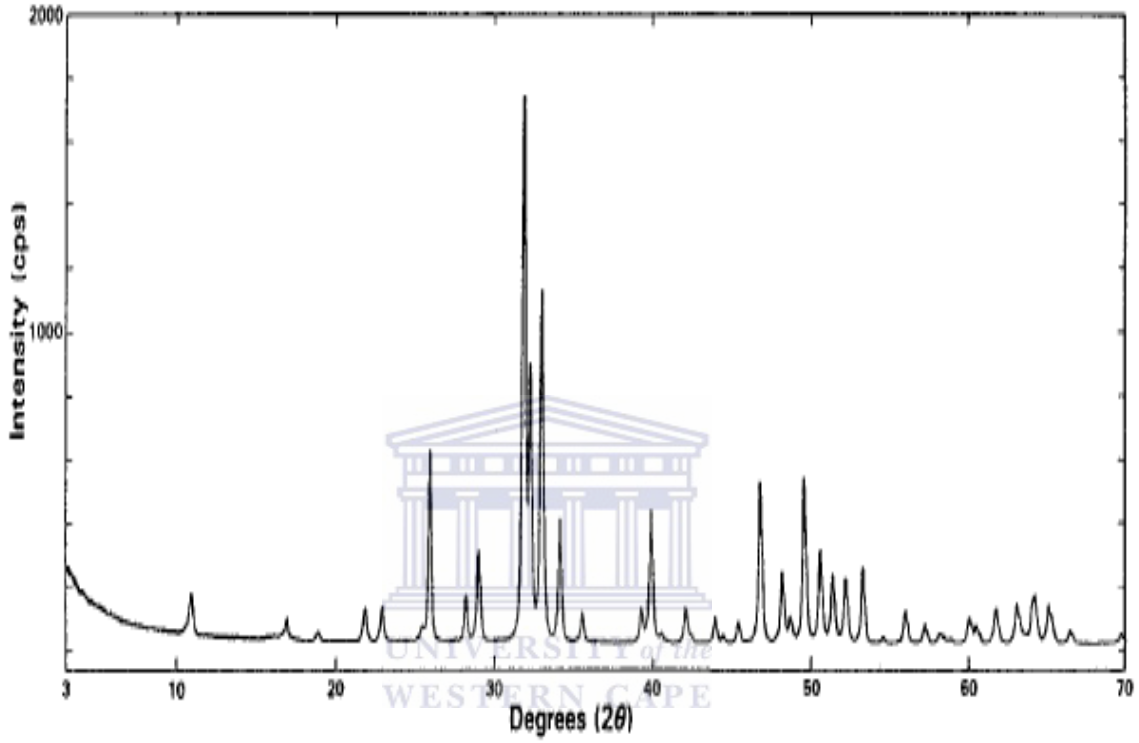

Figure 1. 4: Standard X-ray diffraction spectrum of hydroxyapatite [27].

In the past 30 years, HA has attracted much attention as an alternative material for autogenous free bone grafting [28-33]. It is the most prominent and widely investigated and used bioactive ceramic. HA typically exhibits excellent biocompatibility, bioactivity and, if porous, osteoconduction *in vivo*. Because of its similarity to bone, many workers have investigated its bonding properties to bone and have found that living bone can form a mechanical bond with sintered HA without forming a collagen interface layer which is usually found in other bioinert materials after implantation [34-37].

1.4.3 Mechanism of HA Bonding to Tissue

In spite of the fact that HA coated implants have gained wide acceptance in orthopedic and dental surgeries, the mechanisms leading to the formation of new bone on HA remains a matter of guesswork. Two hypotheses have been put forward in an attempt to explain this phenomenon as reviewed by Hao Wang [2]:

First hypothesis

The first hypothesis suggests that a granular afibrillar zone exists directly at the bone-implant interface and bone derived cells generate calcified afibrillar accretions that may act as a substratum condition layer for new bone formation. This extracellular matrix layer, which is less than a micron thick, contains calcium, phosphorous and sulphur. This is comparable to that of cement lines formed at discontinuities in natural bone [38].

This hypothesis has been confirmed by other workers and reviewed by Haibo Wang [28]:

- Immediately after implantation, calcium phosphate solid-solution equilibria are established by calcium and phosphorous ions released from the implant and surrounding environment.
- As a result of this, supersaturation of calcium and phosphorous is attained within the surrounding body fluid and the carbonate apatite crystallites reprecipitate epitaxially on the surface of HA [39].
- This surface which has now been modified is known to accommodate protein adsorption and cell adhesion more rapidly in particular cells associated with bone bonding [40].
- A cellular bone matrix from osteoblasts then appears on the HA surface producing a narrow amorphous electron dense band. Collagen bundles between this area and the cells can be seen with mineral crystals observed in this amorphous area.
- As the site matures, the bonding zone shrinks to a depth of less than a micron. The rising ratios of Ca/P (1.50 to 1.62) observed shows calcification process taking place [41]. After six months, mineralization on the implant site is comparable to the surrounding bone.

Despite all this however, the processes through which the amorphous layer matures to become bone remains unknown.

Second hypothesis

The second hypothesis suggests that an unmineralized collagen fiber matrix is first laid down at the implant-bone interface and subsequently is mineralized during osteogenesis. This fiber matrix layer is a thin area with potential to undergo remodeling or mineralization [20, 42].

The nature of the underlying processes involving the formation of these interfacial structures is still unknown and so it is not clear whether they are related to early bone formation.

1.4.4 Hydroxyapatite as a Coating

The major limitation of sintered HA however, is inferior mechanical properties. Although a compressive strength of up to 294 MPa of dense HA may be achieved, the tensile strength is only about 147 MPa which makes HA unsuitable for load bearing applications [13] despite its good bioactive properties. Table 1.1 shows the mechanical properties of HA and bone.

Table 1. 1 : Mechanical properties of HA vs Bone

	Elastic Modulus (Gpa)	Compressive Strength (MPa)	Tensile Strength (MPa)	Density (g/cm^3)
HA	40-117	294.00	147.00	3.16
Cortical Bone	7-30	100-230	50-150	1.02-1.25
Cancellous Bone	0.05-0.5	2-12	10-20	-

In order for HA to be applied in load bearing systems, it has been used as coatings on metals such as titanium and its alloys. This is an excellent combination because titanium

and its alloys have excellent mechanical properties and chemical stability in the physiological environment.

On the other hand, bone cannot attach or grow onto pure titanium when titanium is used on its own. In addition to this, the human body is a hostile environment to the metal and its alloys and so there is a risk or corrosion/ionization of the implanted device. There can also be toxic materials released from the surface of the metal which can be deleterious to the success of the implants. Therefore the difficulty of titanium and its alloys in bonding with living bone and the release of corrosion products into surrounding tissue immensely restrict their application. Therefore, HA when applied as a coating provides protection to the Ti alloy substrate against corrosion in the biological environment and acts as a barrier against the release of toxic metal ions from substrates into the living body. In order to combine the mechanical properties and stability of titanium with biocompatibility and bioactivity of HA, HA has been used as a coating. Figure 1.3 shows the application of HA coatings on implants.

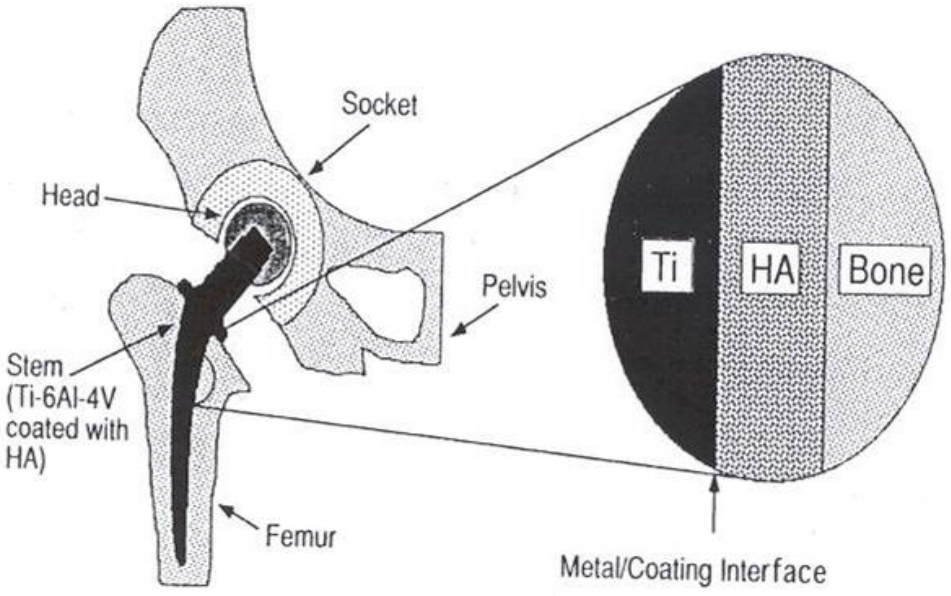

Figure 1. 5: A sketch of HA coating as applied in a hip implant [43].

1.5 Bone /Implant Interface

The interaction of bone with implant is quite complex. Therefore, the understanding of the events at the bone/implant interface and the effects biomaterials have on cells is quite important. Such understanding is essential in the development of strategies to optimally control osseointegration. All this stems from the hope of designing devices that would induce controlled, guided, predictable and rapid healing and enable better long term performance of implants. A comprehensive review of this interface can be found elsewhere [44]. Mechanical testing of various implanted biomaterials confirms that tissue/implant interfacial strength is the weakest compared to the intrinsic bone while micromotion at the interface is also detrimental to osseointegration [45]. Surface modification of implants is the most economic way of improving biological response instead of designing new and novel materials which can be quite expensive.

1.5.1 Surface Modification To Improve Biological Response

In the quest to obtain optimal biological response to implants, many efforts have been made in modifying implant surfaces though physicochemical methods, morphology and biochemical methods [46] as discussed below.

1.5.1.1 Physicochemical Methods

The physicochemical characteristics of interest in this work are surface energy, surface charge and composition. Surface energy has been shown to improve adhesion of interfaces [45]. Surface charge, positive or negative has also been observed to induce or promote bone formation [47]. Plasma ion implantation has been used to modify these physicochemical characteristics. In this process ions are implanted into the surface thus changing the surface charge as well as causing sputtering. This changes the surface energy. Depending on the type of ions, the chemical composition of the surface can be changed as well which can render a material bioactive. A brief review of the effects of

ion implantation will be given in section 1.6. Another physicochemical method is calcium phosphate coating. The implant is modified by coating it with HA and this imparts to the surface an affinity for bone cells. This method is the more widely used as was discussed in the previous sections.

1.5.1.2 Morphology

Surface morphology and roughness have been observed by a number of workers to influence cell and tissue responses through processes like attachment, proliferation, extra cellular matrix (ECM) synthesis, growth factor and cytokine production [48]. Contact guidance [49], which is the ability of an underlying substrate to direct or modify the response of a cell, is being investigated by many workers and it has been found that cells respond to different surface geometries depending on the width and density of the geometries. Osteoblast can also be attracted. V-shape, convex/concave and rectangular grooves have been investigated. All these have indicated a preferential alignment of cells as comprehensively shown by Adams *et al* as well as other investigators [50, 51]. Certain pattern dimensions attracted more cells than others indicating that there must be some optimal parameters which can influence maximum cell response. Contact guidance seems a promising mechanism as a complete understanding of this phenomenon will enable optimal manipulation of surfaces to obtain a predictable biological response.

1.5.1.3 Biochemical

This method uses the current understanding of biology and biochemistry to study cellular function and differentiation. Much has been learned about the mechanisms of how cells attach to implants [52]. Immediately upon implantation, proteins adsorb on the surface of the implant. This is where the cells subsequently attach, and hence bone formation begins. Therefore, the goal of these biochemical methods is to immobilize proteins, enzymes or peptides on the biomaterial to induce specific tissue response. As discussed in the previous section, one of the most used surface modifications was physicochemical methods through calcium phosphate coatings and more specifically HA coatings. However, with biochemical methods, organic compounds are used to affect tissue

response [44]. Cell adhesion molecules such as the sequence, Arg-Gly-Asp (RGD) have been used to control cell/material interactions because this has been identified to mediate cell attachment. However, this is not cell specific as other cells apart from osteoblasts can be attracted. More studies are needed of modified surfaces which are cell selective. Another method is to use biomolecules which have been shown to induce bone formation. The simplest way is to dip the implant into the protein solution before being inserted. In this case, the local cell populations must interact with the biomolecules and the concentration must be optimal [53]. Control of exposure and concentration, retention and release of biomolecules from the implant surface is another critical issue. However, it can be done by adsorption, covalent immobilization and release from coatings. Adsorption however, has little control over delivery, release/retention or orientation of molecules.

1.6 Plasma Immersion Ion Implantation

Bio-integration is the ideal outcome expected of any implant (biomaterial) [54]. The ideal biomaterial should have good physicochemical properties, while the surface should possess good biocompatibility as the environment inside the body is chemically and mechanically active. Interactions between the implanted materials and body tissues take place on the materials surface and, consequently biochemical responses and reactions depend on the surface properties. This means reactions that occur at the interface between the implant and host tissues should not induce negative effects such as releasing harmful chemical products or inducing deleterious effects, such as skin irritation, chronic inflammatory, and hypersensitivity responses [54]. As mentioned earlier, since implant/material interactions happen at the material surface, the design of biomaterials with good surface properties is of utmost importance. Materials can have adequate bulk properties, that is, good mechanical properties for load bearing applications, but their surface properties may not be optimal. In order for implants to function in the bio-environment, they must have both these properties especially in the orthopedic and dental applications. Since it is quite difficult to design materials with both these properties, the better approach is to fabricate materials with adequate bulk properties followed by a

specific treatment to enhance the surface properties. One method is through the process of Plasma Surface Modification (PSM). This is an economical and effective materials processing technique and has gained popularity in the medical field. This can alter a surface chemically and physically by altering the surface composition and microstructure. It can also synthesize a different structure, such as a thin film structure on the surface of the material via coating, grafting, thin film deposition and also the formation of a thin apatite layer on the surfaces after implantation of some species [54]. The latter is reviewed more in the next sections. There are many techniques falling under PSM which are used in the quest for better biomaterials. Among them are Plasma sputter and etching, Plasma deposition, Plasma spraying and more importantly, the technique in the present review, Plasma Immersion Ion Implantation (PIII). Before delving much in the review, a basic understanding of Plasma is needed and how it is produced and implanted.

Plasma

Plasma is usually called the fourth state of matter. Plasma can be described as a collection of electrons, singly and multiply charged positive and negative ions, neutral atoms, excited particles or radicals, electromagnetic radiation, molecules and molecular fragments [54]. The charged ions are typically obtained when gases are excited into energetic states by radio frequency (RF), microwave, or electrons from a hot filament discharge. An important feature of the plasma is that there is an equal number of positive and negative particles hence these are in a state of equilibrium and the sum of the positive and negative charges in a sufficiently large volume is equal to zero. The ions are bombarded onto the material surfaces and cause sputtering and displacements on the upper atomic layers causing atomic mixing. The penetration depth of ions in the low MeV range is of the order of microns [55]. The high density of ionized and excited species in the plasma can change the materials characteristics of the surface such as biocompatibility, mechanical and chemical properties, such as surface properties of normally inert materials like ceramics.

Sources of Plasma

Basically to produce a plasma, electron separation from atoms or molecules is needed. When an atom or a molecule gains enough energy from an outside excitation source via interactions with one another, ionization occurs. There are many types of plasma sources, the common ones being the gaseous, metallic and laser based sources**.**

A more comprehensive review of plasma sources can be found elsewhere [54].

1.6.1 Advantages of PIII

Plasma immersion ion implantation (PIII) was first investigated in the late 1980s as an alternative to extracted ion beams for achieving ion implantation of a sample [56, 57]. The advantages were identified to be the high flux of impinging ions and the conformal nature of the implantation, which reduced the need to rotate the sample during treatment. For this reason, with PIII, complex shapes can be implanted with equal amounts of ions to be implanted in all regions of the sample. This is opposed to line-of-sight (beam line) ion implantation which requires the substrate to be rotated to allow equal implantation amounts of ions in all regions. With PIII the sample is "immersed" in the plasma without having to be rotated. PIII utilizes the application of short, high-voltage pulses to a substrate immersed in plasma from which ions are drawn across a high voltage sheath and implanted into the substrate surface. As a competitor to beam line methods, PIII also has some disadvantages. These include difficulties accessing very high ion energies due to electric breakdown occurring across the plasma sheath and the larger energy spread of implanted ions, including a considerable proportion of low energy ions [58]. The low ion energies are due to the finite rise and fall times of the high voltage pulse. Recent simulation work on the sheath dynamics has shown that the major low energy ion contribution is due to the pulse rise-time despite the fact that it is usually shorter than the fall-time [58].

1.6.2 Review of the effects of PIII

The use of PIII to enhance surface bioactivity has attracted a lot of interest. Many researchers have worked on and improved the bioactivity of materials not normally bioactive [59]. Not only does PIII improve or enhance surface bioactivity but it can also improve surface corrosion resistance and hardness as well as anti-wear properties so that the materials can be more widely used clinically, especially as orthopedic implants with coupling where fretting is expected [59].

Paul K. Chu [59] reported enhanced bioactivity of silicon surfaces. He conducted plasma immersion ion implantation into single crystal wafers and observed improved biomimetic growth of apatite on surfaces in Simulated Body Fluids (SBF). All surfaces under investigation, hydrogen implanted and un-implanted, were immersed in the simulated body fluids for 14 days and 28 days. After 14 days of immersion in SBF, the un-implanted samples retained their smoothness while on the implanted samples ball shaped particles could be seen. After 28 days, the whole area of the surfaces was covered. On further investigations, X-Ray Fluorescence (XRF) indicated no calcium and phosphorus on the un-implanted silicon wafer after soaking for 14 days and 28 days. However, the XRF spectra for the hydrogen-implanted sample soaked in SBF for 14 days indicated the existence of surface calcium and phosphorus. After immersion for a further 28 days, more Ca and P were detected indicating the formation of a denser and thicker Ca-P layer. The Ca-P ratio was found to be between 1.33 and 1.58 for the 14 day immersion but with longer immersion time the ratio could increase to 1.67 indicating that Ca-P layer formed on the H-implanted silicon can crystallize to form Hydroxyapatite. X-Ray Diffraction showed peaks belonging to apatite on the implanted samples immersed in SBF. The broad peaks observed indicated that apatite particles were superfine and/or had low crystallinity.

Hanawa [60] showed that titanium implanted with Ca^{2+} using the conventional beam-line implantation is superior to un-implanted titanium from the perspective of bone conduction in terms of bioactivity. Baumann et al. [61] showed that apatite like layers are formed on the surface of titanium implanted with calcium and phosphorus after annealing at about 600^{o}C.

Another point of great importance is densification. A conventional method of densification of films is usually high temperature sintering. However, in HA systems, the process of sintering induces other phases which are not HA. Low temperature densification reduces this difficulty and this is done by ion beam densification. Levine and colleagues [62] studied the effect of ion implantation on Zirconia sol-gel thin films. Using 280 keV Xe ions a densification of up to 50 % could be achieved. Moriya also showed that sol-gel derived silica could be densified by ion implantation [63]. Lopatin and co-workers [54] irradiated 1 and 2 MeV Si^{++} on sol-gel derived HA deposited on silicon substrates and found that densification was 36 % of fully dense HA after drying at 620 ^{o}C for 3 minutes and 83 % after irradiation. Scratch testing also showed that implantation led to a substantial improvement in scratch resistance indicating that implantation improves adhesion. Lopatin used beam line ion implantation.

As opposed to the beam line ion implantation done by Lopatin and his group, the rationale of the present study is to investigate the capability of PIII on the densification of the hydroxyapatite films when plasma ions are implanted into the HA as well as the adhesion of the HA on the implanted metal.

1.7 Interface systems

The long term successes of implants depend on the integrity of the interfaces. The Bone/HA/Metal substrate system contains two interfaces, the Bone/HA (biological) interface and the HA/Metal (mechanical) interface. Clinical reports show that many implant failures originate at the HA/Metal substrate interface [55]. In the quest to improve the adhesion of the HA to metal substrates, many attempts have been made by different researchers. Among them, ion beam irradiation has been used. Studies have shown that it increases surface energy which is a characteristic for adhesion. This method can also be used to improve the adhesion by bombarding the coated surface with ions. The ions penetrate and cause an alloying effect between the surface coating material and the metal substrate. Another effect of implantation is the spontaneous formation of an apatitic layer on the titanium surface when immersed in simulated body fluid (SBF) after

implanting with species like Ca^{2+}, P ions and H_2O [12-13]. This treated substrate achieves a homogeneous interface with the coated HA hence providing a strong bond coat. As with the Bone/HA interface, the main aim is to ensure bone attachment onto the HA surface. As mentioned earlier in this chapter morphology and plasma implantation can be a solution.

1.8 Research Objectives

The goal of this research was to prepare and characterize HA coatings obtained from the low temperature sol-gel method with the specific aim of characterizing the crystallinity of the coatings, microstructure, and the adhesion of the coatings to metallic substrates.

With regard to characterizing the Bone/HA (biological) interface, earlier findings reveal that a combination of optimal surface topography and bioactive coatings can act synergistically to improve osteoblast adhesion and osteogenesis and so the report seeks to extend and investigate why cells behave that way from a materials science perspective. This thesis seeks to extend the work done by Adams *et al* [50].

Beam line ion implantation poses a practical problem when treating medical implants with complex shapes as these implants need to be rotated so that all the sides receive an equal flux of ions. However, in the plasma immersion ion implantation (PIII) process, the substrate is immersed in the plasma sheath and as a result it receives a uniform flux of ions on all its surfaces. With regard to the HA/Metal (mechanical) interface therefore, this thesis seeks to use PIII instead of beam line implantation as by Lopatin [55] to modify the HA coating in the quest to improve adhesion and achieve densification.

The objectives were achieved by answering the following questions,

- What effect does ion beam mixing via plasma immersion ion implantation have on HA density, microstructure and adhesion?
- With regard to the HA coating on the patterns, what are the effects of the substrate geometry on the evolution of HA microstructure?

1.9 Hypotheses

Two hypotheses to be tested are:

1. PIII will work like beam line implantation in improving adhesion and achieving densification.

2. Surface micro-topography provides a larger surface area for HA nucleation sites and is responsible for the fact that the constraints within the channels bring these sites close together. As a result the grains coalesce to form bigger grains. This would in effect increase surface roughness which is a crucial topographical feature in cell adhesion.

1.10 Thesis Outline

The rest of this thesis is organized as follows; Chapter 2 presents an overview of the experimental techniques used, the HA coating methods and the general sample preparation methods used in the experimental program. Chapter 3 focuses on the first objective of the thesis of investigating the effects of PIII on adhesion and densification on the mechanical interface. Results are given and discussed. Chapter 4 discusses the final objective of seeking information about cell response to a topographically modified surface from a materials science perspective. This will be done through the investigation of the evolution of HA microstructure on these substrates. Chapter 5 finally concludes the thesis and recommendations are given.

References

[1] Luptak K.A., "The Development of Hydroxyapatite Thin Films by Sol-Gel Processing", Masters' Thesis, Arizona State University, 1994

[2] Wang H., PhD Thesis, Massachusettes Institute of Technology, 2004

[3] Langer R., Vacanti JP, Tissue engineering .Science 260 (1993) 920-926

[4] Heimann R.B. , CMU.Journal (2002) Vol.1 (1)

[5] Hench L.L. "Cementless fixation in biomaterials and clinical applications," proceedings of the Sixth European Conference on Biomaterials, (ed. Pizzoferrato A., Marchetti P.G., Ravaglioli A. and Lee A.J.C) Elsevier Science Publishers, 1987

[6] Park B.J, Lakes R.S., Biomaterials an Introduction, 2nd edition, Plenum Press, New York and London, 1992

[7] Rudolf Marx, Hans J Erli, Othmar Paar, Fritz U Niethard, Michael Weber, and Dieter C Wirtz "Surface pretreatments for medical application of adhesion," BioMed. Eng. Online 2003, 2:15

[8] Jasty M., Maloney W.J., Bragdon C.R., O'Connor D.O., Haire T., and Harris W.H., "The initiation of failure in cemented femoral components of hip arthroplasties," J. Bone Joint Surgery (Br) 73 (1991)551-558

[9] Lu Xiong, PhD Thesis, Hong Kong University of Science and Technology, 2004.

[10] Cheng Zhang, PhD Thesis, Hong Kong University of Science and Technology, 2000

[11] Hench L., Spinter, R.J., Allen, W.C., Greenlee, T.K., "Bonding Mechanisms at the Interface of Ceramic Prosthetic Materials," Biomed. Mater. Sympo, 2 (1971) 117-141

[12] Williams D.F., Definitions in Biomaterials: Progress in Biomedical Engineering. 4th edn. Elsevier Science: Amsterdam; 1987: 67.

[13] Hench L.L., Wilson J., Larry L., An Introduction to Bioceramics, Singerpole, Hong Kong, World Scientific, 1993, pg 1-23 .

[14] Hench L.L., Bioceramics, J. Amer. Ceram. Society, 81 (1998)1705-1728

[15] Sanden B., "Fixation of Spinal Implants: Clinical and experimental studies on the effects of HA coating," PhD thesis, Uppsala university, 2001

[16] Thomas K.A., "Hydroxyapatite coatings". Orthopedics 17 (1994) 267-278

[17] Ravaglioli A. and Krajeweski A., Bioceramics: Materials, Properties and Applications, Chapman, London, 1992

[18] Rusu V.M., PhD thesis, Universitat Potsdam, 2004

[19] Ostwald W., Z. Phys. Chem. 22 (1897) 282

[20] Nancollas G.A., Lore M., Perez L., Richardson C., Zawacki S.J., "Mineral phases of calcium phosphates," The anatomical record, 224 (1989) 234-241

[21] de Groot K., "Chemistry of calcium phosphate Bioceramics" in CRC Handbook of Bioactive calcium phosphates, T. Yamamuro, L. Hench, J. Wilson (eds) CRS press, Boca Raton, 1990, pp 3-16

[22] Kay J.F., Dent. Clin. North-Amer 36(1992)117

[23] Jarcho M., "Calcium phosphate ceramics as hard tissue prosthetics." Clin. Orthop. 157(1981)259-278

[24] Koc N., Timcin M., Korkusuz F., Ceramics international 30 (2004)205-211

[25] Kani T., Kani M., Moriwaki Y., and Doi Y., "Microbeam X-ray diffraction analysis of dental calculus," J. Dent. Res. 62 (1983) 92-95

[26] LeGeros R.Z., Calcium phosphates in oral biology and medicine, Karger, Basel, New York, 1991

[27] Wei X., Akinc M., Key Engineering Materials, Vols 284-286 (2005) 83-86

[28] Wang H., PhD thesis, The Ohio State University, 2004

[29] Jarcho M., "Calcium Phosphate Ceramics as Hard Tissue Prosthetics. Clinical Orthopaedics and Related Research" 157(1981)259-278,

[30] Hulbert S.F., Bokros J.C., Hench L.L., Wilson J., and Heimke G., Ceramics in Clinical Applications: Past, Present, and Future. pp. 189-213 in High Tech Ceramics. Edited by P. Vincenzini. 1987.

[31] de Groot K., Klein C.P.A.T., Wolke J.G.C., and de Blieck-Hogervorst, J. Chemistry of Calcium Phosphate Bioceramics. pp. 3-15 in Handbook of Bioactive Ceramics, Vol.II. Edited by Yamamuro T, Hench LL, and Wilson J. 1990.

[32] Williams D.F., The Biocompatibility and Clinical Uses of Calcium Phosphate Ceramics. pp. 43-66 in Biocompatibility of Tissue Analogs, Vol.II. Edited by Williams D.F. 1985.

[33] Damien C.J., and Parsons J.R., "Bone Graft and Bone Graft Substitutes: A Review of Current Technology and Applications." J. Appl. Biomater. 2(1991)187-208

[34] Denissen H.W., and de Groot K., "Immediate Dental Root Implants from Synthetic Dense Calcium Hydroxyapatite." J. Prosthet. Dent. 42(1979) 551.

[35] Radin S.R, and Ducheyne P., "The Effect of Calcium Phophate Ceramic Composition and Structure on *In vitro* Behavior." II. Precipitation. J. Biomed Mater Res. 27(1993)35-45.

[36] Heughebaert M., LeGeros R.Z., Gineste M., Guilhem A., Bonel G., "Physicochemical Characterization of Deposits Associated With HA Ceramics Implanted in Nonosseous Sites." J. biomed. Mater. Res: Appl. Biomat. 22(1988)257-68.

[37] Jarcho M., Kay J.F., Gumaer K.I., Doremus R.H., and Drobeck H.P., "Tissue, Cellular and Subcellular Events at a Bone-Ceramic Hydroxyapatite Interface." J. Bioengin. 1 (1979)79.

[38] Davies J.E., Chernecky R., Lowenberg B., Shiga A., Cells and Materials 1:1 (1991)3-15

[39] Radin S.R., Ducheyne P., J. Biomed. Mater. Res, 27(1993)35-45

[40] Heughebaert, LeGeros M., R. Z., Gineste M., Guilhem, A. and Bonel G., J. Biomed. Mater. Res.: Appli. Biomat. 22(1988)257-268

[41] Jarco M., J. Bioengineering 1 (1977)79

[42] Steflik D.E, Corpe R.S., Lake F.T., Young T.R., Sisk A.L., Parr G.R., Hanes P.J., Berkery D.G., "Ultrastructural analyses of attachment (bonding) zone between bone and implanted biomaterials," J. Biomed. Mater. Res. 39:4(1998)611-620

[43] Levine T., Schroer A., Pizziconi V., Suchicital C., Dey S.K., Mayer J.W., Nastasi M. and Koeneman J., "Ion-Beam Processing of Hydroxyapatite Sol-Gel Thin Films on Bone Prosthesis," presented at International Workshop of Plasma-Based Ion Implantation, Madison, WI, 1993

[44] Puleo D.A., Nanci A., "Understanding and Controlling the Bone-Implant interface," Biomaterials 20 (1999) 2311-21

[45] Baier R.E., Surface properties influencing biological adhesion. In: Manly RS, editor. Adhesion in biological systems. New York: Academic Press, 1970 pg 14-48.

[46] Schuler M., Trentin D., Textor M., Tosatti S.G.P., "Biomedical interfaces: Titanium surface technology for implants and cell carriers," Nanomedicine 1(4) (2006) 449-463

[47] Krukowski M., Shively R.A., Osdoby P., Eppley B.L., "Stimulation of craniofacial and intramedullary bone formation by negatively charged beads." J Oral Maxillofac Surg 48(1990)468-75.

[48] Boyan D. Barbara, Christoph H Lohmann,, David D Dean,, Victor L Sylvia,, David L Cochran,, Zvi Schwartz. Annual. Rev. Mater. Res 31 (2001) 357-71

[49] Weiss P., "In vitro experiments on the factors determining the course of the outgrowing nerve fiber," J. Exp. Zool. 69 (1934) 393-418

[50] Adams D., Smith R.D., Malgas G.F., Massia S.P., Alford T.L., Mayer J.W., " The influence of Geometrically Configured Sol-Gel Derived Hydroxyapatite Substrates on Osteoblast Response," Key Engineering Materials 284-286 (2005)569-572

[51] den Braber E.T., de Ruijter J.E., Ginsel L.A., von Recum A.F. and Jansen J.A., Biomaterials 17 (1996) 2037- 44

[52] Albelda S.M., Buck C.A., "Integrins and other cell adhesion molecules." Faseb J 4(1990) 2868-80.

[53] Lucas P.A., Syftestad G.T., Goldberg V.M., Caplan A.I., "Ectopic induction of cartilage and bone by water-soluble proteins from bovine bone using a collagenous delivery vehicle." J Biomed Mater Res 23 (1989)23-29.

[54] Chu P.K., Chen J.Y., Wang L.P., Huang N., Materials Science and Engineering R 36 (2002) 143-206.

[55] Lopatin C.M., Alford T.L., Pizziconi V.B., Kuan M., Laursen T., Nucl. Instr. And Meth. In Phys. Res. B 145(1998)522-531

[56] Conrad J.R., Radtke J.L., Dodd R.A., Worzala F.J., J. App. Phys. Letters, 62(1987)4591.

[57] Tendys J., Donnelly I.J., Kenny M.J., Pollock J.T.A., J. App. Phys. Letters, 53(1988)2143

[58] Kwok D.T.K., Bilek M.M.M., McKenzie D.R. and Chu P.K., J. App. Phys. Letters, 82:12 (2003)1827-1829.

[59] Paul K. Chu, "Bioactivity of Plasma Implanted Biomaterials," Nucl. Instr. And Meth. In Phys. Res. B 242(2006)1-7

[60] Hanawa T., Kamiura Y., Yamamoto S., KohgoT., Amemiya A., Ukai H., Murakami K., Asaoka K., J. Biomed. Mater. Res. 36 (1997)131.

[61] Baumann H., Bethge K., Bilger G., Jones D., Symietz I., Nuclear Instruments & Methods in Physics Research. Section B, Beam Interactions with Materials and Atoms 196 (2002) 286.

[62] Levine T.E., Keddie JL, Revesz PR, Mayer JW and Giannelis J, American ceramics society 76 (1993)1369

[63] Moriya N., Diamand Y.S., Kalish R., J. Appl .Phys. Letters, 57 (1990) 108

Chapter 2

Experimental Techniques

2.1 Introduction

The interaction of implant and host bone is very complex, and controlled by many factors, such as site of implant, techniques of clinical implanting as well as the physical and chemical properties of the implant material [1]. In order to fully understand the interaction mechanism and process of implants and host bone, critical characterization of implant materials is essential. This chapter begins with the characterization techniques and procedures performed in the experiments to characterize the samples under investigation. The characterization techniques discussed are, Rutherford Backscattering Spectrometry (RBS) for composition and depth profiles, x-ray diffraction (XRD) for phase analysis and crystallinity, scanning electron microscopy (SEM) and atomic force microscopy (AFM) for surface morphology, tape test for adhesion properties. The chapter concludes with the experimental procedures involved.

2.2 Characterization Techniques

2.1.1 Rutherford Backscattered Spectrometry

Rutherford backscattered spectrometry (RBS) is a fast, direct and non destructive ion beam technique for determining elemental depth profile and composition. A particle accelerator is used to direct a mono-energetic ion beam typically a few hundred keV to a few MeV onto the sample under study. The most commonly used beam in RBS is ^4He (alpha particle) with energies of 1-4 MeV. Protons (H^+) are also used typically with energies between 100 keV and 2 MeV [2]. The range of depth accessible by this method (RBS) is about 1-10 microns, beyond which complications due to straggling effect results in loss of sensitivity and depth resolution. The elastically backscattered particles are detected using a solid state detector. The energy of backscattered particles can be determined with a resolution of a few keV in the case of surface barrier detector.

Collisions between impinging ions and target atoms can be described with the Rutherford formalism if the distance of closest approach is neither so small that nuclear reactions are possible nor so large that electronic screening must be taken into account. If these conditions are fulfilled, collisions are elastic and the energy loss of the projectile is entirely determined by its mass m_1,the mass of the target atom m_2 and the scattering angle θ, taken in the laboratory system of coordinates or geometry system. There are three basic concepts which are of importance when using RBS, each related to an analytical capability of the method, *viz,*

- Kinematic factor, K, for mass analysis
- Differential scattering cross section, for quantitative analysis and
- Energy loss of a particle, for depth profiling (analysis).

The geometry system used in RBS is shown in Figure 2.1.

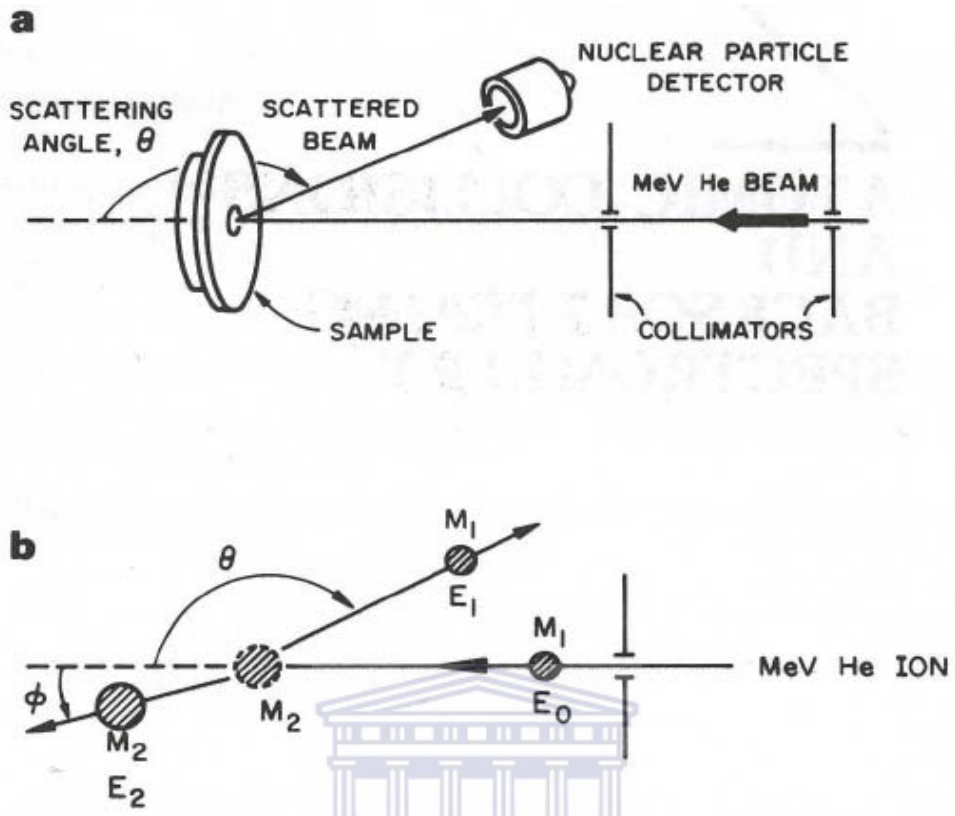

Figure 2.1: (a) Schematic of the experimental setup for Rutherford backscattering, (b) Schematic representation of an elastic collision between a projectile of Mass M_1 with energy E_0 and a target atom of mass M_2 initially at rest [3].

2.1.1.1 Kinematics

As shown from the above geometry in Figure 2.1.a, the energy E_1 of particles scattered from the target atom M_2, is related to the incident energy E_0 through the kinematic factor, K, where

$$K = \frac{E_1}{E_0} = \left[\frac{M_1 \cos\theta + (M_2 - M_1^{\,2} \sin^2 \theta)^{\frac{1}{2}}}{M_1 + M_2} \right]^2 \qquad (2.1)$$

Using the kinematic factor the mass of the target atom from which the scattering event took place can be calculated. From the above Equation, (2.1), it is evident that the mass separation is best for large θ and large M_1. This formula has simple forms at $\theta=90^0$ and 180^0.

$$K(90^0) = \frac{M_2 - M_1}{M_2 + M_1} \tag{2.2}$$

And

$$K(180^0) = \left(\frac{M_2 - M_1}{M_2 + M_1}\right)^2 \tag{2.3}$$

Hence from the foregoing, the mass of the scattering atom determines the energy of the backscattered ion.

2.1.1.2 Differential Scattering Cross Section

One of the main advantages of the RBS technique is the ability for quantitative analysis without standards [3]. This is because backscattering takes place with a known cross-section, σ, which is given by the Rutherford formula,

$$\frac{d\sigma}{d\Omega} = \left[\frac{Z_1 Z_2 e^2}{2E_0 \sin^2\theta}\right]^2 \frac{\left[\cos\theta + (1 - (\frac{M_1}{M_2}\sin\theta)^2)^{1/2}\right]^2}{\left[1 - (\frac{M_1}{M_2}\sin\theta)^2\right]^{1/2}} \tag{2.4}$$

Where Z_1 and Z_2 are the atomic numbers of the projectile and target atoms respectively and Ω is the solid angle subtended by the detector. The differential scattering cross-section above is related to the scattering yield and is used for quantitative analysis. From Equation 2.4, it can be seen that the sensitivity is greatest for atoms with large Z and small scattering angles [3].

The total number of atoms detected can be extracted from the yield, Y,

$$Y = \sigma(\theta)\Omega Q N_s \tag{2.5}$$

Where Q is the total number of incident particles and N_s are the observed projected atoms as measured in atoms/cm^2.

2.1.1.3 Energy Loss and Depth scale

When ions penetrate a solid they lose energy through electronic interactions. The rate of loss, $\frac{dE}{dx}$, or stopping power is used to determine the layer thickness. The stopping power depends on the composition of the sample and is a relatively slowly varying function of the projectile energy [3]. At small depths the loss follows a linear relation, with depth, t, and the loss ΔE can be expressed as,

$$\Delta E = [S]t \tag{2.6}$$

Where, [S], is the backscattering energy loss factor. When the thickness being probed becomes large, the equation becomes more complex, because there will be losses on the inward path as well as the outward path due to electronic stopping.

Below is a sketch of how the energy is lost.

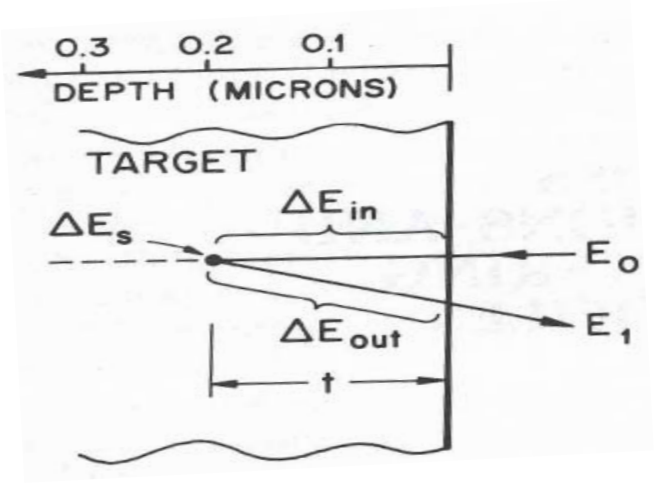

Figure 2.2: Diagram depicting energy loss of the probing beam [3].

The loss of energy by a projectile which was backscattered by the target atom at a depth t is

$$\Delta E = [S]t = \left[\frac{K}{\cos\varphi_1} \frac{dE}{dx}\bigg|_{E_0} + \frac{1}{\cos\varphi_2} \frac{dE}{dx}\bigg|_{E_1} \right] t , \tag{2.7}$$

where the incident and scattered angles are, respectively, φ_1 and φ_2 with respect to the normal of the target surface. From Equation 2.7, determination of ΔE allows one to obtain the depth profile. A more comprehensive review can be found elsewhere [2-4].

2.1.1.4 Experimental Considerations

In summary, for experimental consideration, most RBS measurements are carried out with H and He ions. Heavier ions such as Li or B can be used to gain better mass resolution, but due to poor detector resolution for such ions, this is applied only in special cases. Below are typical conditions for RBS measurements:

- Targets are usually set normal to the incident beam, except when 90^o detection is required, in which case the target is set to some angle sufficient to prevent blocking of detector by the frame and to minimize the straggling effect.
- The particles are detected using surface barrier detectors set between 90^o and 175^o. For maximum mass resolution, the angle must be close to 180^o, which can be achieved with annular detectors.
- The beam energy is usually chosen to avoid nuclear reactions, which result in deviations from the Rutherford cross-section. However, these can be corrected by means of relative measurements against suitable standards, since the other quantities governing the yield are unaffected by nuclear effects.
- Low currents (below 1 nA) are desirable to ensure accurate results due to secondary electron emissions from the target and leakage currents in the beam integration circuits [2].

In summary, Rutherford backscattering spectra give information on the mass and on the depth of a target atom. This is advantageous because it allows the determination of the atomic composition of the target as a function of depth.

2.1.2 Scanning Electron Microscopy

Scanning electron microscopy is a powerful characterization tool in the analysis of surface structures of materials. The variety of samples which can be studied using surface analysis is immense, ranging from atomically flat semiconductors grown in situ to compressed powders including ceramics. In the analysis of bio-ceramics, scanning electron microscopy (SEM) is used among other things to check porosity of the material, for example, concentration, size and structure of the pores which determine the mechanical properties of these materials. So from the simple SEM results it is possible to make a rough estimate of how dense a material is. The SEM uses electromagnetic lenses to form a de-magnified image of the electron source. This fine probe of electrons is scanned over a small rectangular area across the sample and one of a number of possible signals arising from the electron-specimen interaction (i.e.; backscattered electrons, secondary electrons, photon emission, auger electrons, *etc*.) is detected, amplified, and used to modulate the intensity of a cathode ray tube image, which is scanned at the same rate as the electron probe.

2.1.2.1 Signals and Detectors

When an electron is incident on the surface of a thick specimen, several signals can be detected. The incident (primary) electron results in ionization of atoms along its path in the solid, which in turn can result in the ejection from the surface of secondary electrons, very close to the incident beam position. These have energies from 0-20 eV, and can be attracted to a positively charged detector with high efficiency [2]. The primary electrons can be deflected through large angles, and hence emerge as backscattered electrons from a region surrounding the incident probe. By placing a large annular detector below the

final lens, facing towards the sample, a proportion of the backscattered electron (BSE) signal can be collected. The resolution of the BSE image is typically of the order of 0.1-1 μm [2], being determined by the volume within the sample from which most of the detected BSE signal comes. Of the two signals (SE and BSE) being discussed here, SE signals show fine details of topography while BSE show some topographical features at the expense of contrast. BSE signals depend on the elemental atomic number in the analyzed region with the brighter signal corresponding to higher atomic number elements. One of the major advantages of operating at low beam energies is the reduction in the interaction volume meaning the depth of penetration for lower beam energies is fractions of a micrometer. Monte Carlo calculations show that at 10 keV the maximum depth penetration of the beam in Si is about 1 μm, while at 1 keV it is close to 0.03 μm [2]. This therefore suggests that SE image at lower energies (about 1 keV) gives better representation of the surface detail. Another advantage of low kV operation is that the secondary electron yield is approximately inversely related to beam energy. Furthermore, an electron energy of around 1 keV when used would cause no charging and thus no metal coating of samples is required, thus fine surface detail is not obscured which is very advantageous especially when analyzing a bio-ceramic topography.

SEM can also be used to determine osseointegration percentage, for example, the contact length of bone-implant interface [5, 6]. While SEM can qualitatively describe the surface topography, it does not provide the quantitative values of the surface roughness. Profilometry can conveniently be used to quantify the topographical parameters.

2.1.3 X-Ray Diffraction (XRD)

X-Ray Diffraction (XRD) is a powerful characterization tool which uses x-rays as the probing source. It is very essential in the characterizing of materials because it can determine the phase and crystallinity of a material. Calcium phosphates (Ca-P) or hydroxyapatite (HA) coatings need to be sintered before being implanted *in vivo* to drive off solvents and densify the material in the process. Sintering also induces crystallinity. Crystallinity is very important because when a material is placed in vivo it prevents rapid

resorption of the coating in the bio-environment as compared to when it is amorphous. This is important because this will give time for the healing process. Therefore curing is indispensable. However, in the process of sintering other phases may result as a consequence of sintering at high temperatures. Therefore is necessary to identify the unwanted phases.

XRD has a limitation however, as most of the peaks for the other phases of HA such as CaO, Tricalcium phosphate, OHA and Tetracalcium phosphate *etc,* exactly coincide with the HA peaks hence it is unable to identify which one is which. Fourier Transform Infra Red Spectroscopy (FTIR) offers a complete way to identify these phases by identifying the different bonds. A comprehensive review of FTIR can be found elsewhere.

2.1.3.1 Theory of Operation of XRD

The operation of X-Ray Diffraction is based on Bragg's law which is

$$n\lambda = 2d\sin\theta \qquad (2.8)$$

Where,

$\lambda =$ incident wavelength

$d =$ spacing between atomic planes in the crystalline phase

$\theta =$ diffraction angle usually in terms of 2θ angle and

$n =$ integer,

A collimated beam of x-rays is directed on the sample. A crystalline material will always have planes which will diffract the x-rays. The diffraction depends on the crystal structure and on the wavelength. The diffraction is a constructive interference of the radiation from successive planes and occurs when the path difference is an integral number n of wavelengths. This diffraction happens at a unique angle and so the angle and sometimes the intensity becomes the signature of that crystalline material. Bragg's

law is a consequence of periodicity of the lattice and this effect is only evident on crystalline materials.

The intensity of the diffracted x-rays is measured as a function of the diffraction angle and specimen orientation. The pattern can be used to identify the crystalline phase, structural properties such as stresses and strains, epitaxy and the size of the crystallites and orientation.

The crystallite size can be determined by using the Scherrer equation 2.9. An assumption is that the crystals must be smaller than 100 nm [7].

$$d = \frac{0.9\lambda}{\Delta_{2\theta}\cos\theta}, \tag{2.9}$$

where d is the crystallite size, λ = 0.15404 nm for wavelength of Cu k_α X-rays and $\Delta_{2\theta}$ the full width at half maximum (FWHM) at angle 2θ in radians.

2.1.4 Atomic Force Microscopy (AFM)

This is a very high resolution type of scanning probe microscopy with lateral resolution ranging from atomic levels to 1 nm and a vertical resolution of 0.01 nm [8, 9]. It is a versatile imaging probe in that it can nondestructively image surfaces of solid conductors, semiconductors, insulators and surfaces in liquid media. The AFM principle is similar to contact Profilometry but works by having a microscale cantilever with a nanometric tip (probe) at its end that is used to scan the specimen surface. The tip is very sensitive to any surface changes. Depending on the situation, forces measured in AFM include mechanical contact force, Van der Waals forces, capillary forces, chemical bonding, electrostatic forces and magnetic forces etc. Basically the inter-atomic forces between surface atoms and the atoms on the tip will deflect the cantilever beam. The deflection is measured using a laser spot reflected from the top of the cantilever into an array of photodiode detectors. The topography of the surface therefore can be mapped to atomic resolution in three dimensions by monitoring with this laser spot. The magnitude of the

deflection depends upon short range attractive and repulsive interaction forces for a given distance between surface atoms and tip atoms. The Figure 2.3 below shows a sketch for AFM.

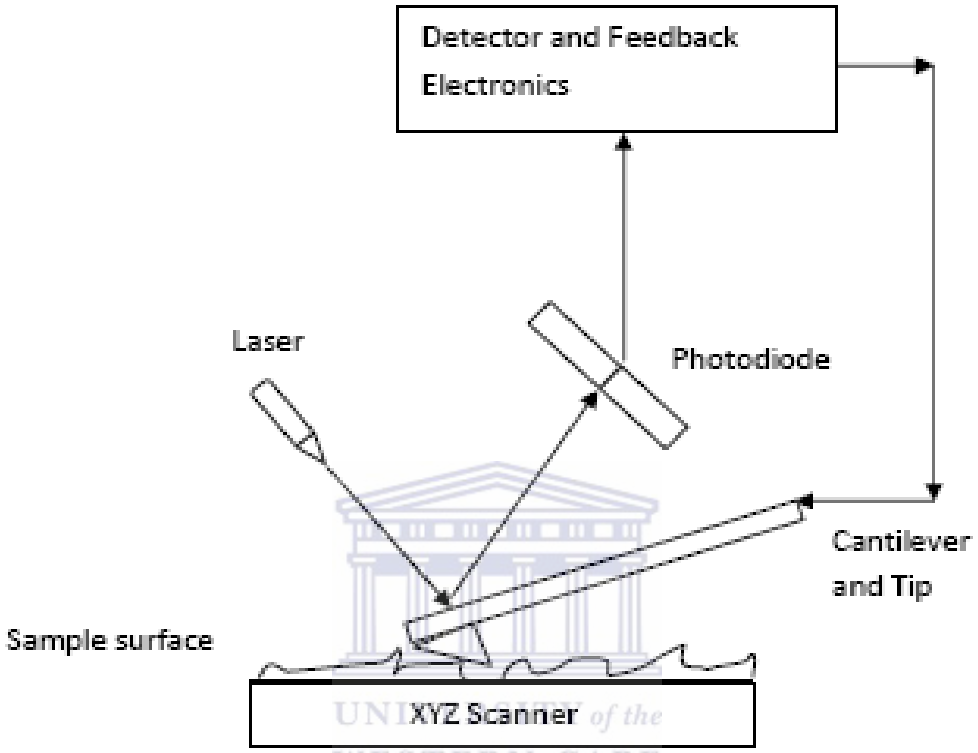

Figure 2.3: Schematic of Atomic Force Microscopy

2.1.4.1 Force-Distance measurements

Besides imaging, AFM can also be used to obtain Force-Distance curves. In this application, the tip is approached towards and retracted from the surface and the static deflection of the cantilever is monitored as a function of piezo displacement. These measurements have been used to evaluate nanoscale contacts, atomic bonding, van-der Waals, hydration forces in liquids and single molecule stretching and rupture forces [9].

AFM is therefore a useful technique which does not require special conditions like expensive vacuum but can work in ambient environment including liquid environments. This makes it possible to study biological macromolecules and even living organisms.

Information on the surface roughness, grain size and 3-D topology can be obtained by AFM.

2.2 Experimental procedures

2.2.1 Substrate preparation

Since the experimental program was based on studies of the properties of hydroxyapatite (HA) deposited on metal and alloy substrates, samples were prepared by depositing metals on the silicon samples. Silicon substrates were used because they are rigid, easy to cleave into smaller pieces and more importantly do not interact with HA coatings. In the experimental program therefore, in order to mimic the real conditions and materials involved in medical implants, where HA is used as a coating, the experiment involved electron-beam depositing the metals on the Si substrates of single crystal silicon of <100> orientation, in a vacuum of 1 x 10^{-7} kPa or better. The procedure follows in the next sections.

2.2.2 Wafer Cleaning

A clean surface means the bulk material extends all the way to the surface without any change of chemical composition and with no foreign material attached to the surface. Solvent cleaning is usually employed for the removal of fats, oils, and greases attached to the surface.

Silicon wafers of <100> orientation of 10 Ω.cm resistivity and 50 mm diameter and thickness of 381±50 μm were cleaved into 1 cm x 1 cm pieces and then degreased in organic solvents The cleaning procedure involved a sequential washing of the samples with methanol, acetone and trichloroethylene in this order and then in a reverse order by acetone then methanol. The samples were then rinsed with de-ionized water. This cleaning was done under ultrasonic agitation. After rinsing, cleaning was followed by an etching process to get rid of any surface oxide layer. This was done by etching in a 20%

hydrofluoric acid (HF) solution for a minute or so. After the HF treatment, the samples were again rinsed in de-ionized water and were kept immersed until the depositions were ready. Upon removal the samples came out dry and were loaded into the evaporation chamber immediately.

2.2.3 Electron Beam Deposition

The silicon substrates were mounted on aluminium sample holders with wire clips and care was taken to clip the sample as close to the edge as possible to prevent shadowing the centers of the samples from the deposition process. They were then put on a rotatable sample changer. The system could only accommodate six sample holders. Pumping down was done by various systems serving the evaporation chamber. After rough pumping, a set of vacsorb pumps under liquid nitrogen cooling were used to pump down to pressures of the order of 10^{-5} kPa. Further pumping was carried out by titanium sublimation and condensation onto a liquid nitrogen filled cryopanel.

The pressure measurements were done with a thermocouple gauge in the range of atmospheric to 10^{-3} kPa and a range of 10^{-3} kPa to 10^{-8} kPa for the penning gauge. The metals to be evaporated were put into the three crucibles of a multiple hearth. The metals were heated with a 3 kW electron gun system. The filament current was used to control the electron gun system. A potential field of 4 kV was used to accelerate the electron beam and the beam focused on to the metal by a permanent magnet, directly below the hearth. The hearth was itself water cooled to act as a heat sink to the crucibles. Heating of metals from room temperature to the point of sublimation or evaporation after melting was done with extra care to prevent flaking, spurting gaseous outbursts which all could lead to material loss from crucible. During this preheat treatment of the metals; the samples were protected by a shutter. A water cooled quartz crystal monitor was used to monitor the deposition rate and the total thickness.

To prevent contamination during the operation of the evaporation system, several precautions were taken, *viz;*

- Thorough cleaning of crucibles before introducing the charges (metals) by cleaning solvents like ethanol etc,
- During preheating the shutter was closed to prevent vapours from settling on the surfaces of the samples,
- Accidental contamination of metals was prevented by shielding each crucible from the adjacent ones by partitions of about 20 mm high.
- Skin contact with the interior surfaces was avoided by wearing clean gloves

After evaporating the metals, the system was allowed to cool off for about two (2) hours before samples could be taken out. After the samples were taken out, clip shadows could be seen on the samples which could be useful in confirming that the metal had been deposited as well as determining thickness using Profilometry on the resulting step between the shadow and the film.

2.3 Synthesis of HA thin films using Sol-Gel processing

For all the experiments described in the upcoming sections, the precursor sol used is prepared as described in the following subsection.

2.3.1 Formation of the precursor sol

This procedure follows Lopatin's dissertation [10]. The precursor sol was made using n-butyl acid phosphate (n-BAP) and calcium nitrate tetra-hydrate, as the sources of calcium and phosphorous. The presumed steps of the reaction are given below [10].

- Hydrolysis of the n-BAP

$[RO]_2\ P(O)OH + 2H_2O \rightarrow H_3PO_4 + 2ROH$, where $R = CH_3(CH_2)_3$

- Condensation.

Some of the hydrolyzed n-BAP undergoes condensation reactions forming dimers and higher order linear phosphates as shown below,

$H_3PO_4 \rightarrow H_4P_2O_7 + H_2O$, a pyrophosphate

- Addition of the calcium tetra-hydrate.

This does not play a role in sol formation but when there is significant polycondensation, the calcium ions act as network modifiers by preventing phosphate chains becoming too large. The chemicals used in the synthesis are n-butyl acid phosphate (n-BAP), de-ionized water, 2-methoxyethanol and calcium nitrate tetra-hydrate.

Procedure

1. De-ionized water was mixed with n-BAP for one minute
2. One third of the solvent, 2-methoxyethanol was mixed with the n-BAP for one minute
3. Calcium nitrate tetra-hydrate was added to the remaining two thirds of the solvent, 2-methoxyethanol and mixed thoroughly. The mixing was done with a magnetic stir bar and a gentle heat taking care that the heat is not too much to start evaporating the solvent. This mixing was done for twenty minutes until complete dissolution occurred.
4. The two mixtures were added together and mixed well using the same magnetic stirring plate for about five minutes. The solution was then left to cool before use. The batch was then stored for future use and subsequent experiments.

Different molar concentrations and volumes were made depending on the experiment and below is a table of the calculated recipe for the HA concentrations.

Table 2.1: Calculated molar concentrations and of 100 ml of HA. N-BAP is the n-butyl acid phosphate; Di-H_2O is the de-ionized water, 2-MOE is the 2-methoxyethanol and CaN_4H_2O is the Calcium nitrate tetra-hydrate

Molar concentration of 0.1 M:	
	100 ml
n-BAP	10.24
Di-H_2O	1.64
2-MOE	80
CaN_4H_2O	23.6
Molar concentration of 0.15 M:	
	100 ml
n-BAP	15.4
Di-H_2O	2.44
2-MOE	71.4
CaN_4H_2O	35.4

References

[1] Guo L, Hui Li , "Fabrication and characterization of thin nano-hydroxyapatite coatings on titanium," Surface & Coatings Technology 185 (2004) 268-274.

[2] O'Connor D.J., Sexton B.A., Smart R.S.T.C., "Surface Analysis Methods in Materials Science" ,Second Edition,2003, Springer Series, Berlin.

[3] Feldman L.C. and Mayer J.W., Fundamentals of Surface and Thin Film Analysis, 1986, Elsevier Science Publishing Co., New York

[4] Pretorius R., "Surface and Subsurface characterization of solids using Rutherford backscattering spectroscopy," S. Afr J. Physics 12 No. 1 (1989)

[5] Soares G.D.A., Vanzillota P.S., Bastos I.N., Materials Research Vol. 7, 3 (2004)437-444

[6] Prado da Silva M.H., Soares G.D.A., Elias C.N., Best S.M., Gibson I.R. Di Silvio L., Journal of Materials Science,: Materials in Medicine, 13 (2003)511-519

[7] Cullity B.D., Elements of Crystal Diffraction, Addison-Wesley Publishing Company, Philippines, 2nd Edition, pg 284, 1978

[8] Luptak K.A., MSc Thesis, Arizona State University, 1994, USA

[9] Wikepedia (2006), "Atomic Force Microscopy," [**Online].** Available at http://en.wikipedia.org/wiki/Atomic_force_microscope,

[10] Lopatin C.M., PhD thesis, Arizona State University, 1999, pg 82-83

Chapter 3

Effect of Ion Beam Mixing on Structural, and Adhesion Properties of Hydroxyapatite Coating

3.1 Introduction

Ion beam implantation has been used by many workers in surface modification of materials. As has been mentioned in chapter 1, there are two types of implantation; the beam line ion implantation which uses a line of site implantation and the plasma immersion ion implantation (PIII). PIII uses an immersion method where a material is immersed in a sheath of ions and an equal flux of ions is implanted on all surfaces of the sample, as opposed to the line of site ion implantation which requires a material to be rotated in order to implant all the surfaces. With PIII, complex shapes can be implanted and so this has a potential application in the orthopedic field.

When hydroxyapatite (HA) is used as a coating for metal substrates, the HA/metal interface also referred to in this thesis as a "mechanical interface," is a major failure mode in most implants [1]. One potential way of improving the coating adhesion is through the use of ion beam mixing [2].

In ion mixing, ions bombard the surface of the material and disrupt the microstructure. The ions penetrate and cause an alloying effect between the surface coating materials and substrate [3]. In this way the atoms displaced at the

film/substrate interface can lead to increased adhesion. Many researchers have used beam line plasma implantation to modify surfaces. Lopatin *et al*., in their study managed to improve the adhesion of HA on the metal substrates, increased hardness by fifteen times and densified the HA with the implantation [2]. In the present report, PIII will be used instead of the beam line implantation on the substrate. As a hypothesis it is assumed the implantation will cause some surface roughening on titanium so that when the film is subsequently spun on, it would attain increased bonding.

When a sol-gel film is first made, its density is generally less than half the theoretical value of the ultimate target material [2]. High temperature sintering is the most common method of densifying HA films [2]. However, as with HA, densification and crystallization are competing mechanisms and so to achieve these two, sintering to full density may be necessary before crystallization [4]. A problem arises as HA transforms to other phases such as tricalcium phosphate and oxyhydroxyapatite at temperatures above 850 ^{o}C, therefore to attain the two properties, low temperature densification is a solution and then the densified film can the be subsequently processed at temperatures below 800 ^{o}C.

Ion implantation has been used as a low temperature technique to densify ceramic films. A review can be found in section 1.7.2. Lopatin *et al.* also achieved densification of 83% of full density of HA in his work with beam line implantation [2]. The chapter reports the feasibility of PIII in improving adhesion and structural properties of the HA coatings.

3.2 Experimental methods

3.2.1 Sample preparation

3.2.1.1 Substrate preparation

Samples approximately (1x1) cm^2 were cleaved from <100> silicon wafers with a diamond scribe. These substrates were sequentially and ultrasonically cleaned in organic solvents and HF acid as described in section 3.3.2. After the cleaning procedure, the sample exhibited a mirror-like finish.

3.2.2.1 Metal deposition

After cleaning the Si substrates Six (6) sets of different metals namely titanium (Ti), chromium (Cr), cobalt (Co) and vanadium (V) were electron-beam deposited on them. The thickness of each metal layer was approximately 400 nm.

3.2.1.3 Spin coating and firing

Before the spinning procedure, the samples were blown off using a dust can to remove any dust particles that might have adhered on the samples. The samples were placed on a frustum shaped spin-head. The shape is designed in such a way as to ensure total coverage of the spin-head with the samples and hence preventing spillages of the sol onto the suction pipe located directly at the centre of the spin-head. A 0.15 M sol was spin coated on the substrates using a CHEMAT spin coater model KW 4A. The samples were spun at a rate of 4000 rpm for 10 seconds. The relative humidity (RH) in the preparation laboratory was in the range of 10-14%. This was important as humidity can affect the quality of the films. Therefore low RH was desirable so as to have smooth films.

Immediately after spin coating, the samples were dried on a hot plate (CHEMAT model KW 4AH) at 300^oC for 3 minutes. The drying step is important as it helps drive off solvents from the film as well as increasing the physical stability of the film before handling. The Lindberg Blue M furnace was used for firing. The samples were all fired for five minutes at 850^oC.

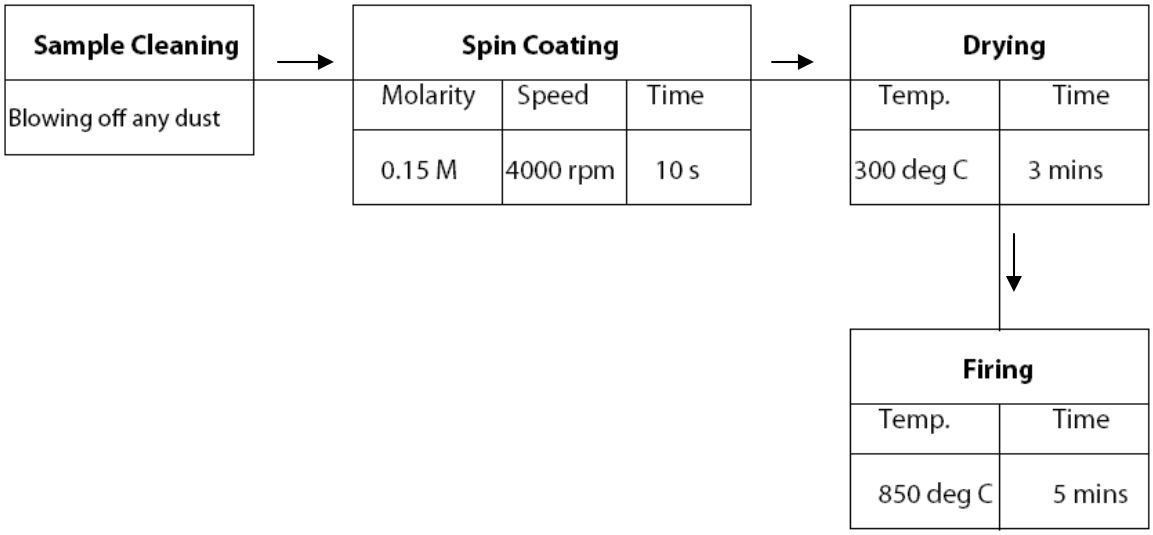

Figure 3. 1: Figure showing a schematic of the sample preparation procedure.

3.2.3.1 Plasma Immersion Ion Implantation

The plasma implanter was used, with argon as a feed gas. The plasma immersion ion implantation was done under a pressure of 0.04 Pa. The discharge voltage and currents were respectively 50 V and 0.5 A while the bias voltage and filament current were 20 kV and 27 A respectively. The implantation time was thirty (30) minutes with the pulse time being 5 μs.

Two implantation procedures were performed on the samples, namely,

1. Implantation into the metal surface. The argon ions were implanted on the metal surface before the HA deposition was performed. The end sample was one with HA film deposited on the plasma irradiated metal surface.
2. Implantation into the HA film. In this case, the HA was firstly deposited on the metal substrates followed by ion implantation into the spun-on surface coating.

These procedures are clarified in Figure 3.2.

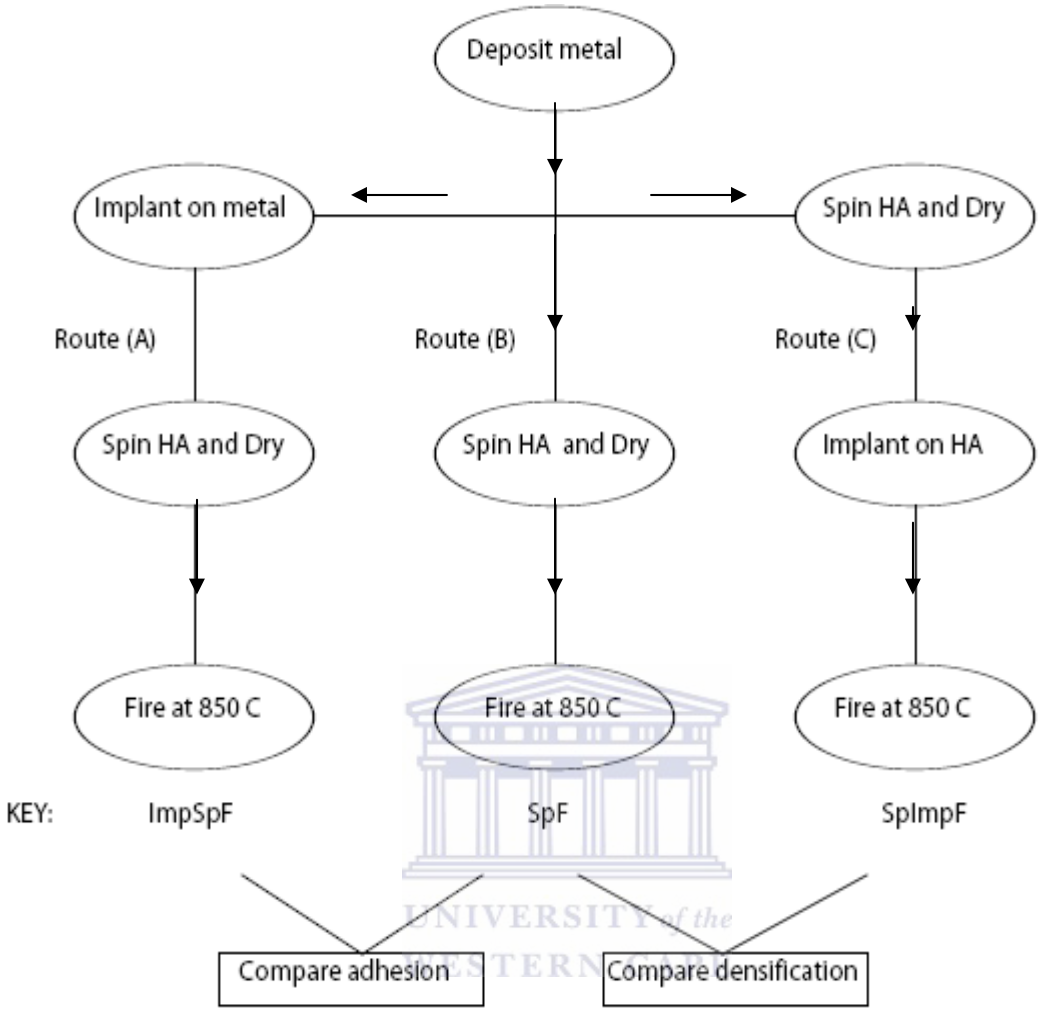

Figure 3. 2: Overview of the experimental procedure to evaluate the adhesion and densification of the HA samples due to argon implantation. The arrows show the direction (or steps) of the experiment.

In route A, indicated in the Figure 3.2, two (2) substrates of each metal were used. These substrates were implanted with argon plasma into the surface of the metal before the HA spin coating process. One sample of each metal was analyzed in the SEM for any surface damage or change but no visible difference was observed. HA sol was spin coated on these samples and dried. Then one sample was removed for characterization sample at this stage. The remaining sample was then fired to complete the process. This was

designated as '**ImpSpF**' because the substrate was **Imp**lanted then subsequently **Sp**in coated with HA and then **F**ired.

Route B was simply the control route. The one substrate of each metal was spin coated with HA, dried and then fired. This was identified as '**SpF'** for the substrate that was **Sp**in coated with HA and then **F**ired.

Route C involved the two substrates of each metal being spin coated with HA and then argon plasma implanted on the HA film. At this stage, before firing one sample was removed for characterization and then the remaining one was the fired and was denoted as **'SpImpF**' for the sample that was **Sp**in coated with HA , **Imp**lanted with argon and then **F**ired.

Route A was compared with the control (route B) to obtain information about the feasibility of improving adhesion of HA coatings to the metal substrates via plasma implantation. The comparison of route C with the control was used to obtain information on the feasibility of using plasma implantation to densify the HA films.

3.3 Characterization Techniques

The techniques used in characterizing the films included XRD, RBS, SEM, Optical microscopy, Tape test (ASTM D3359-02) and Atomic force microscopy. SEM and atomic force microscopy (AFM) were used to obtain information on the morphology, crystallite size and roughness. The V700 Nanoscope was used. A 5 μm x5 μm image was taken on each sample. As will be observed, the images for the other metals (Co, V and Cr) do not provide much information on the aims of the project due to their surface properties. Chromium for example in XRD has many peaks, which make it difficult to identify the HA peaks hence only the HA/Ti/Si system was further investigated.

Particle induced x-ray Emission (PIXE) was used to determine if some of the argon ions actually entrapped/embedded in the metal surfaces. This was used on the implanted

chromium and titanium surfaces. The technique is however inconclusive for titanium as the escape peaks for titanium are on the same position as the argon peak.

XRD was used to obtain information on the crystallinity of the samples. A θ-2θ angle scan was used with a Philips diffractometer. The step width of the scan was 0.02. The voltage was set at 40 kV and current at 25 mA. The scans were done on the samples before and after firing.

RBS was used to confirm the chemical composition of the films, the thickness and the densification. An He^{++} beam with energy of 2 MeV was used. The sample tilt angle was set at 10^{o} to avoid channeling effects and the scattering angle was set at 165^{o}. The beam current was as low as possible to avoid beam damage to the sample. In spite of this, the beam left a circular spot on the sample. The data was analyzed using the RUMP program.

The tape test method, designation D3359-02 (Annual Book of ASTM Standards) was used to compare adhesion of the coating on the metal substrates with the control. This test is commonly used to test adhesion of coatings on metals despite its low sensitivity. Grid lines were inscribed on the sample 'ImpSpF' in route A and the control sample 'SpF' using a sharp blade making 1 mm x 1 mm squares. The surfaces were then brushed to remove any flake on the surface. The tape was then placed on the center of the grid and in the area of the grid; the tape was smoothed into place by a finger. After 90 ± 30 s of application the tape was removed by seizing the free end and rapidly pulling it back upon itself at as close to an angle of 180^{o} as possible. The grid area was inspected for removal of the coating from the substrate and the adhesion was rated in accordance to the scale in the D3359-02, Annual Book of ASTM Standards. Optical microscopy was used to observe the tape test results on the samples.

AFM was used to obtain information on surface topography of the HA on the titanium substrates. The topographical description of the surfaces using a three-dimensional numerical evaluation was used to obtain roughness parameters. The profile parameters used for the evaluation of the amplitude (height) of the surface were R_a and R_q. R_a being

the arithmetical mean deviation of the profile while R_q being the root-mean square deviation of the profile. These numbers were generated by the Veeco Nanoscope V700 software. These values were obtained from using equations 2.1 and equation 2.2 to obtain R_a and R_q respectively.

$$R_a = \frac{1}{N}\sum_{j=1}^{N}\left|Z_j\right| \tag{2.1}$$

$$R_q = \sqrt{\frac{\sum (Z_j)^2}{N}} \tag{2.2}$$

Where Z_j is the current Z value and N is the number of points within the box cursor [5].

3.4 Results and Discussion

3.4.1 Scanning electron Microscopy: Surface morphology.

To observe the surface morphology of the samples, SEM was used. This was done on all the metal substrates; Ti, Cr, V, and Co. Figure 3.3 shows images of HA films on cobalt and vanadium after firing. Cobalt tends to peel off while vanadium beads up. These samples were subsequently not further investigated.

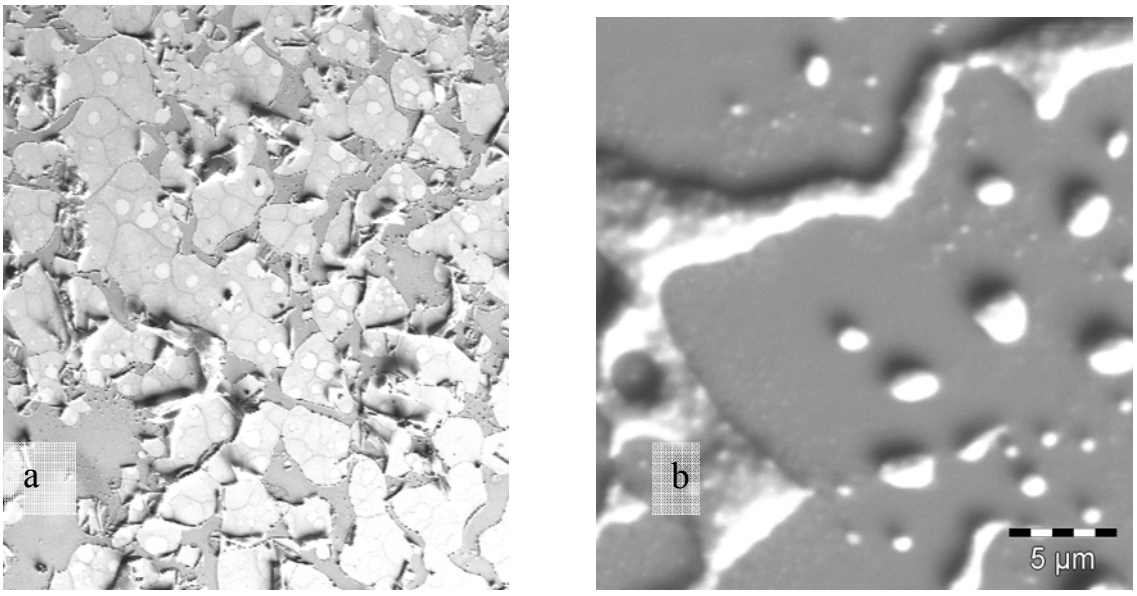

Figure 3. 3: SEM micrographs of HA on (a) Cobalt and (b) Vanadium. All have the same magnification. Delamination and beading up can be observed respectively.

The micrographs of all the three routes indicated in Figure 3.2, of HA deposited on each of the metal substrates is shown in the next figures. Figure 3.4 shows the HA deposited on Ti. Fig 3.4a shows the image for the sample of HA deposited on the implanted metal surface (ImpSpF). Fig 3.4b shows an image of the control (HA simply fired without any implantation) (SpF) and Fig 3.4c shows the image for HA implanted with argon ions (SpImpF). The same pattern applies for the other metals, vanadium and chromium. Figure 3.5 show images for HA on chromium and finally Figure 3.6 is for HA on vanadium. For the figures below, (a) represents the route ImpSpF, where the HA was deposited on the implanted metal surface and then fired (b) denotes the control, SpF, where HA was simply fired and (c) labels SpImpF representing the HA that was deposited on the metal substrate, implanted with argon ions on top and then fired at 850^{o}C for 5 minutes.

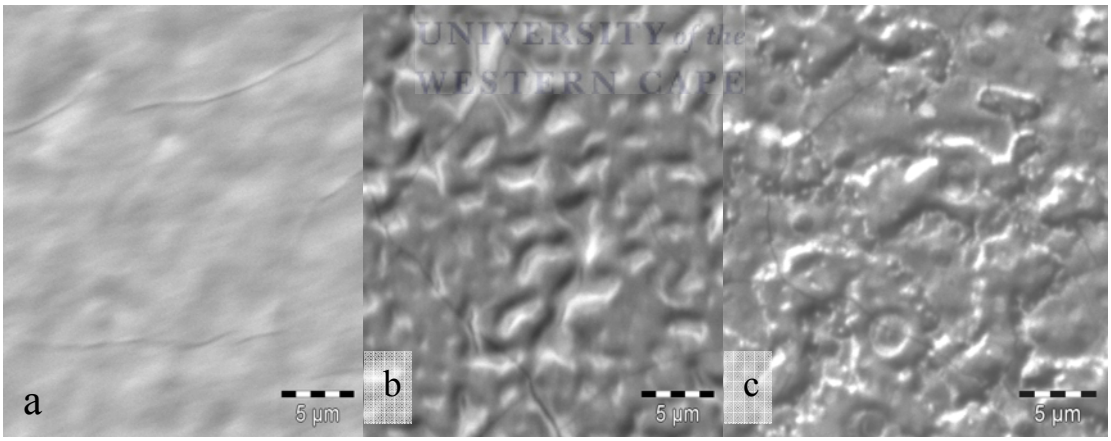

Figure 3. 4: SEM backscattered electron (BE) images for the HA/Ti/Si system. (a) ImpSpF, (b) SpF, (c) SpImpF. Cracks can be observed. The implanted HA surface (c) looks more rougher than the others

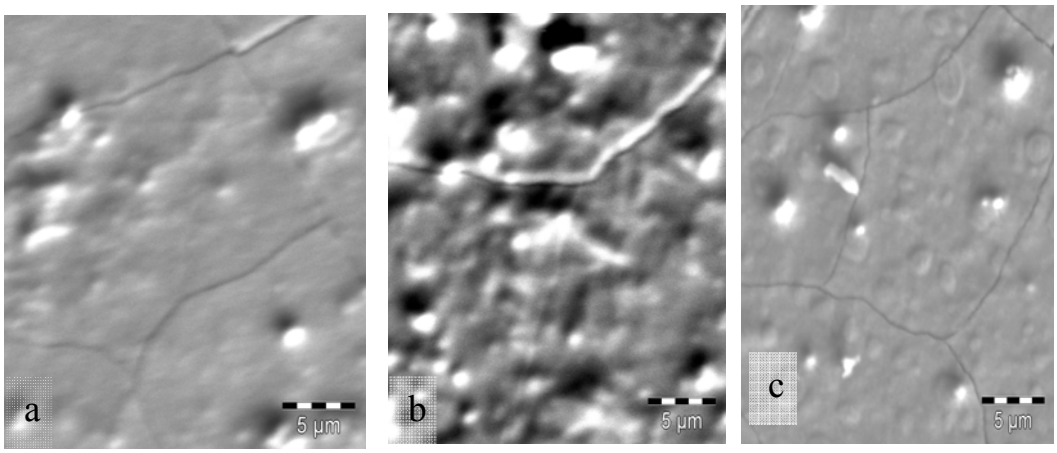

Figure 3. 5: SEM backscattered electron (BE) images for the HA/Cr/Si system. (a) ImpSpF, (b) SpF, (c) SpImpF. Cracks can be observed. The implanted HA surface appears more compact than others.

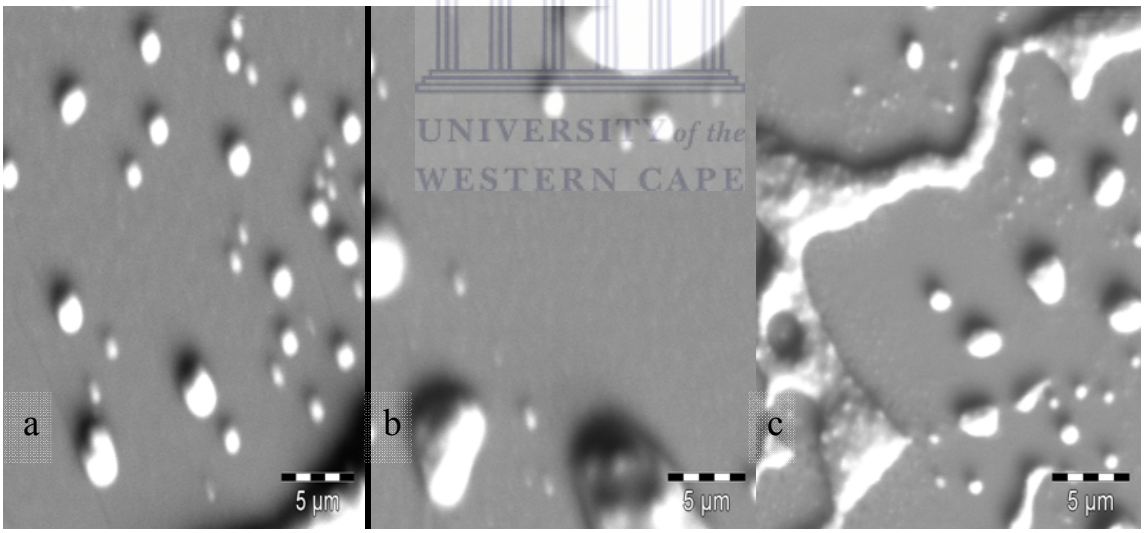

Figure 3. 6: SEM images for the HA/V/Si system. (a) ImpSpF, (b) SpF, (c) SpImpF. Beading can be observed. The HA globules seems to have come together for the implanted HA.

SEM micrographs from Figure 3.3 show that HA does adhere well on the cobalt and vanadium surfaces. Cracks and delamination can be observed on the cobalt sample.

Delamination of the metal from the silicon substrate can also be noticed. This is suspected to be due to in-plane tensile stresses at the metal/substrate interface and also HA/metal interface because the films are constrained on the surface. The difference in thermal expansion coefficients of the film and its substrate also contribute to the stresses hence the cracks and delamination. The HA sol on the vanadium surface seems to bead, forming globules. This may be due to poor wetting properties of vanadium towards HA.

From the micrographs in Figures 3.4 to Fig 3.6, interesting results can be observed. Comparisons of images (a) and the control (b) show no real differences between the images. This implies that ion implantation on the surface of the metal does not provide visible information on the adhesion properties of the HA film. However, cracks are still visible which are due to stresses generated during the firing process.

Comparison of images (b) and (c) (control and film which was spun on, fired and subsequently implanted) give information on densification. Noticeable are shrinkage and cracks on the implanted samples. The shrinkage is due to the densification mechanisms. In addition to this, the implanted films show more cracks than the un-implanted. These are suspected to be due to the tensile forces generated by the film densification induced by the irradiation. The same effects were observed by Lopatin et al [2], however, using the reverse procedure of firing and then implanting into the HA.

3.4.2 Atomic Force Microscopy: Morphology and Roughness

The surface morphology and roughness of the films were determined using atomic force microscopy. All the films prepared from the three different conditions were imaged. Figure 3.7 shows the AFM image for a non irradiated sample. The image for the HA film on an implanted metal substrate is shown in Figure 3.8. On both, the surfaces appear rough and have pits. Figure 3.9 shows the HA film that was implanted and subsequently fired. It is rougher than the other two samples. It also appears to contain faceted, elongated structures that are suspected to be grains or maybe due to the roughening mechanism of implantation. However, this result is an exact opposite to the findings of

Lopatin *et al.* [2] where they used the reverse procedure (fired then implanted) and found no grains on implanted samples.

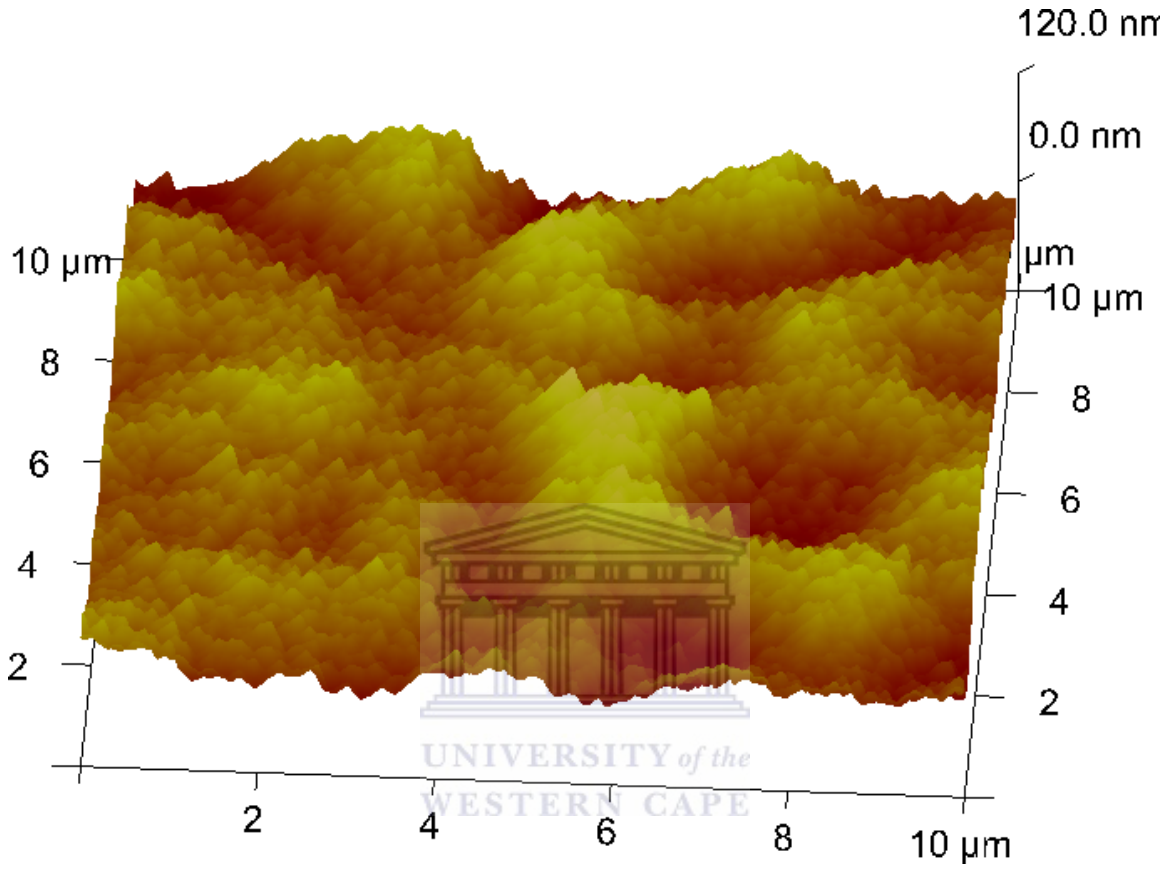

Figure 3. 7: Atomic force micrograph of the HA film fired at 850 ^{o}C for five minutes. The film is approximately 400 nm. This was the control film without implantation (SpF).

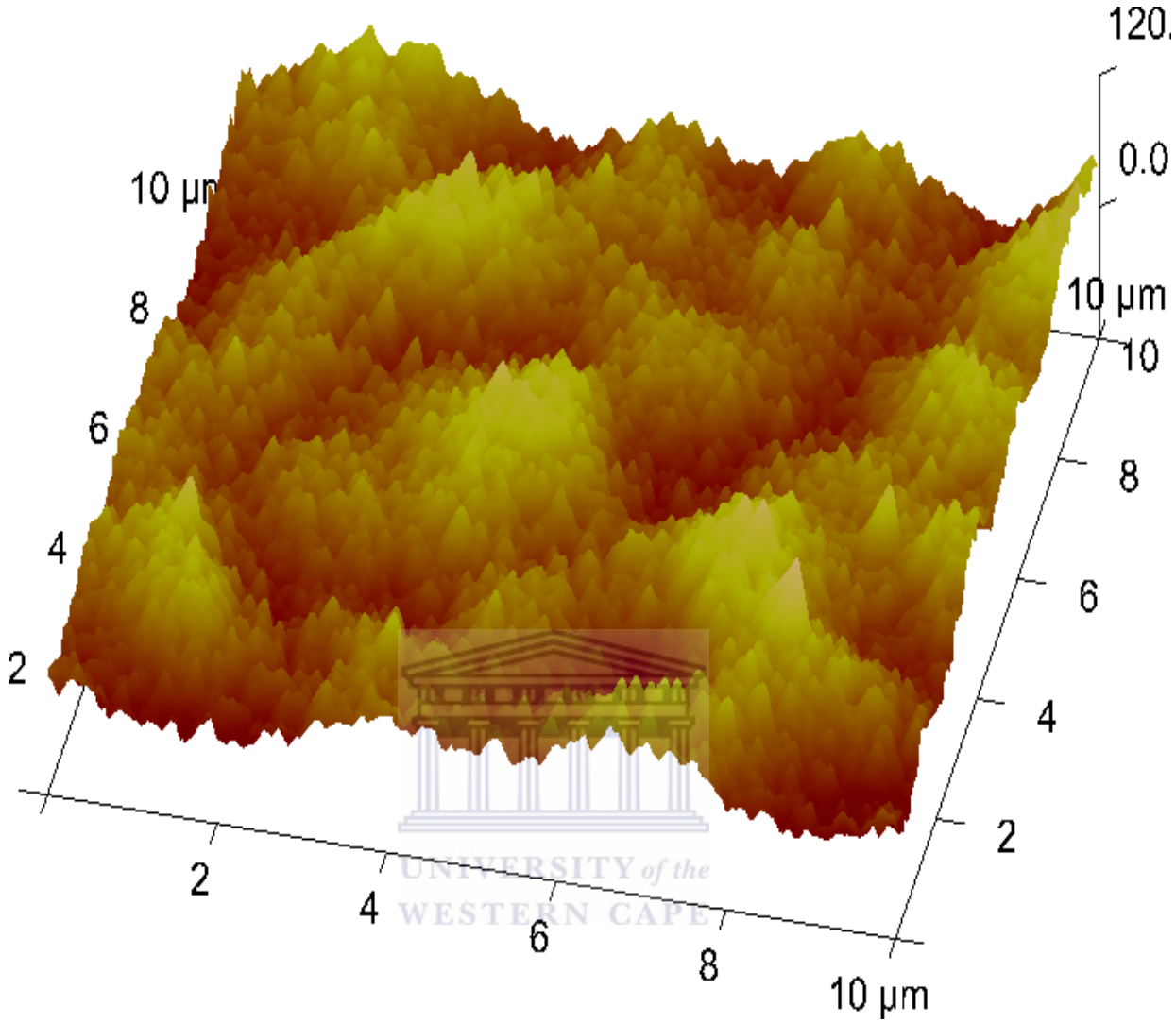

Figure 3. 8: Atomic force micrograph of a film fired at 850 ^{o}C for five minutes on an implanted substrate (ImpSpF). Pits can be observed on the film.

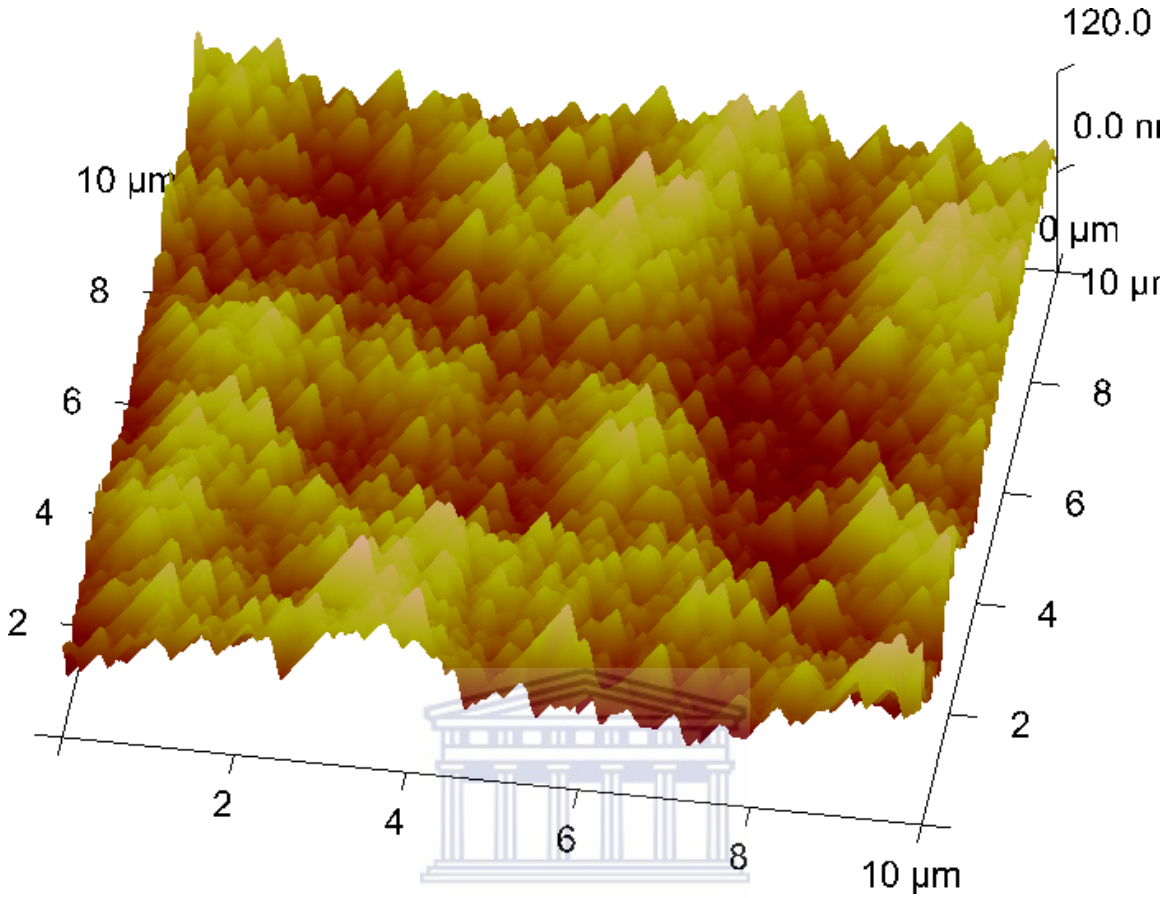

Figure 3. 9: Atomic force micrograph of the implanted HA film and then subsequently fired at 850 ^{o}C for five minutes (SpImpF). The surface looks rougher with elongated grains.

These above results are quantitatively given in the graph shown in Figure 3.10. The roughness results are given. The implanted HA film is rougher than the other two, SpF and ImpSpF samples. From the results it seems that implantation of the HA spun film causes more roughening on the film.

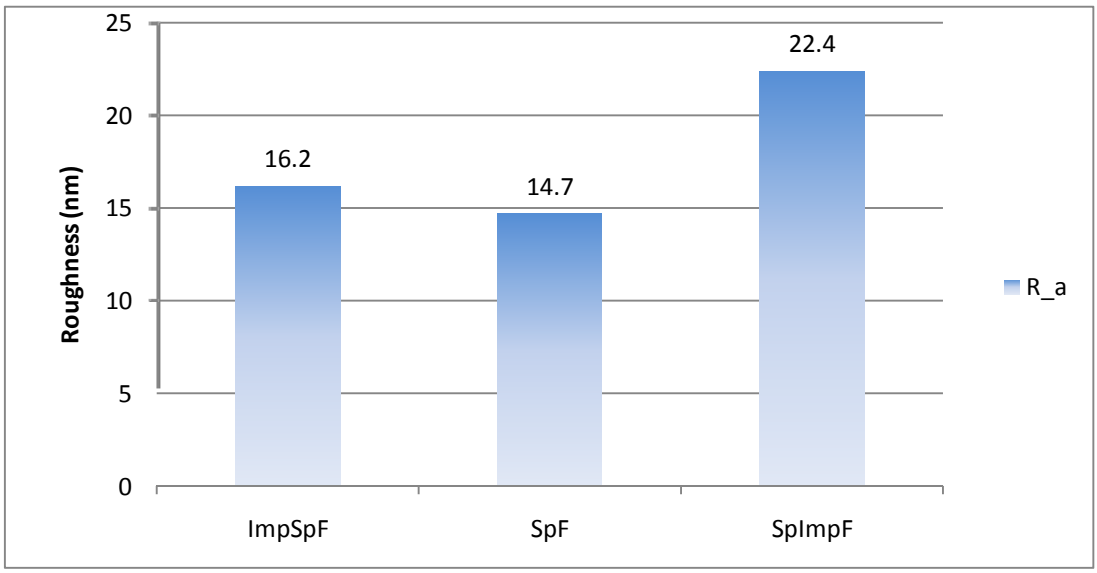

Figure 3. 10: Chart showing AFM results for roughness of samples from three different processing conditions. ImpSpF was a film deposited on the implanted substrate and then fired while SpF was the control, the un-implanted and finally the SpImpF was the implanted HA film that was subsequently fired.

3.4.3 Particle Induced X-ray Emission (PIXE): argon identification

For the identification of argon implanted into the metal surface, PIXE was used. Figure 3.11 shows the PIXE spectrum for the chromium surface implanted with argon plasma. The argon peak can be observed. Figure 3.12 shows the spectrum for the un-implanted chromium. Figure 3.13 shows the spectrum for the implanted titanium surface.

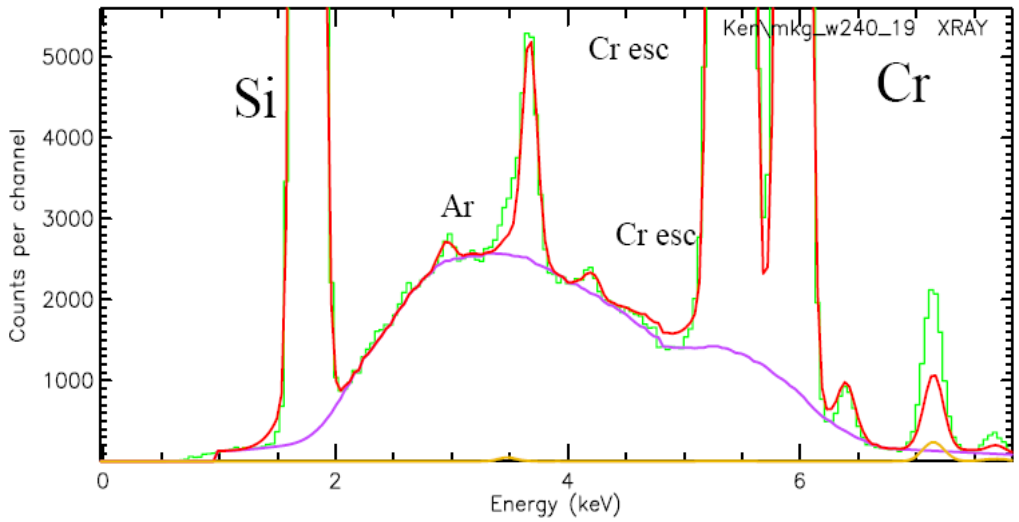

Figure 3. 11: PIXE spectrum for the argon implanted chromium. The argon peak can clearly be observed. The 125µm Be filter was used.

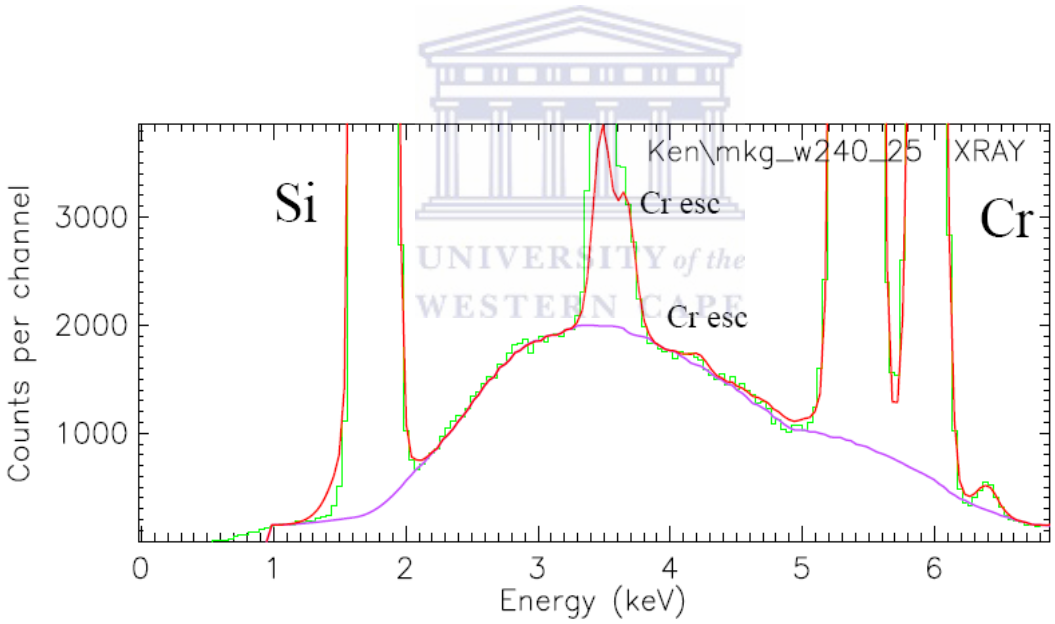

Figure 3. 12: PIXE spectrum for the un-implanted chromium. A very small argon peak can be observed. 125 µm Be filter was used.

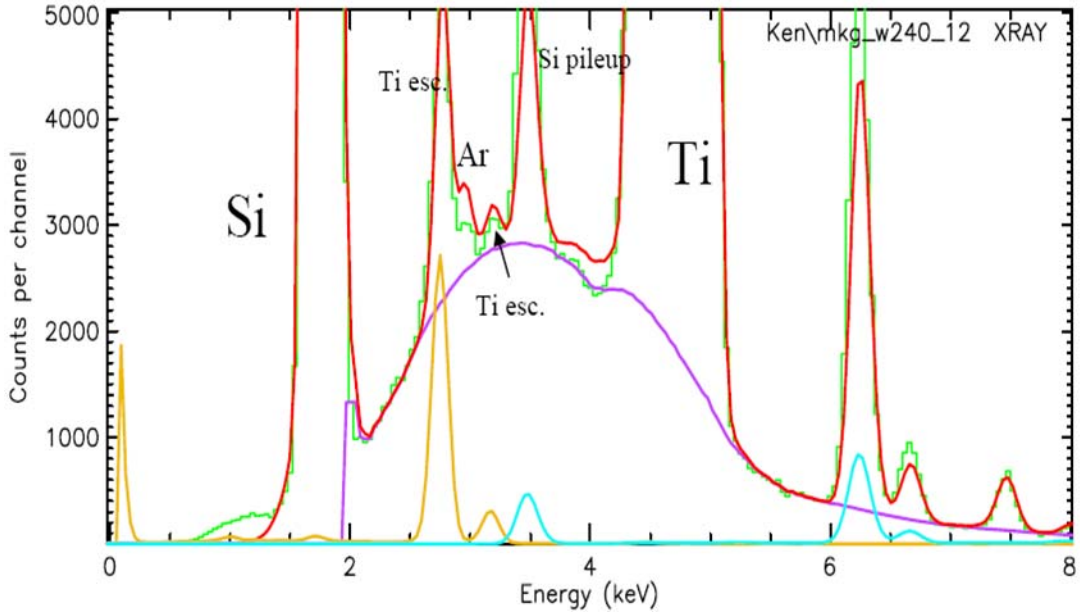

Figure 3. 13: PIXE spectra for the argon implanted titanium. Argon peak coincides with the Ti escape peaks. Be 125 µm filter was used.

To ascertain if implantation really has an effect on the surface, PIXE was used. This was basically to identify the argon under the surface of the metal substrate. When a surface is implanted with high energy ions through, in this case, plasma immersion ion implantation, damage will be done on the surface. These may include bubble formation (roughening the surface), vacancy formation and ion attachment (surface charge) [6]. TRIM simulation calculations showed that for a bias voltage of 25 kV, the ions would go as deep as 134 Å and 203 Å in the chromium and titanium surfaces respectively. For this reason, surface charge is improved. The net effect of this surface charge is to create a local environment with a specific surface tension, surface free energy and energy of adhesion [7].

In terms of identifying argon on the metal substrates, clearly noticeable in Figure 3.11 is the argon peak on the chromium spectrum for the implanted substrate. There is a small Ar peak on the spectrum in Figure 3.12, which could be due to ambient Ar from exposure to air. This conclusively confirms the ion attachment during implantation though it can not be determined how deep they went.

However, for the titanium metal substrate, the spectrum in Figure 3.13 does not conclusively show the argon peak. This is because the argon peak coincides with the escape peaks of titanium hence there is a possibility that there are no argon ions attached or that the peak is overlapped by the escape peaks.

3.4.4 X-Ray Diffraction: Crystallinity and Phase Identification

For information on the HA crystallinity of the HA/Ti/Si system from the three preparation routes, XRD was used. Figure 3.14 shows the spectra for HA that was coated on the argon implanted Ti surface. ImpSp and ImpSpF denote spectra for the unfired and fired Ha respectively. The spectrum for the fired sample shows more intense peaks than the unfired. The major HA peak (211) can be observed.

Figure 3.15 shows the spectra for HA that was spin coated on the Ti surface and then argon implanted on top. SpImp and SpImpF are spectra for the unfired and fired samples. The effect of firing is evident as the fired sample has more intense peaks than the unfired. Furthermore, many HA peaks can be observed on the spectra from the route A, where the surface was first implanted before coating with HA than the route C sample spectra.

Figure 3.16 shows spectra to compare the effect of implantation of argon ion (1) into the Ti surface and (2) into HA, compared with the control, the un-implanted sample. All the samples were fired at 850^{o}C. Implanted samples are observed to have less intense peaks than the un-implanted samples.

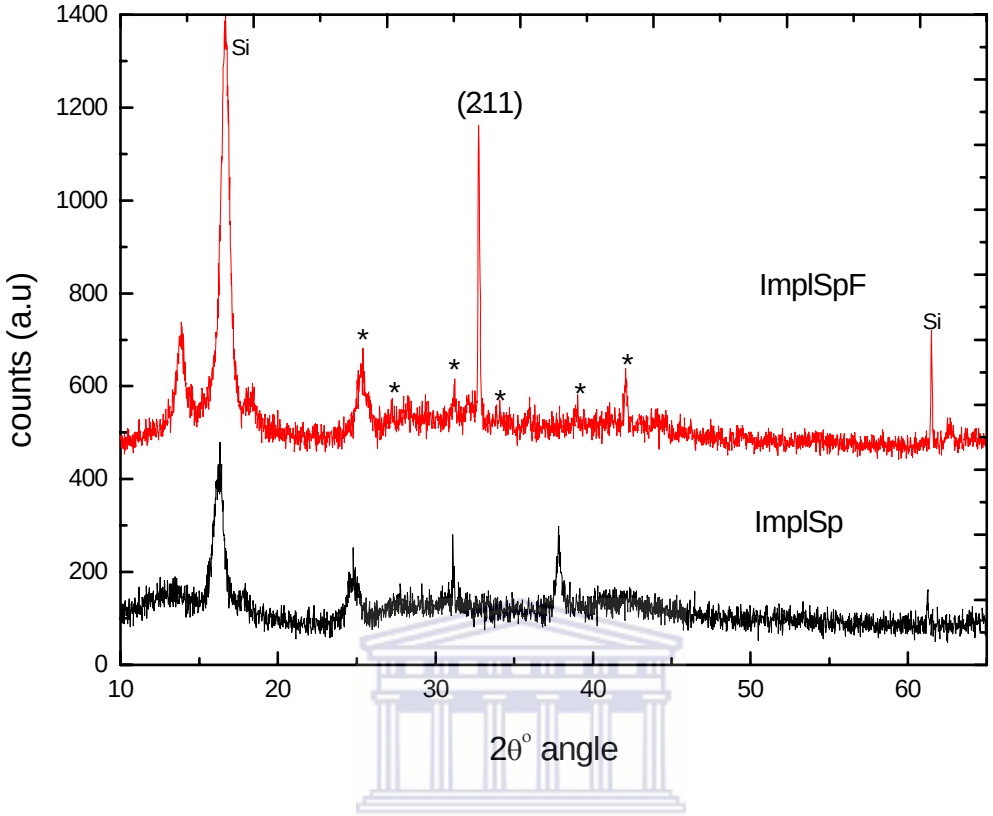

Figure 3. 14: Spectra showing the effect of firing on the HA/(implanted Ti) system. The major HA peak is evident on the fired sample. In the graph, ImpSP represent one that was not fired and the ImpSpF is for one that was fired at 850^{o}C. The * denotes the HA peak positions. Other peaks are unidentified. HA peaks are evident. The unfired sample is still amorphous

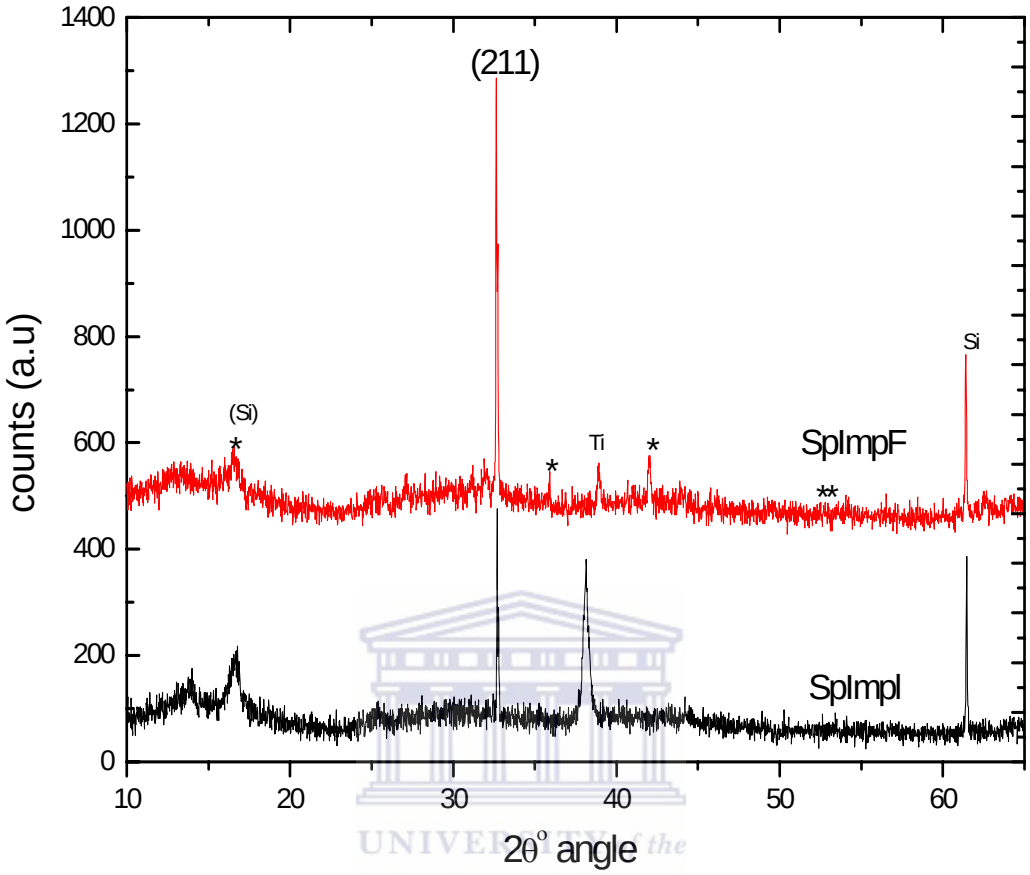

Figure 3. 15: XRD spectra showing implanted HA films. SpImp denotes spectra for HA spun on the substrate and then implanted while SpImpF denotes the same procedure but was fired at 850°C. Few HA peaks can be observed on the fired sample indicated by *, while no HA peaks can be seen on the unfired sample except substrate peaks.

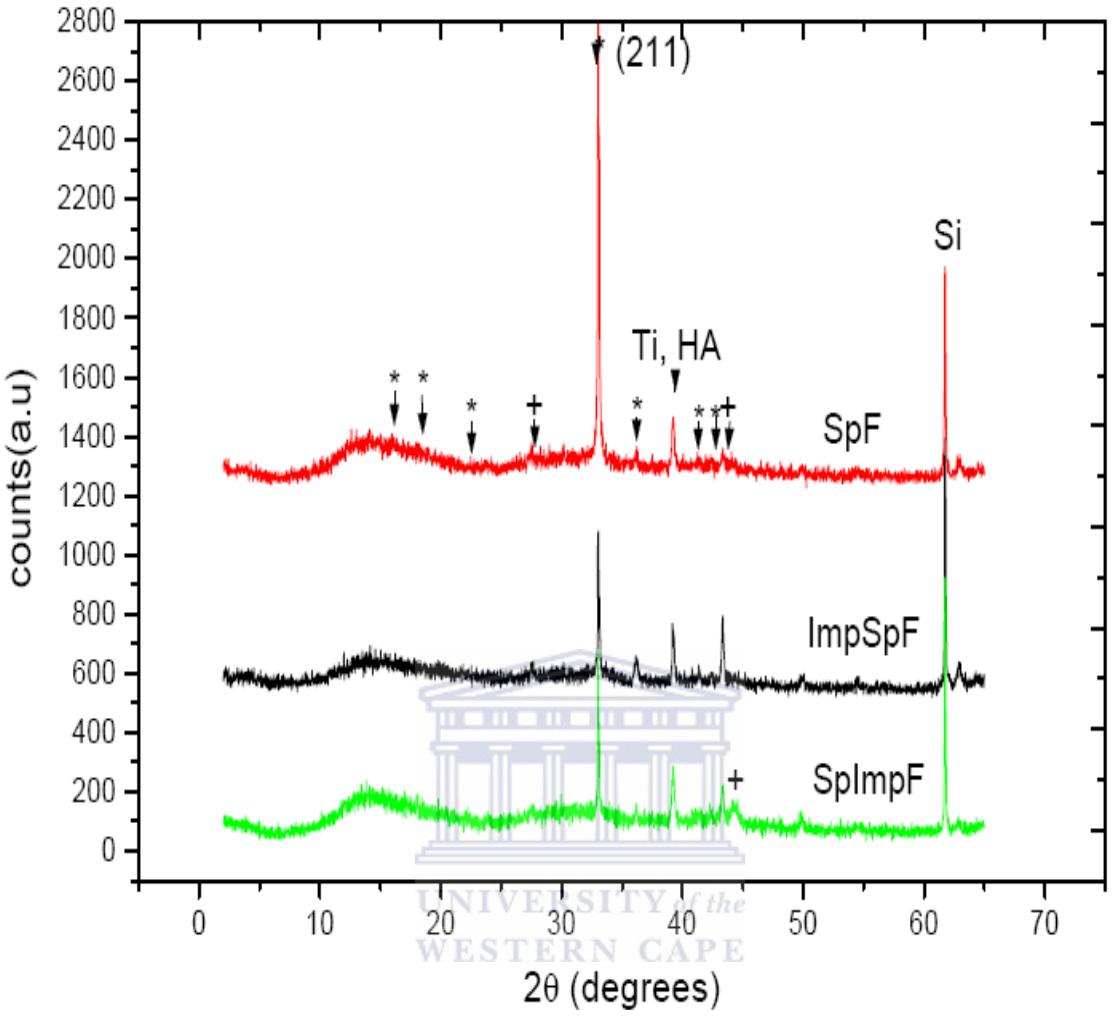

Figure 3. 16: XRD spectra comparing SpImpF and ImpSpF with SpF of the HA/Ti/Si system. In these spectra SpImpF denotes HA spun on the substrate and then implanted and fired while ImpSpF represents the substrate implanted and then HA spun on the implanted substrate and then fired. The SpF is the control, which is fired HA without any implantation. HA peaks are denoted by * . The samples were fired at 850^{o}C.

From Figure 3.14 to Fig. 3.16 the XRD spectra indicate that the HA film was successfully deposited on the surface. However, the peaks are not intense and the possible reason is that the films were very thin (~400nm) and also that the grazing angle analyses was not possible. Not much information can be obtained in this case.
As expected, HA peaks are more intense on fired samples than the unfired ones. This is because firing induces crystallinity of the HA phase while the unfired ones are still in the amorphous phase. The peaks that appear on the unfired spectra maybe Si peaks, or some not related to the HA film.

The comparison of HA that was plasma implanted and subsequently fired (SpImpF) and HA on the plasma implanted Ti surface (ImpSpF) with the un-implanted HA (SpF) is shown in Figure 3.16. The strongest HA lines are evident on both films however, noticeable from the spectra is the marked, intense major HA peak on the un-implanted sample. There is a reduction of peak intensities in the implanted sample. This is possibly due to the physical changes that arise from atomic and nuclear collisions during the implantation leading to formation of amorphous structure, hence the reduction of crystallinity of the HA [8]. This effect was also observed by Lopatin *et al*., on their work with the beam line plasma ion implantation [2] though they recovered it once it was fired again.

3.4.5 Rutherford Backscattering Spectrometry: Elemental Composition and Densification.

Rutherford backscattering spectroscopy was performed on the samples to confirm elemental composition as well as to determine possible densification of HA films as a result of the plasma implantation.

Figure 3.17 below show the RBS spectra for the unfired but implanted HA film compared with the HA film fired at 850 ^{o}C for five (5) minutes. From the figure, it can be clearly seen that the thickness is almost the same for both films

However, two observations can be made from the figure;

1. The Ca/P ratio from the unfired film is far less than the standard 1.67,
2. Some regions on the spectrum appear sloped implying a variable concentration of the HA versus the depth at the surface.

The comparison of RBS spectra from films prepared through three different routes is shown in Figure 3.18. The spectra fit each other regardless of the processing conditions although the implanted films show less thickness than the control, the un-implanted.

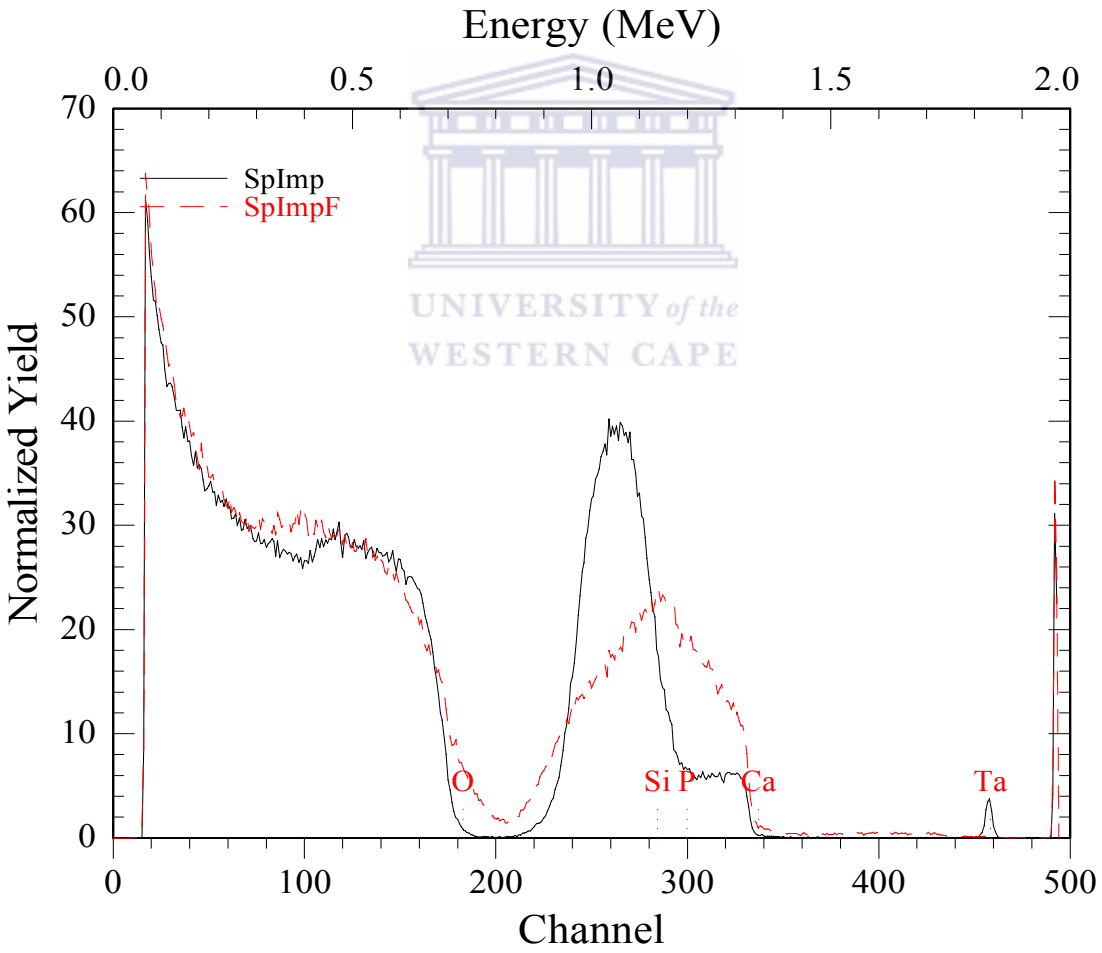

Figure 3. 17: RBS spectra for the HA/Ti/Si system, route C, comparing the densification of the fired and unfired films both implanted.

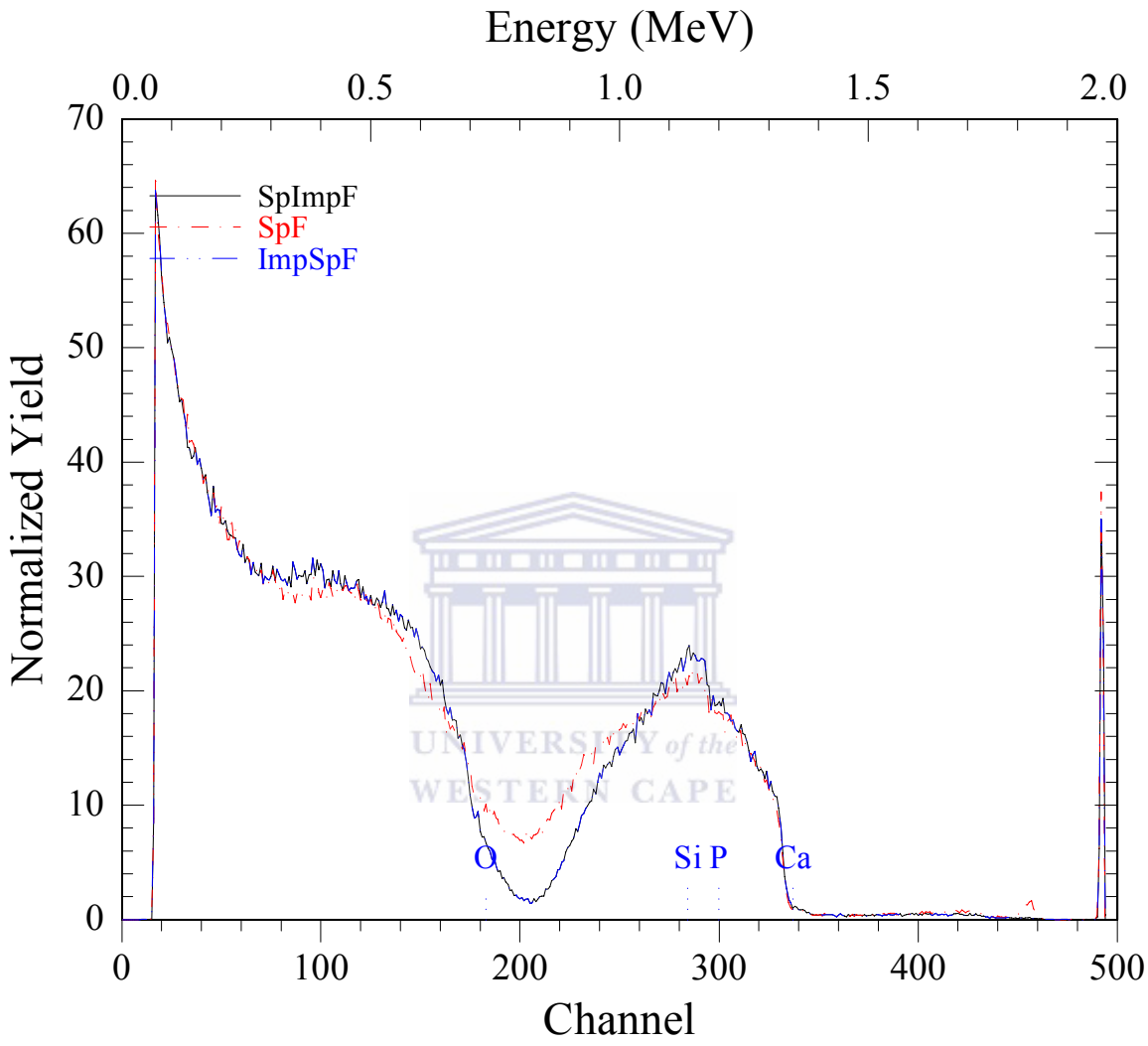

Figure 3. 18: The RBS spectra of all three conditions in HA/Ti/Si system all fired at 850 ^{o}C for five minutes.

From the above two figures, the spectra from fired films look irregular. This is suspected to be due the roughness on the film surfaces. Implantation caused the erosion of the surfaces as shown in Figure 3.4c. In addition to the effects of implantation, firing also produced tiny pores. All these compounded made the surfaces rougher hence the spectra obtained. From Figure 3.17, a small peak can be observed positioned at the energy of 1.838 MeV. This is believed to be Tantalum (Ta). This makes sense because the

filaments used in the implanter were made of tantalum consequently some of the Ta atoms were evaporated and implanted into the HA. The peak is not there on the fired sample. This is because the firing process drove off these atoms.

In terms of densification analysis, no quantitative method was applied. However, the qualitative methods, SEM and RBS were used. Interestingly these results compliment each other. The RBS spectrum for the implanted film in Figure 3.18 shows a small reduction in film thickness as compared to the un-implanted. This is possibly due to the shrinking of the film as a result of densification mechanisms during irradiation. This is also confirmed in the SEM images shown in Figures 3.4 and 3.5 as the films are cracked and look smooth suggesting film shrinkage.

3.4.6 Adhesion Testing: Tape Test

This test compares the effect of implantation on adhesion of implanted versus un-implanted metal substrate. This is illustrated in the sketch in Figure 3.2.

Figure 3.19 shows the adhesion test results of the control (un-implanted) sample before and after testing. Localized areas of weakness can be seen in the grids indicated by white spots in the image before the test. After the test, these spots are completely delaminated as the underlying substrate can be observed indicating that the tape actually peeled off some HA from the metal substrate.

However from Figure 3.20 no peeling off was observed from the samples whose metal substrate was implanted before and after the testing process demonstrating that irradiation could improve peel off resistance.

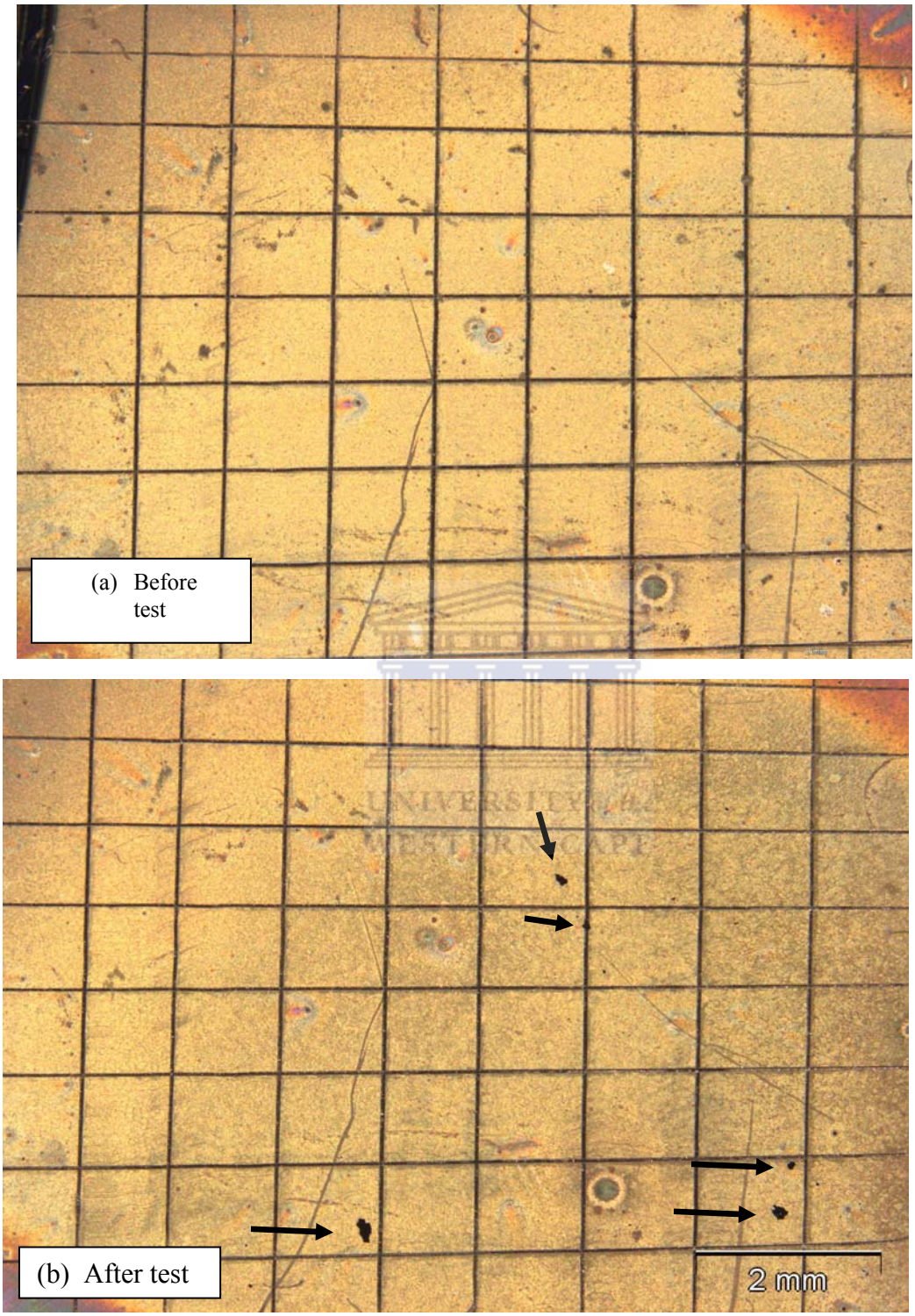

Figure 3. 19: Optical images of a film on an un-implanted substrate (control sample) before and after the tape test. The arrows indicate the delamination spots.

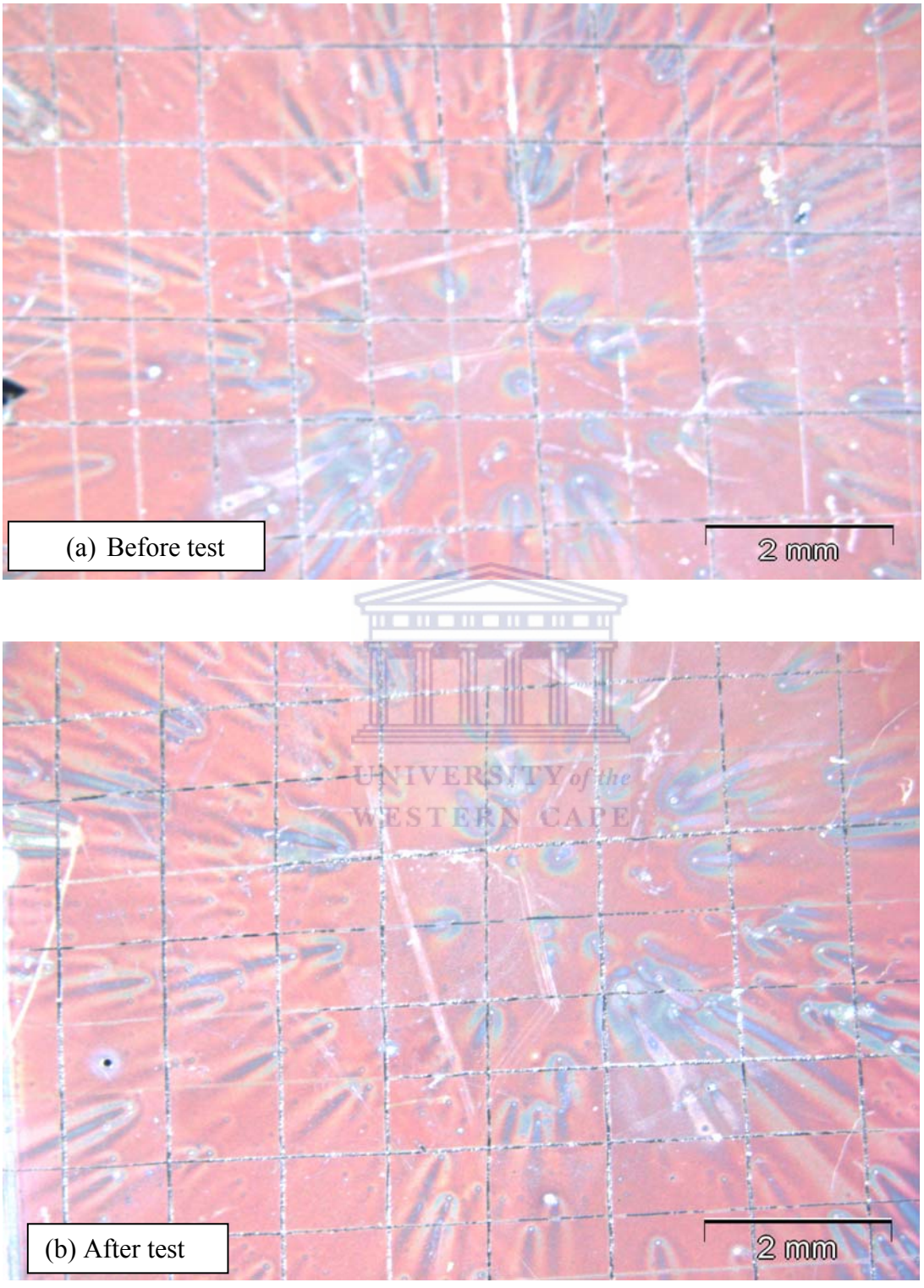

Figure 3. 20: Optical images of the film on an implanted metal substrate before and after test. No change of surface can be observed even after the test.

From the results above, it can be concluded that implantation can improve adhesion of HA on the metal substrate. Similar results were obtained by Lopatin *et al* [2] on their work with beam line implantation on HA where they found that irradiation increased scratch resistance of HA on metal substrates.

When a material is bombarded with ions in this case through ion implantation, the ions lose their energy through interactions with electron and atomic nuclei. Therefore, the electronic energy loss is responsible for excitation and ionization of target atoms while the displacement of target atoms is caused by nuclear energy loss [9]. From this, therefore, it can be seen that substantial energy is deposited in the film and is available in promoting densification.

It is well known that densification can be achieved through sintering at higher temperature. However, as has been mentioned earlier in section 3.1, crystallization and densification are competing mechanisms. Hence it is necessary to first densify and then crystallize. However, high temperature sintering of HA causes undesirable emergence of other phases such as tricalcium phosphates (TCP) etc, hence a low temperature method is desired. Moreover, TCP prevents the achievement of full density at higher temperatures as was observed by Wang *et al* [9]. Therefore an alternative such as plasma implantation can be used. From the present research, using plasma immersion, SEM and RBS results have shown qualitatively that this is possible and was also achieved by Lopatin [8] where he was able to densify up-to 83% of full density of HA. The densification results were obtained by comparing the results of the control samples (fired without implantation), with the sample that was implanted with argon ions (SpImpF).

Furthermore, ion/target interaction also causes ion beam mixing. In ion mixing, ions bombard the surface of the material and disrupt the microstructure. The ions penetrate and cause ion mixing between the ions and the target as well as an alloying effect between the surface coating materials and substrate [3]. This ion mixing has been shown to disturb the microstructure (crystallinity). In a study of ion beam modification, Volkert

found that amorphization occurred as a result of implantation [10]. Lopatin also observed a decrease in the degree of crystallinity of HA films after implantation (using beam line implantation) but found that it was reversible upon sintering again [11]. These results have been obtained in the present report, as shown by the XRD results in Figure 3.16 using PIII. In addition to the armophizing effect, this ion beam mixing process has an advantage due to roughening of the surface. By increasing the surface energy and charge, it improves the adhesion of the film on the substrate [7]. This was actually one of the main goals of the research as the implanted samples showed better adhesion integrity than the un-implanted ones.

3.3 Conclusion

It has been demonstrated that plasma immersion ion implantation as opposed to a more commonly used beam line implantation can be used to densify HA films as well as improve adhesion. All this is in the hope of improving the metal/HA interface which is reported to be a major weakness in implants. The following results were obtained;

- SEM results showed that irradiation caused shrinkage of the films and that HA does not adhere to vanadium but only forms globules.
- Ion beam mixing induced densification as evidenced from the shrinkage seen in SEM micrographs and the RBS film thickness variations.
- Implantation improved the adhesion of the HA to surfaces. However, the 25 kV bias voltage used in the implantation is not sufficient to cause major changes to the sample surface as the differences between the adhesion results of implanted and un-implanted films was minimal. Higher voltages could improve penetration and hence give better results.

References

[1] Filiaggi M.J., Coombs N.A., Pilliar R.M., J. Biomed. Mat. Res. 25 (1991)1222

[2] Lopatin C.M., Alford T.L., Pizziconi V.B., Kuan M., Laursen T., "Ion-Beam Densification of hydroxyapatite Thin Films," Nucl. Inst. & Meth. In Phys. Res. B 145 (1998) 522-531

[3] Luptak K.A., Masters Thesis, Arizona State University, 1994, pg 28

[4] Brinker C.J., Scherer GW, Sol-Gel science, Academic press, Boston, pgs 730,1990

[5] American Society of Mechanical Engineers (ASME) B46.12

[6] Zhao X., Liu X., Ding C., Chu P.K., "Effects of Plasma Treatment on Bioactivity of TiO_2 Coatings," Surface and Coatings Technology 201 (2007)6878-6881

[7] Boyan D.B., Hummert T.W., Dean D.D., Schwartz Z., "Role of material surfaces in regulating bone and cartilage cell response," Biomaterials 17(1996)137-146

[8] Paul K. Chu, "Bioactivity of Plasma Implanted Biomaterials," Nucl. Instr. And Meth. In Phys. Res. B 242(2006)1-7

[9] Wang P.E., Chaki T.K., J. Mat. Sci. Med. 4 (1993) 150.

[10] Volkert CA, J. Appl. Phys. 70 (1991)3521

[11] Lopatin C.M., PhD Thesis, Arizona State University, 1999

Chapter 4

Effect of Substrate Geometry on HA Microstructure Evolution

4.1 Introduction

The need for directing and concentrating cell growth is an increasing necessity in the tissue and scaffold engineering field [1]. As one of the ways to improve the adhesion of cells to metal substrates *in vivo* and *in vitro*, surface microfabrication has been widely used for the spatial control of cells [2]. In fact, the biocompatibility of a material has long been associated/or determined by factors, such as, surface micro-topography, micro-texture and micro-chemistry. Surface chemistry and/or topography affect the nature and strength of the interactions occurring at the biomaterial/biological interface [1-3]. Patterns have been used to direct cells and many workers have shown that well prepared patterns are able to influence cell growth, orientation and migration. The effect of surface topography on the development, motility, differentiation, orientation and alignment of cells is referred to as "contact guidance" [4]. This implies that cells tend to align themselves in the direction of the grooves. They use the morphology of the substrate for orientation and migration. Many studies have established that specific surface topography is an important factor in regulating cellular adhesion and may be used to manipulate interactions with the biomaterial surfaces [5].

Different geometrical patterns of various sizes and depth have been investigated and have shown to influence cell growth, motility and alignment. Step grooves [3, 6, 7], convex [8], concave [9] and V-shaped grooves [7, 9-15] have all been investigated. Cells in all these patterns have shown a preferential growth. The alignments were observed to be

parallel to the groove axes. It was also found that the degree of orientation depended on the cell type, groove density, groove width and groove depth. The cell alignment occurred with both radial and parallel grooves [16]. The higher the pitch (density) of the grooves the higher the degree of alignment. Similarly, alignment and elongation appeared to be directly related to groove depth [17, 18]. Kaiser JP, *et al*. investigated the role played by groove/ridge dimensions at microscale on fibroblast cell migration by correlating cell shape, migration angle, cell orientation and velocity of migration with these dimensions [7]. They showed that the surface structures significantly influenced migration direction, cell orientation and mean velocity in directions parallel to the grooves/elevations in a surface structure dependant way. The migration of cells followed a defined direction, that is, parallel to the grooves' direction while cells on the plane surfaces had no preferred direction. Similar observations were made by Lenhert, *et al.* [19]. They found that V-shaped grooves were more efficient in influencing cell migration. Adams *et al.* found that a combination of optimal surface topography and bioactive coatings acted synergistically to improve osteoblast adhesion and osteogenesis [20]. Patterned titanium surfaces were able to orient cells in the direction of the micro-channels. The morphology of the cells was also changed. They became elongated. There was a higher concentration of cells inside the micro-channels than there were either outside or on the non patterned substrates which were serving as controls. The experiment was extended by altering the surface chemistry by coating the samples under investigation with hydroxyapatite (HA). Cell orientation along the channels as well as the Form Index (FI) (which measures the elongation of the cells) was more pronounced for cells inside the channels than for cells outside the channels and those on planar surfaces. The difference between the coated and the uncoated samples was marked. Cell occupation per micro-channel dimension measurements revealed a micro-channel width that was optimal for osteoblast attachment. They found that narrow micro-channel widths promoted higher cell coverage than the wider spaced micro-channels.

Since previous studies have reported the behaviour of cells on topographical features, this thesis seeks to extend this and investigate why cells behave that way from a materials science perspective. The study also seeks to elucidate the phenomenon as to why there

was such a marked cell response inside the channels as opposed to outside the channels or on the unpatterned surfaces reported by Adams *et al.*

These goals were achieved by investigating the effects of surface topography on HA microstructure evolution. Rutherford backscattering spectroscopy (RBS), x-ray diffraction (XRD) and optical/atomic force microscopy (AFM) were used to characterize the HA. The microstructure was correlated with the surface roughness results from AFM.

4.2 Experimental methods

4.2.1 Sample Preparation

4.2.1.1 Substrate Preparation

Micro-channel fabrication, the design of micro-channel structures, used the computer program L-edit. Standard photolithography techniques were used to micro-pattern the silicon wafers. These were fabricated at the Centre for Solid State Electronics Research (CSSER) at Arizona State University. Two different types of etching processes were used; dry and wet etching methods. For wet etching process, KOH was applied to obtain micro-channels of width 222 µm, 50 µm, 35 µm, 22 µm, 12 µm and 5 µm. Reactive ions were used for dry etching process. Wet chemical etching is generally isotropic in nature i.e. the material is etched both vertically and laterally at the same rate. This results in pattern edges that are tapered. With reactive ion etching (dry etch), square edged micro-channels are realized.

The substrates etched are shown in figure 4.1. In this thesis, the pattern in Figure 4.1(a) (with decreasing channel dimensions) is referred to in this study as pattern 1 and the one in Figure 4.1 (b) (with the rectangular shape) is pattern 2.

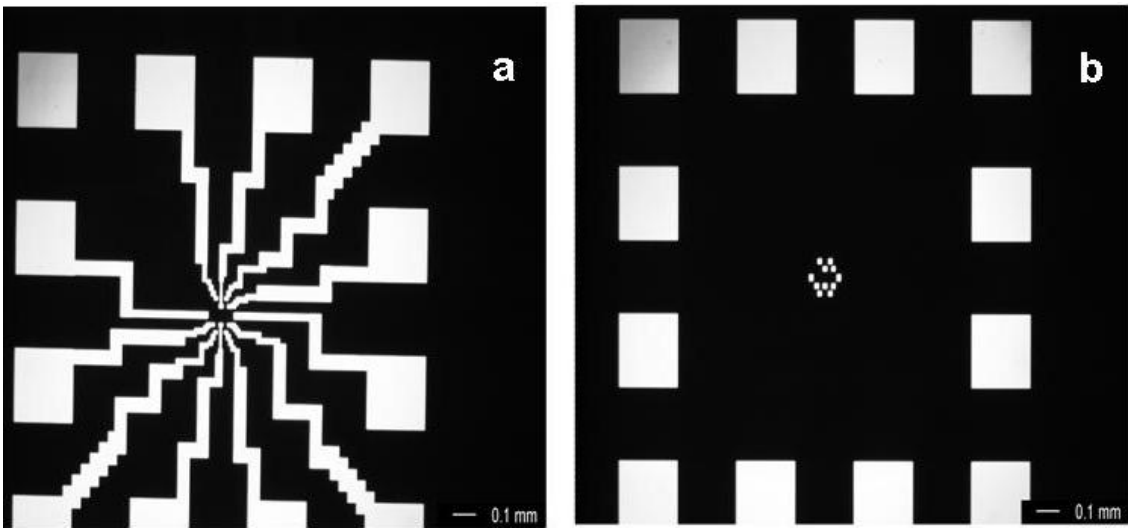

Figure 4. 1: Optical images of the etched patterns. (a) Pattern 1 and (b) pattern 2.

After the patterning processes, 1 cm x 1 cm samples of silicon were cut using a diamond scribe. Before the deposition of the metal on the substrates, they were sequentially and ultrasonically cleaned in organic chemicals and HF acid as described in section 2.3.2.

4.2.1.2 Metal Deposition

Approximately 50 nm of titanium was e-beam deposited at a rate of 2.1 Å/s with the filament current of 20 mA. After the metal deposition, the patterns were still observed on the substrates.

Eight substrates, three wet etched pattern 1 (A, B and C), three unpatterned substrates acting as control (D, E and F) and two dry etched patterns one of pattern 1 (G) and the other of pattern 2 (H) were used. Table 4.1 summarizes the substrates used.

Table 4. 1: Table showing firing conditions of the samples. Letters identify samples.

	Firing Temperature		
	650°C	750°C	850°C
Wet etched Pattern 1	A	B	C
Control (Unpatterned)	D	E	F
Dry etched pattern 1	-	-	G
Dry etched pattern 2	-	-	H

4.2.1.3 Hydroxyapatite Deposition

Before the spinning procedure, any dust particles that might have adhered on the sample were removed. A 0.1 M sol was spin coated on the substrates. The samples were spun at a rate of 4000 rpm for 10 seconds. The ambient was carefully monitored as the relative humidity was in the range of 13-16%. Immediately after spin coating, the samples were dried on a hot plate at 300°C for 3 minutes.

4.2.1.4 Sintering of Hydroxyapatite

After drying the samples were then fired in air at various temperatures using a Lindberg tube furnace. The samples were all fired for five minutes. Table 4.1 shows the firing temperature on each sample.

4.3 Characterization Techniques

The techniques used to characterizing the HA thin films included XRD, RBS, Optical microscopy and atomic force microscopy.

X-Ray Diffraction (XRD)

XRD was used to compare the crystallinity as a function of geometry and firing temperature. A 3^o glancing angle scan was used with the Philips diffractometer located at Arizona State University (ASU). The step width of the scan was 0.02^o. These scans were on the whole sample not just on the channels. Therefore the result of the scan is the cumulative peaks of all the crystallite planes on the entire sample.

Rutherford Backscattering Spectroscopy (RBS)

RBS was used to confirm the chemical composition of the films, the thickness and the Ca/P ratios. A 2 MeV He^{++} beam was used. The sample tilt angle was set at 10^o to avoid channeling effects and the scattering angle was set at 165^o. The beam current was as low as possible to avoid beam damage on the sample. In spite of this precaution, the beam left a circular spot on the sample. The data was analyzed using the RUMP simulation program.

Microscopy

Optical microscopy was used to observe the patterns and evaluate their quality at lower magnifications. Atomic Force Microscopy was used to obtained information on the morphology, crystallite size and roughness. The V700 Nanoscope located at iThemba LABS, Faure South Africa, Materials Research Group (MRG) was used. A 5 μm x 5 μm image was taken on each sample. For each patterned sample, an image was taken from the inside of the channel as well as the outside. The roughness and the crystallite sizes were then compared.

4.4 Results and Discussion

4.4.1 Crystallinity and Phase Identification

XRD was used to evaluate crystallinity in the HA/Ti/Si system. The XRD spectra for the HA prepared on different substrate geometries and fired at temperatures ranging from 650-850^{o}C were obtained. Figure 4.2 shows spectra for the wet etched; pattern 1 sample (A, B and C). Figure 4.3 shows spectra for the dry etched (sample G), pattern 1 and pattern 2 (sample H) all fired at 850^{o}C. The spectra for the control samples, in this case the unpatterned samples are shown in Figure 4.4. Figure 4.5 compares the spectra for the different patterns and different etching processes that is, wet etch and dry etch, with the control. The identified peaks are indicated by stars and crosses while the unidentifiable peaks have not been indexed. There is no explanation as to the existence of these peaks.

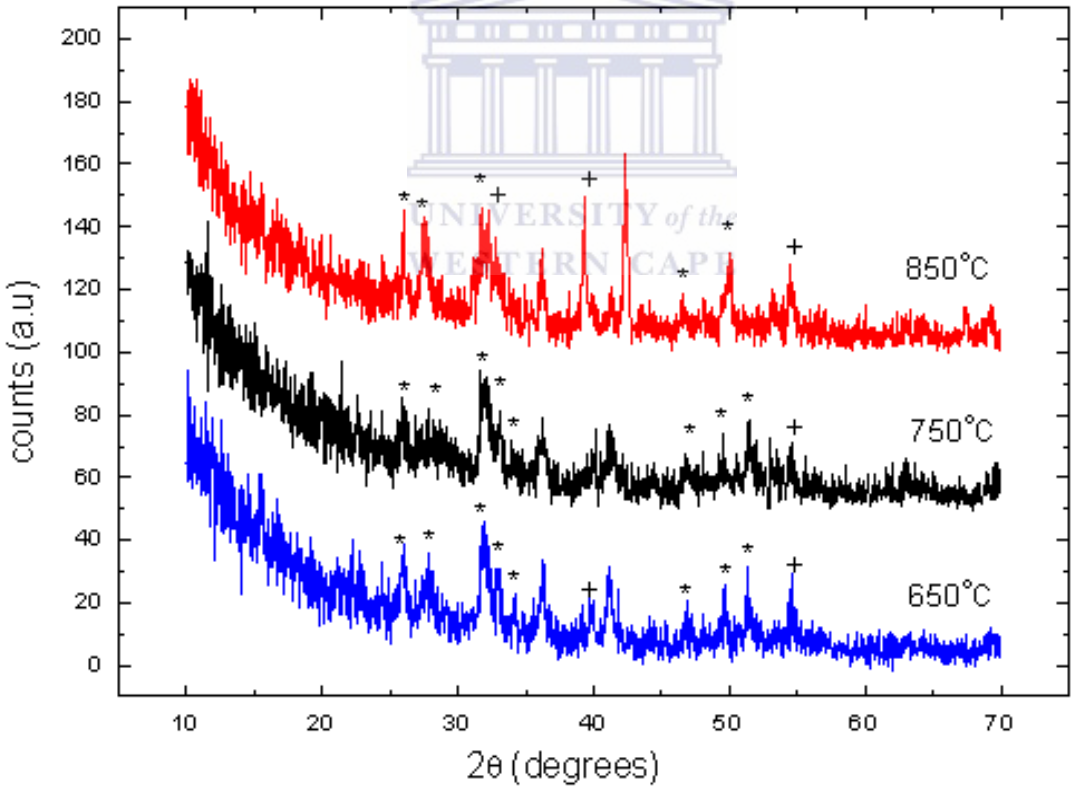

Figure 4. 2: XRD spectra for the wet etched pattern 1 fired at different temperatures with the index * representing HA peaks and + indicating peaks for Ti, Si and other Ca-P phases.

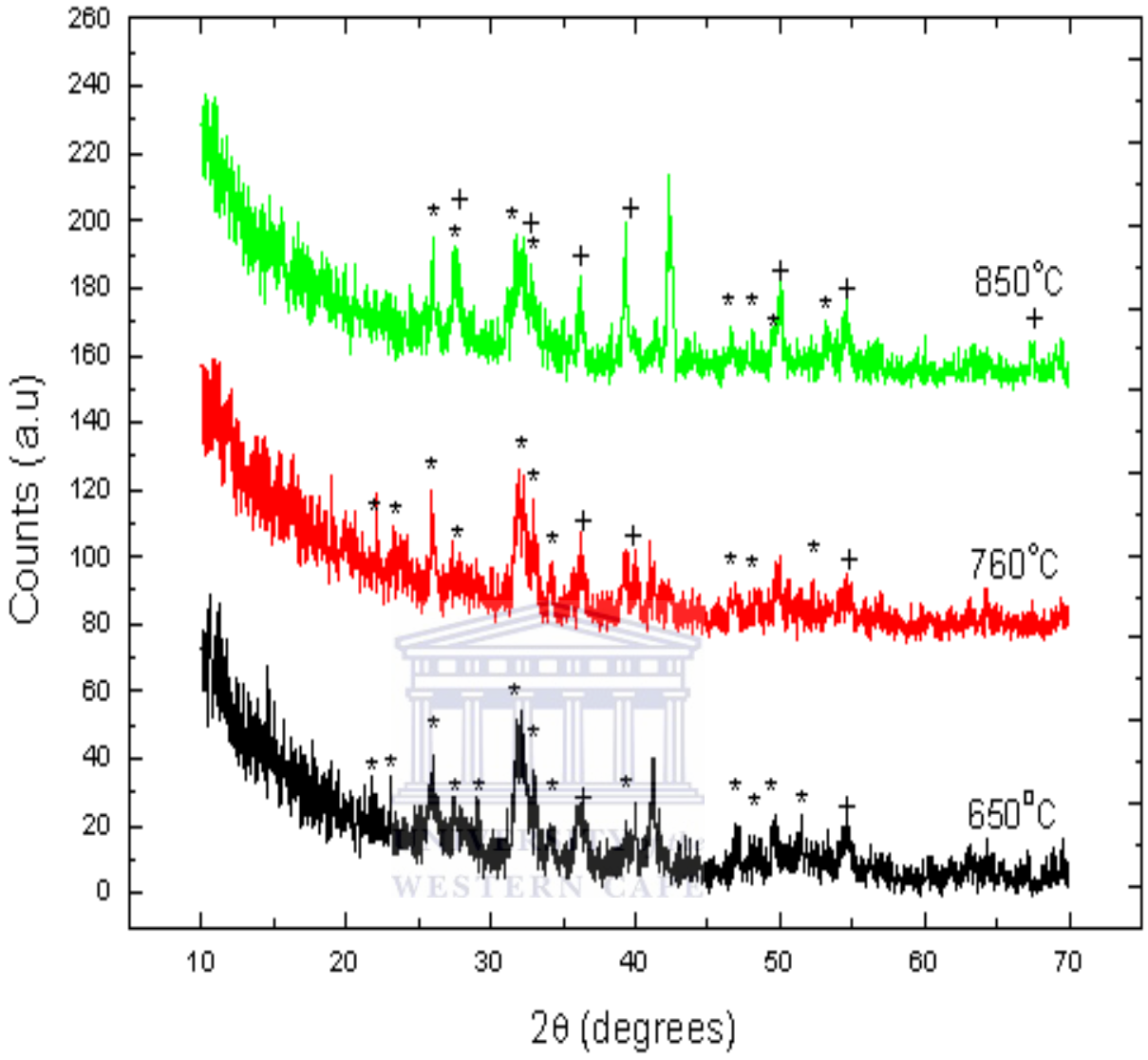

Figure 4. 3: XRD Spectra for the control (non patterned) samples fired at different temperatures for five (5) minutes each. In these spectra the index * represents HA peaks and + indicates peaks for Ti, Si and other Ca-P phases.

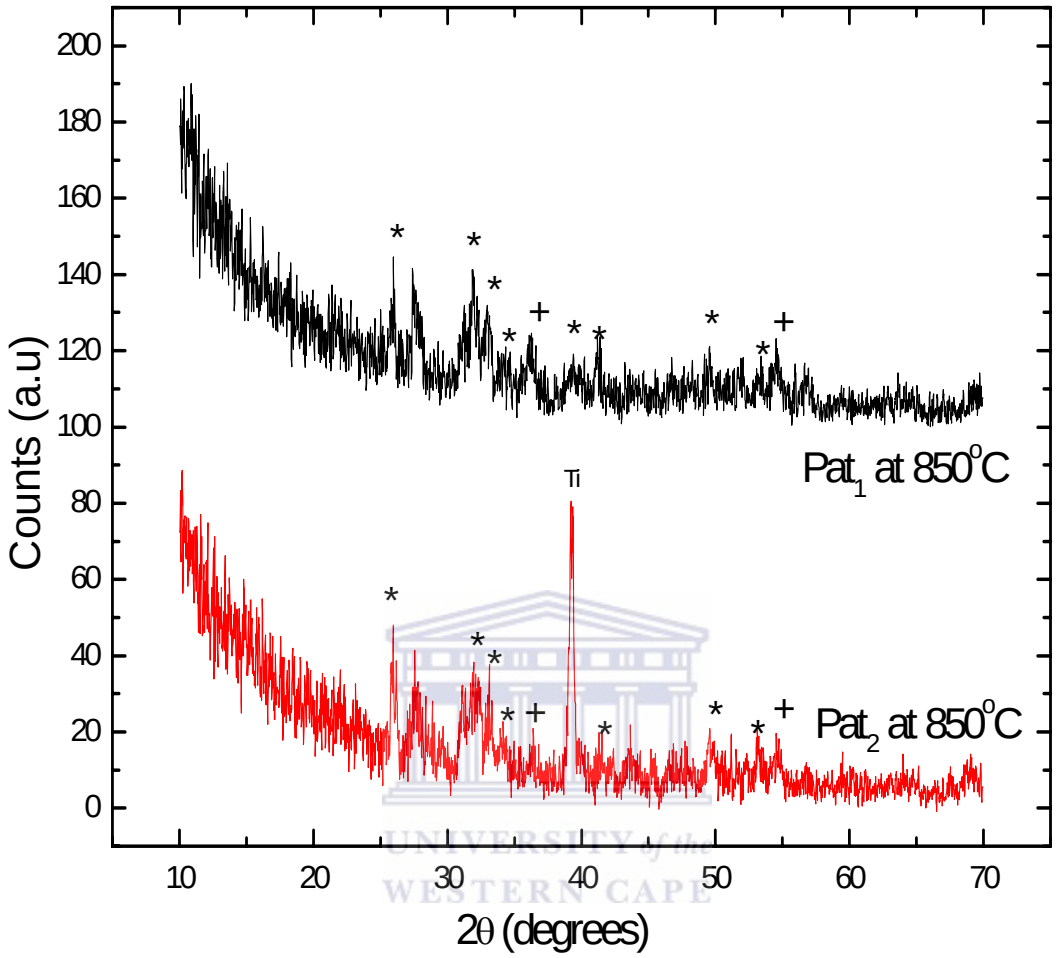

Figure 4. 4: XRD spectra for HA fired at 850°C on different dry etched patterns, pattern 1 and pattern 2. In these spectra * denotes HA peaks while + denotes other Ca-P peaks other than HA.

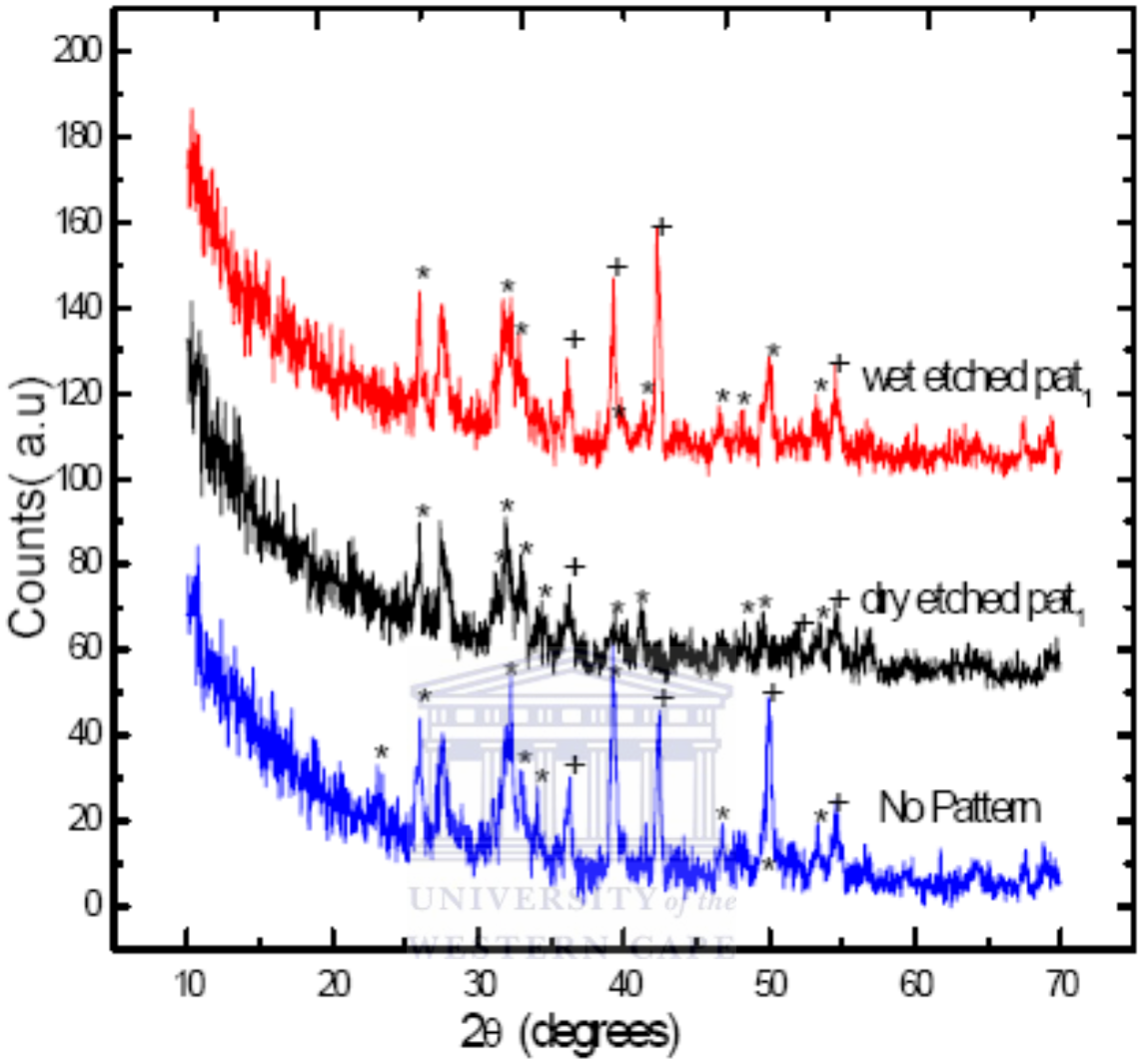

Figure 4. 5: Comparison of XRD spectra of wet etched pattern 1, dry etched pattern 1 and the control all fired at 850°C with * indexing HA peaks and + indexing other Ca-P phase peaks. Peak heights for wet etched samples are more than the dry etched ones.

With regard to the HA microstructure evolution as a function of geometry or substrate pattern, XRD does not provide significant information. This is because the solid angle of

the X-ray beam directed on the sample spans the entire sample not an individual pattern feature, therefore the XRD spectrum of a patterned sample is an average of the patterned and the unpatterned area. This is also the observed reason why there are no differences between the etched and control samples in Figures 4.2 and 4.3 respectively.

Fully crystalline HA starts to form at temperatures above 500^{o}C in the first few seconds. At temperatures above 800 ^{o}C, HA transforms to other phases like calcium oxide (CaO) and tetra calcium phosphates (TCP) due to de-hydroxylation [21]. Therefore, pure crystalline HA is expected at temperatures used in this experiment.

To determine if geometry affects microstructure of HA, XRD was used. Therefore peaks and their intensities were essential. For easy measurement, the 211 peak located at 31.77^{o} was used as it has the highest peak. From Figure 4.2, XRD pattern of the HA film on a wet etched pattern 1 shows that almost all the peaks are present and they correspond to the HA standard [22].

A difference in peak height can be observed between the dry etched pattern 1 and pattern 2 as shown in Figure 4.4. The peak height of the spectrum from the pattern 1 was slightly more than that of pattern 2. One suspected reason for the difference is that the pattern 2 sample has more planar (flat) surfaces than the pattern 1 and hence less capability to retain liquid (sol) than the pattern 1 which has channels which cover the sample, hence the difference in peak height.

The diminishing trend of peak heights from the unpatterned and patterned samples are noticeable though the peaks for the patterned samples are slightly higher than the unpatterned ones. Since the intensity is dependent on the number of planes and amount and size of crystals, the surface with the ability to retain much HA sol during the high speed spinning is expected to have intense XRD peaks. Unpatterned substrates are suspected to lose much sol during spinning due to high outward radial forces. As for patterned substrates, as evaporation proceeds and viscosity of the sol increases, even high spinning speeds would not drive the sol out of the channels of the patterns and so it

remains there as will be shown in AFM micrographs. This is the suspected reason why patterned samples have slightly higher peak intensities than the unpatterned counterparts as shown in Figure 4.5.

4.4.2 Composition

To confirm the elemental composition of the HA film, RBS was used. Figure 4.6 compares the RBS spectra of a dry etched pattern 1 and pattern 2 HA samples fired at 850 ^{o}C. All the elements that make up HA can be observed. However, there is a difference in peak heights in the pattern 1 and pattern 2 samples. From Figure 4.6, the elemental peaks corresponding to HA look similar and so it can be concluded that crystalline HA is obtained regardless of the geometry of the substrate. These results confirm the XRD results obtained. The spectra for the wet etched pattern 1 as a function of temperature are shown in Figure 4.7.

Figure 4.8 to Figure 4.9 show the comparisons between the spectra of patterned and unpatterned samples. All the figures show similar results as the elements present in the samples can be clearly deduced. Additionally, as with XRD, the RBS on different geometry of substrates does not provide information on the microstructure evolution of HA as all the elements can be seen regardless of the firing temperature.

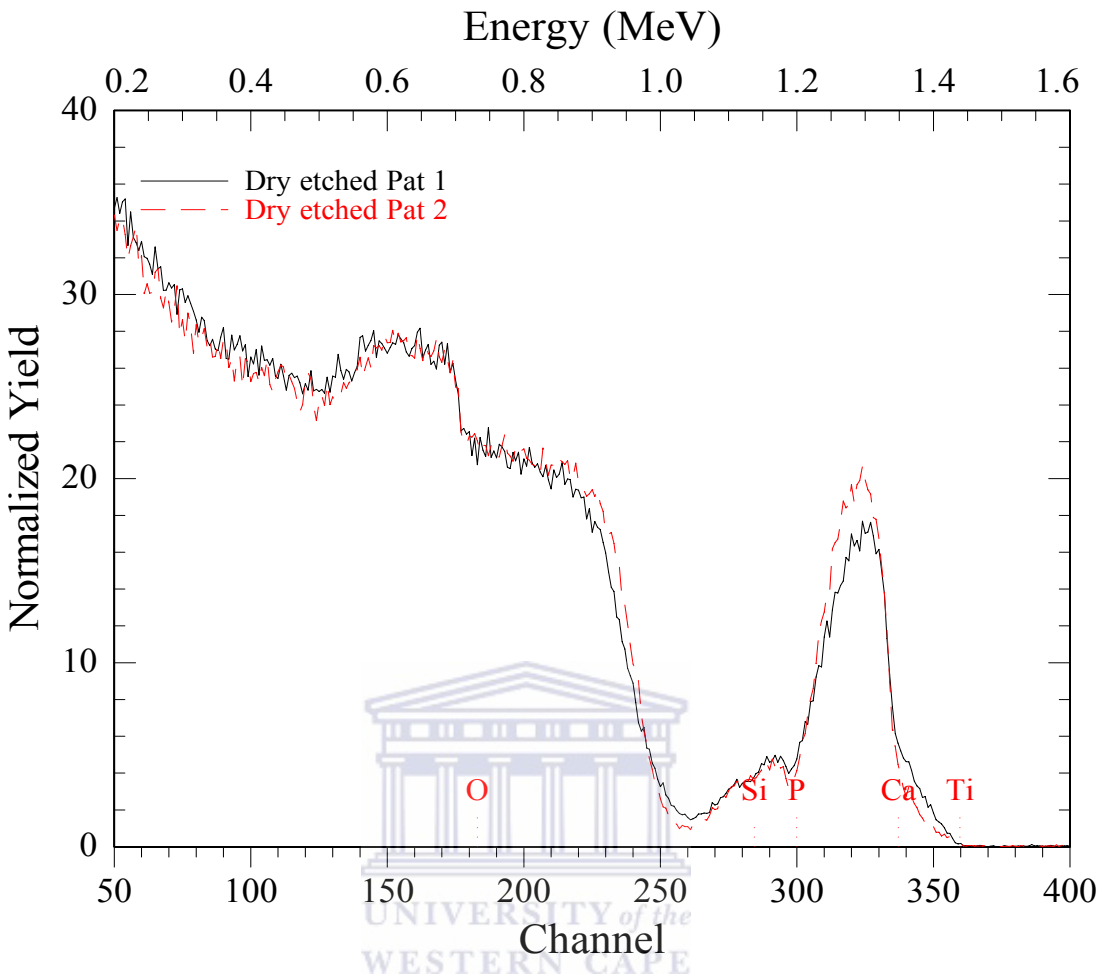

Figure 4. 6: RBS spectra for dry etched pattern 1 and pattern 2 all fired at 850 ^{o}C. Solid line represents pattern 2 while the dashed line represents the pattern 1.

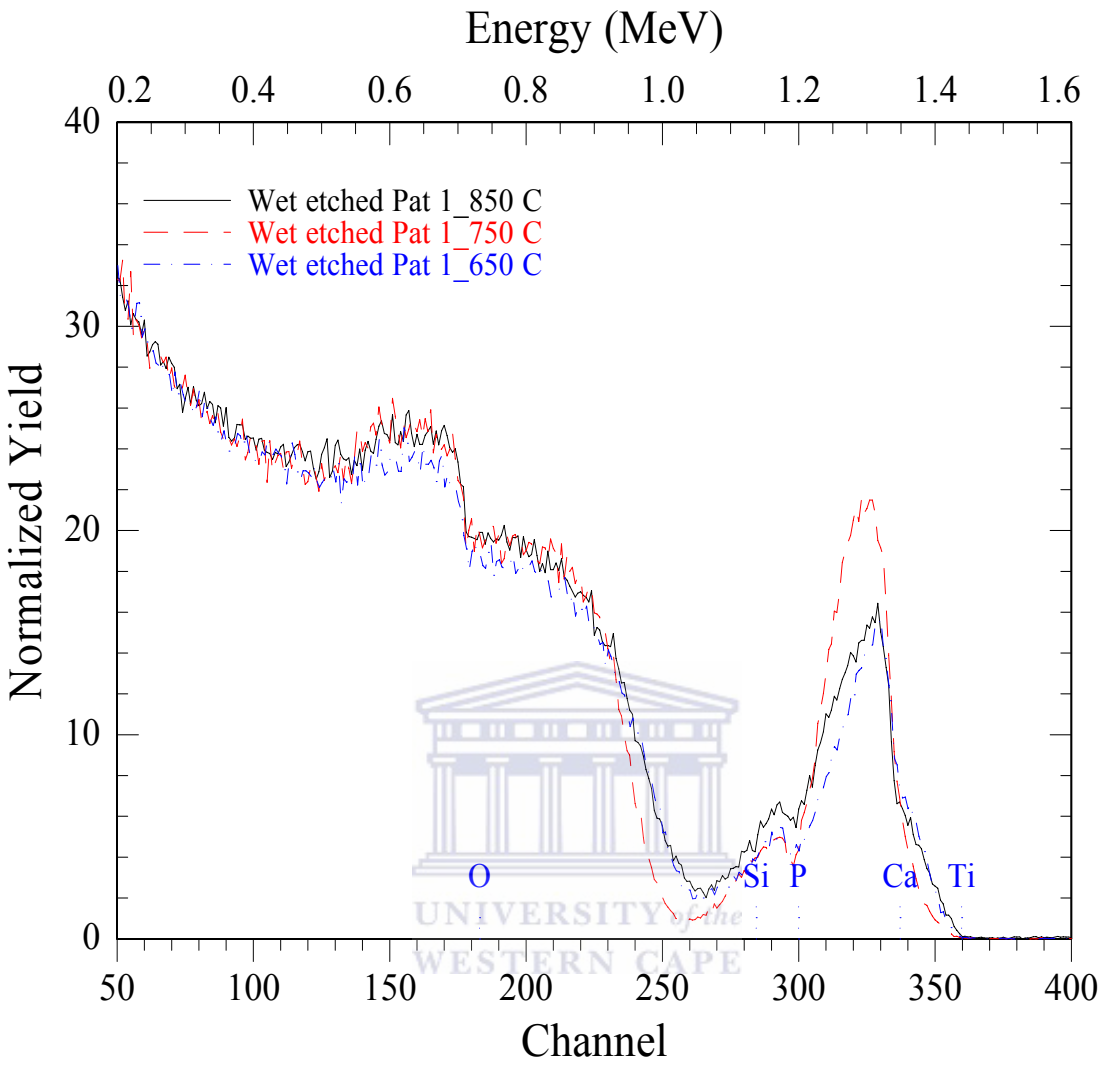

Figure 4. 7: RBS spectra for the wet etched pattern 1 HA samples fired at different temperatures. The solid line represents firing temperature of 850^{o}C, dashed line, 750^{o}C and dash-dot at 650^{o}C.

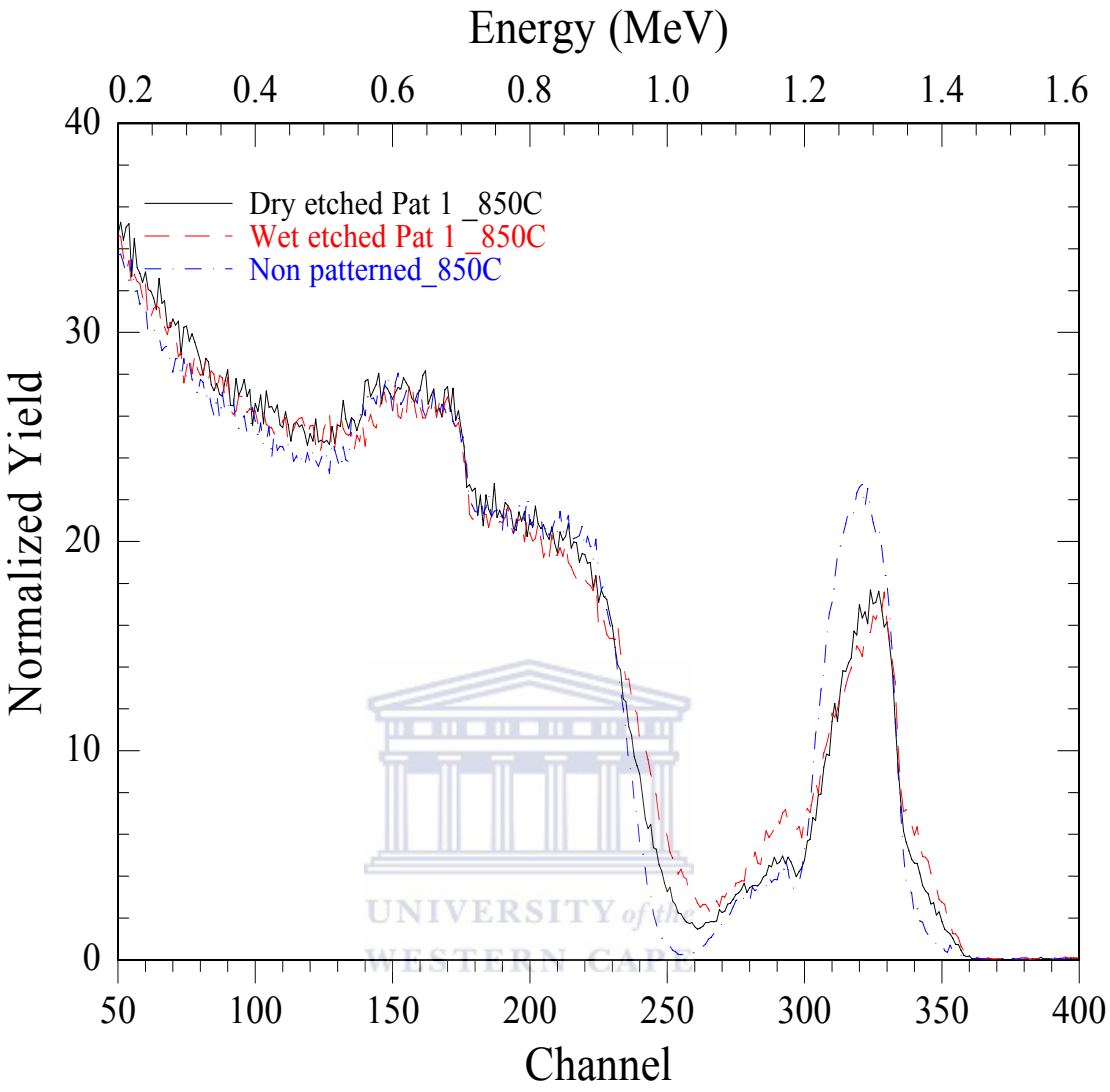

Figure 4. 8: RBS spectra of dry etched and wet etched pattern 1 compared with the control all fired at 850°C. The dashed-dot line represents unpatterned, solid line represents the wet etched and the dashed line the dry etched.

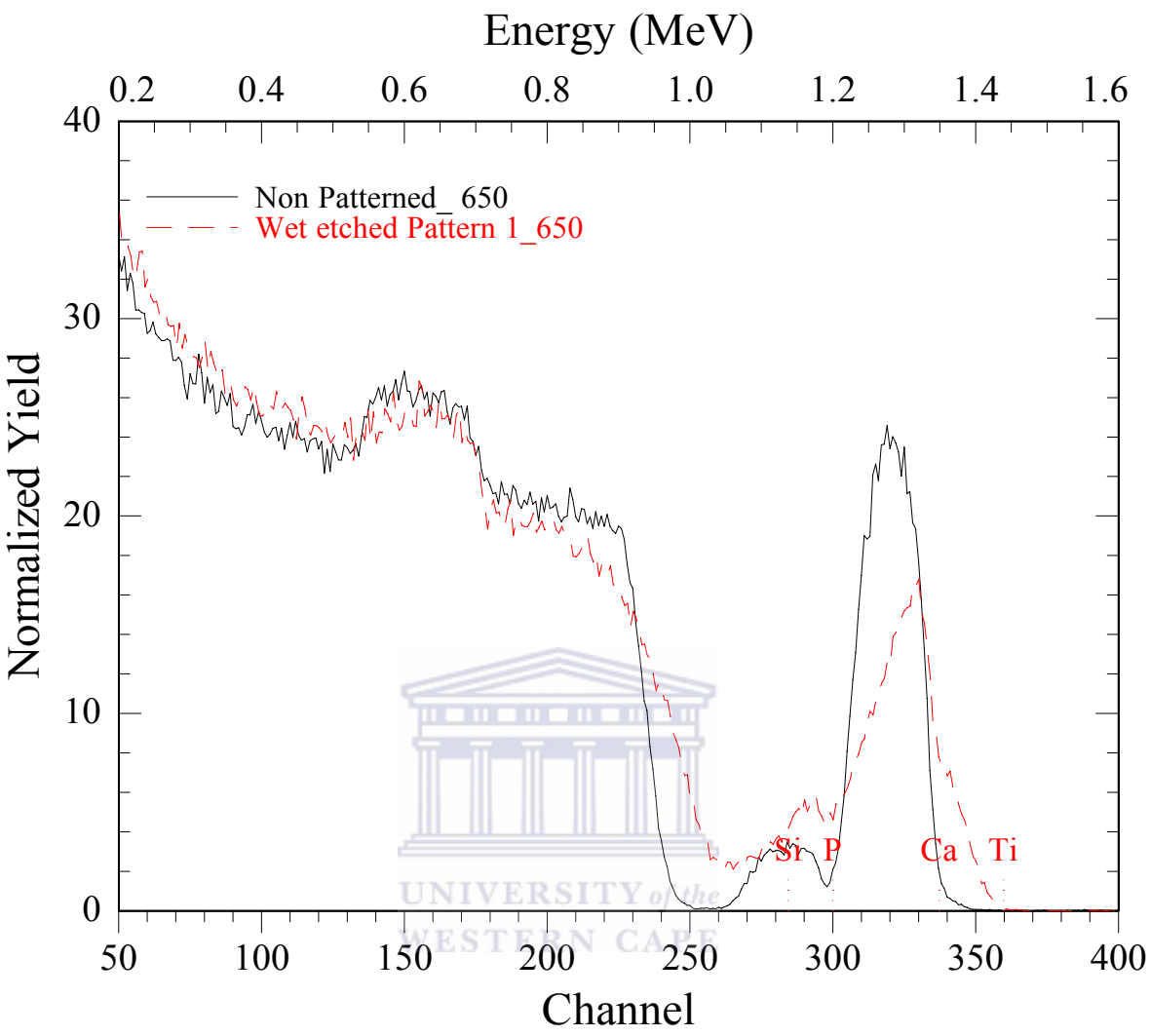

Figure 4. 9: RBS spectra of wet etched pattern 1 compared with the unpatterned, both fired at 650°C.

As can be observed from Figure 4.8, the non-uniformity of the spectrum of patterned substrates as compared to the non-patterned substrates is caused by the differences in the distribution of the HA on the sample substrates, that is, there is more HA in the channels and less HA outside. However, for the non-patterned substrate, the HA is uniformly distributed hence the spectrum is defined and is as expected. This also proves that substrate geometry has an effect on HA evolution.

4.4.3 Morphology and Grain Size

Optical microscopy images on patterned Ti substrates were obtained. These include the dry and wet etched pattern 1. Fig 4.10 shows the HA coated pattern 1 substrates: (a) the dry etched pattern and (b) shows the wet etched pattern.

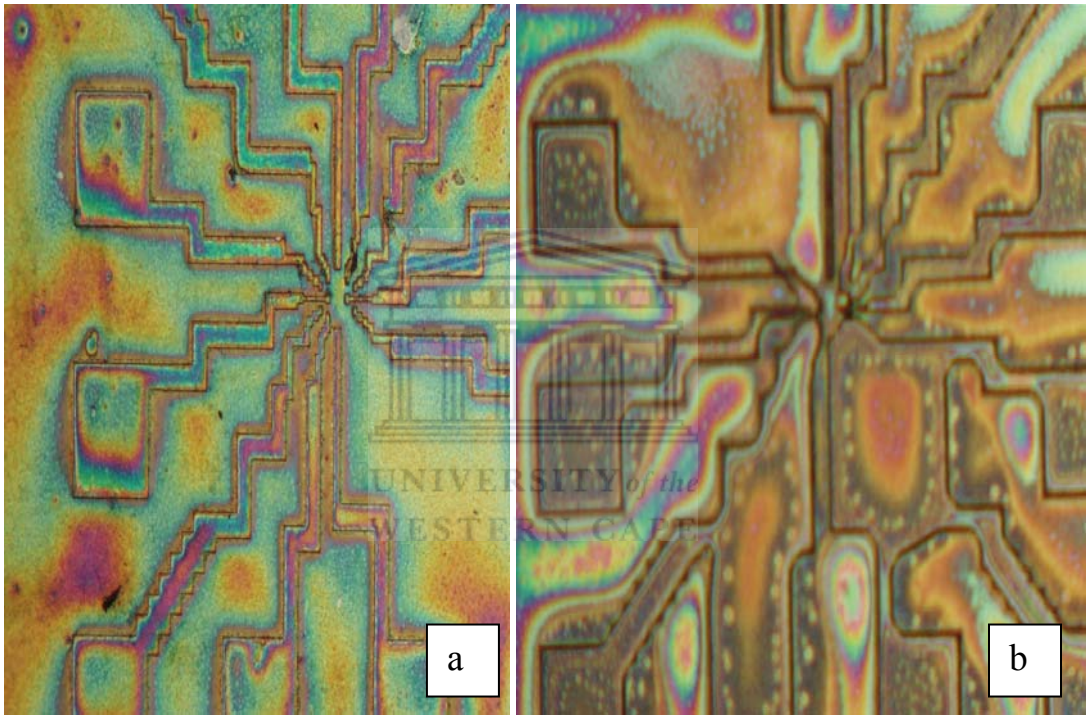

Figure 4. 10: (a) HA on dry etched pattern 1. (b) HA on wet etched pattern 1. The edges of the dry etched channels are sharper than those of the wet etched channels.

When the precursor sol is spun on the patterned substrates, the inside of the channels are also coated. The morphology of the HA was compared with that outside the channels using AFM. Fig 4.11 shows an optical image of the HA located inside the channel of the dry etched pattern 1 substrate. Sharp edges can be observed.

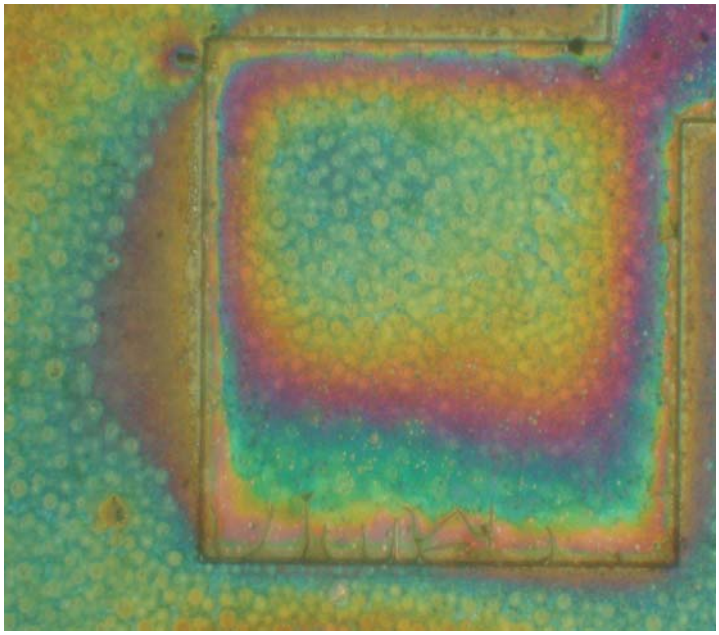

Figure 4. 11: An optical image of an HA on a dry etched patterned substrate.

Wet etched surfaces as opposed to dry etched surfaces have tapered edges due to the fact that chemical etching is limited by crystal planes in silicon and so etching generally stops on certain crystal planes in the substrate. Therefore since planes cannot be vertical to the surface, the channels are not sharp. This effect is usually observed in <100> silicon [23]. This is expected to have happened as the <100> silicon was used in this thesis. This has an advantage as this increase the sites for heterogeneous nucleation of grains [24]. In contrast, dry etched (sharp edged) substrates have less surface area for nucleation. This is elucidated in the AFM studies in the next section.

Atomic Force Microscopy (AFM).

The surface morphology of the patterned HA film was evaluated using atomic force microscopy. The surface morphology was evaluated inside and outside the channels. The roughness and HA grain sizes were correlated. Figure 4.12 shows a dry etched pattern 1 image taken inside the 5 μm wide channel

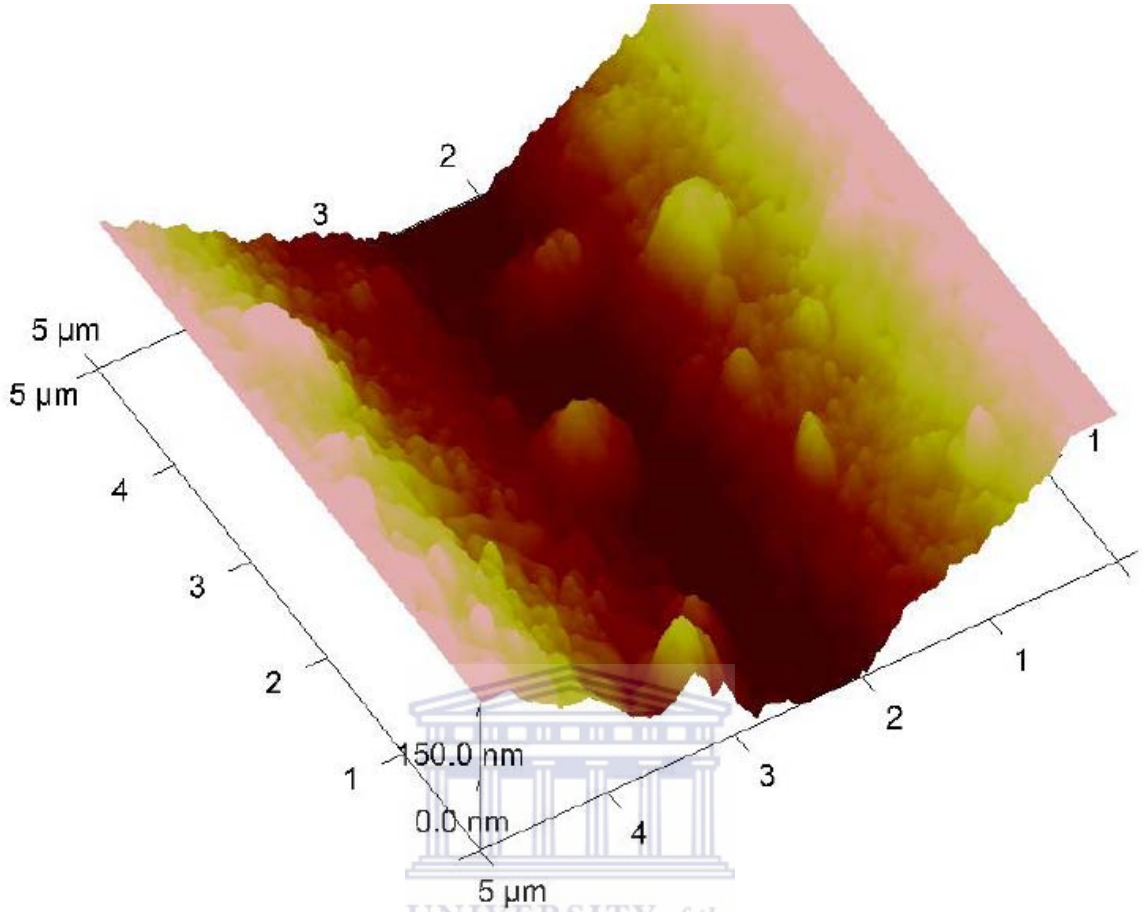

Figure 4. 12: Atomic force micrograph of an HA film on the dry etched pattern 1 substrate taken inside the 5 µm wide channel. The film was fired at 850^{o}C for 5 minutes. The non-uniform coatings of the edges are due to shadowing during the spin-on process.

Very small grains as well as bigger elongated grains can be seen inside the channel. Bigger grains are shown to be due to smaller grains clustered together to form these elongated grains.

Roughness is dependent on the size of the individual granules. Therefore the knowledge of roughness was used qualitatively as an indicator of crystallite size. The topographical

description of the surfaces using a three-dimensional numerical evaluation was used. The profile parameters used for the evaluation of the amplitude (height) of the surface were R_a and R_q. R_a being the arithmetical mean deviation of the profile while R_q being the root-mean square deviation of the profile. Inside the channel, the roughness of a surface feature image R_a was found to be 87.1 nm while the R_q was found to be 103 nm. Similarly, the roughness over a (1 µm x1 µm) square area was determined. Figure 4.13 shows an enlarged AFM micrograph for the area on the outside of a channel of a dry etched pattern 1 substrate.

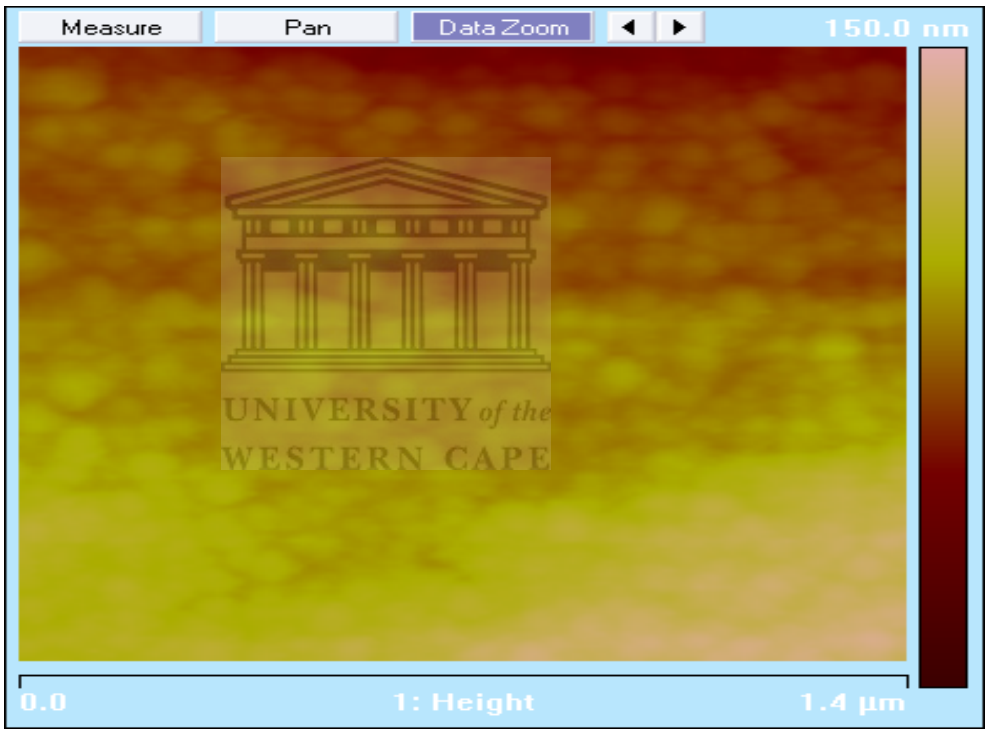

Figure 4. 13: AFM image of the flat area outside of a channel. Small grains can be seen.

Table 4.2 shows the results of the roughness measurements. It can be seen that the inside channel has higher roughness hence bigger grains than the outside channel.

Table 4. 2: Roughness results of the inside and outside of the 5 µm wide channel of the dry etched pattern 1.

	Roughness measurements for the Dry etched pattern 1	
	Inside channel	Outside channel
R_a (Image)	87.1 nm	34.8 nm
R_q (Image)	103 nm	43.6 nm
R_a (1 µm x1 µm)	9.4 nm	3.59 nm
R_q (1 µm x1 µm)	13.2 nm	4.53 nm

Similar results for the dry etched pattern 1 sample also show that roughness inside is greater than outside. Larger grains are observed in the channels than on the surfaces outside. Figures 4.14 and 4.15 are images for the inside and outside of the dry etched pattern 2 respectively.

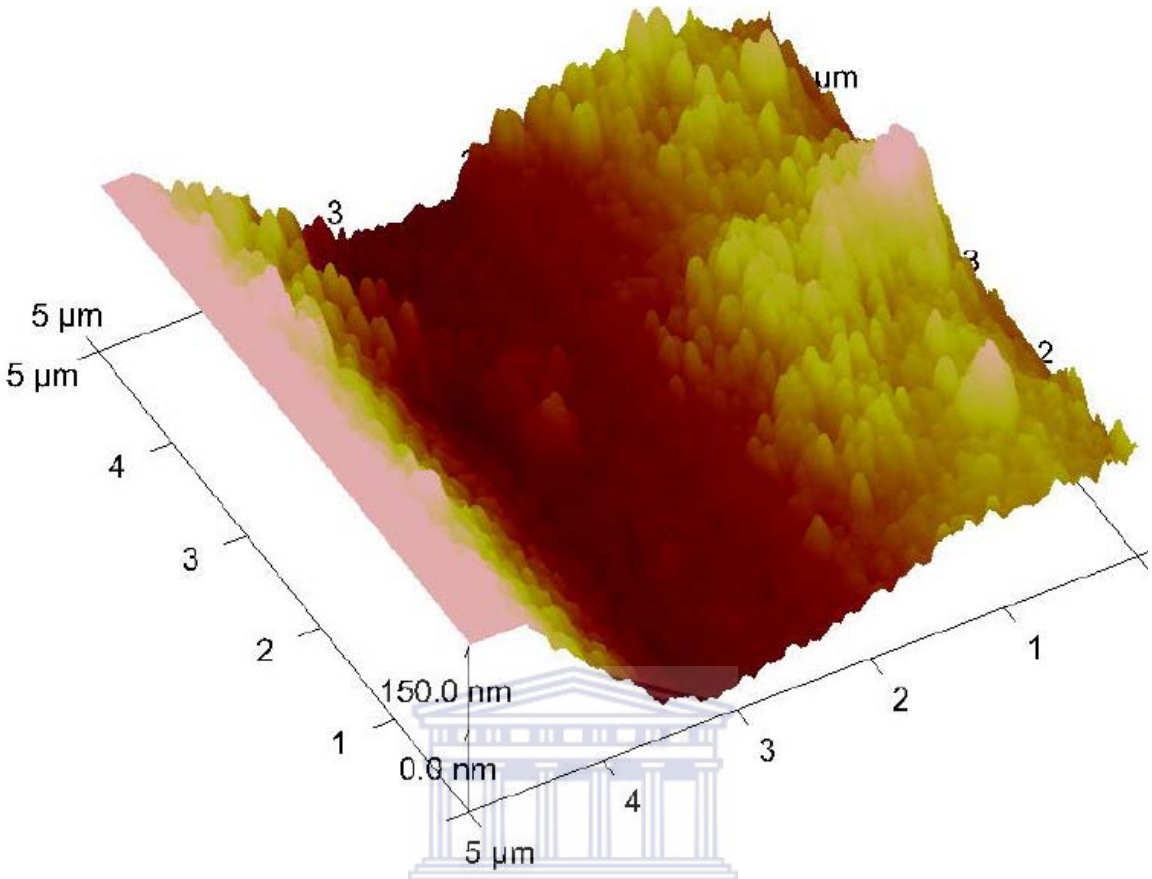

Figure 4. 14: AFM micrograph for the film fired at 850^{o}C for 5 minutes, inside the channel of the dry etched pattern 2 substrate. Elongated grains can be observed.

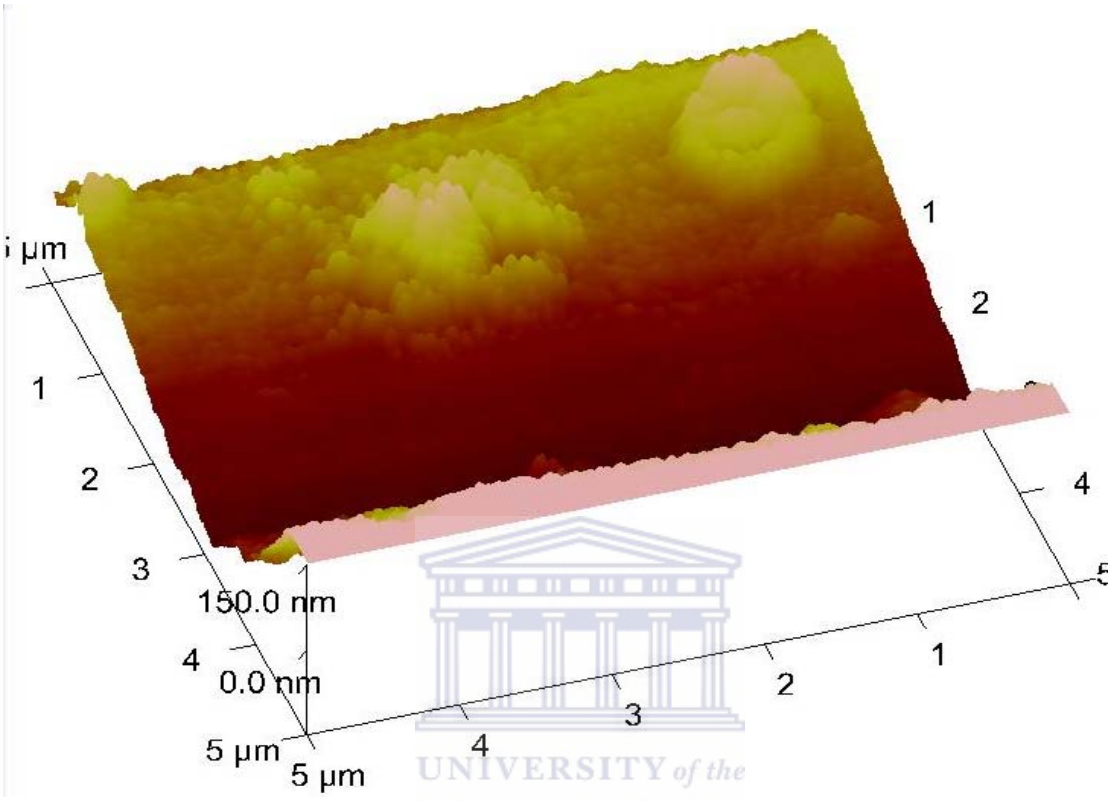

Figure 4. 15: AFM micrograph for the film fired at 850^{o}C for 5 minutes, outside the channel of the dry etched pattern 2 substrate.

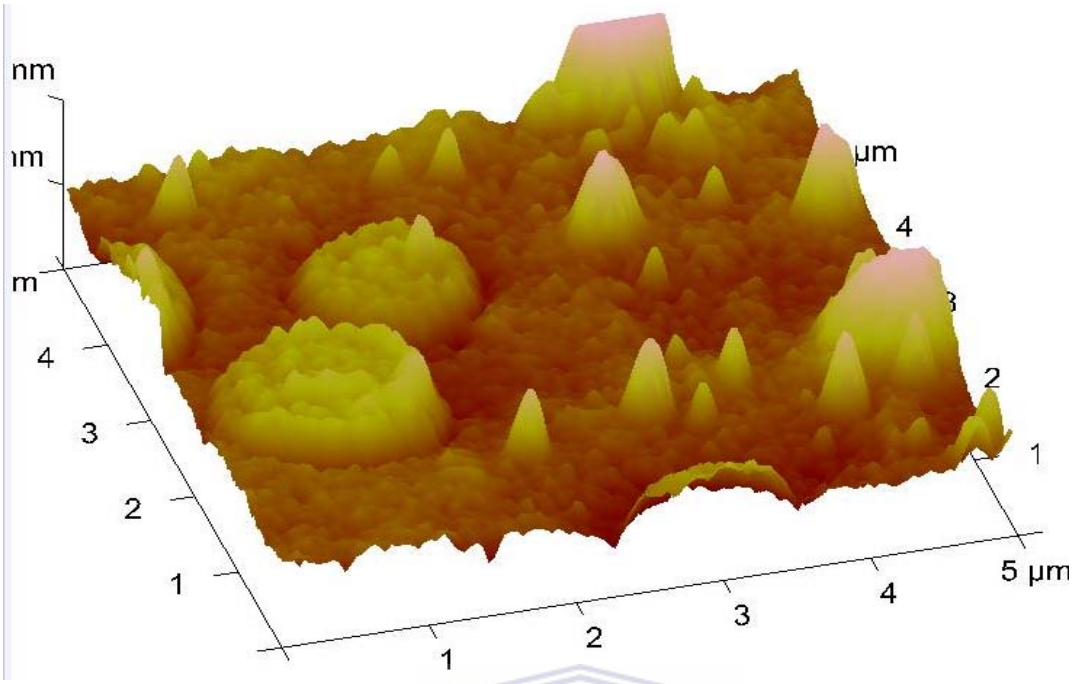

(a)

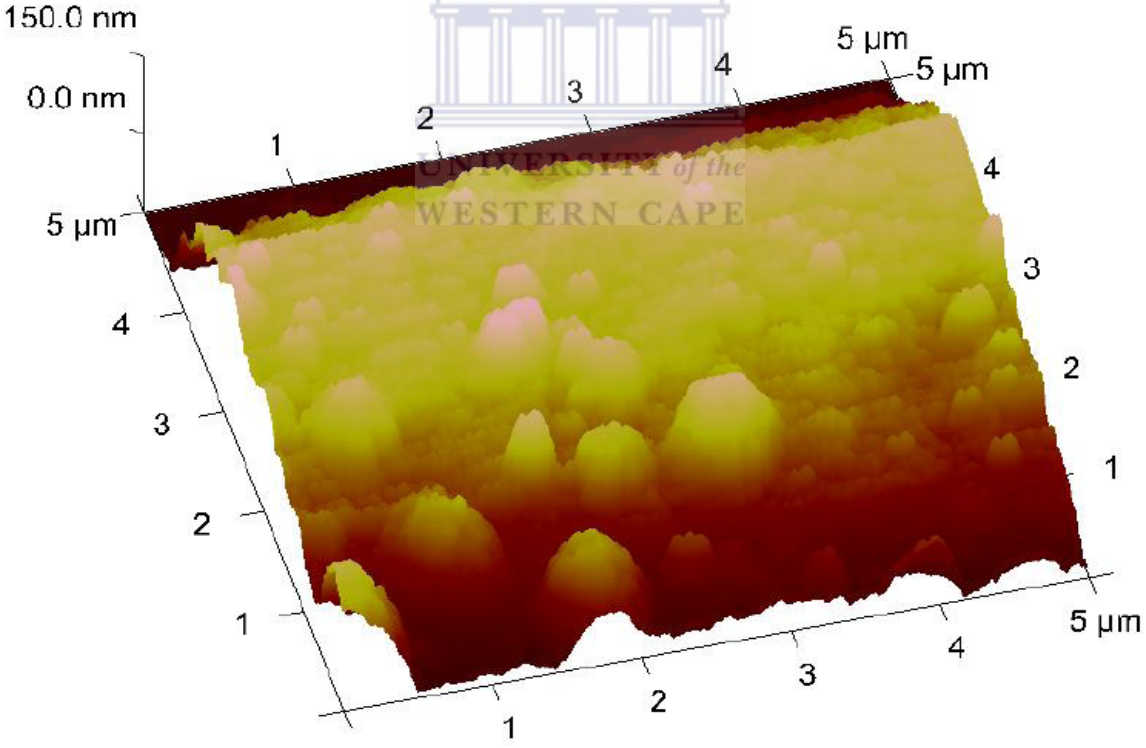

(b)

Figure 4. 16: AFM micrograph for the films inside the channels of the wet etched substrates. (a) film fired at 750°C and (b) for the film fired at 850°C. Agglomerated grains can be observed.

Figure 4.16 shows images for the inside of the channels of wet etched substrates fired at 750^{o}C and 850^{o}C respectively. Grains are observable which are elongated and some clustered together.

Table 4.3 shows the roughness results. High density of bigger grains can be observed on the inside channel also contributing to the high value of roughness.

Table 4. 3: Roughness results for the HA film on the dry etched pattern 2 substrate.

	Roughness measurements for the dry etched pattern 2	
	Inside channel	Outside channel
R_a (Image)	71.1 nm	66.7 nm
R_q (Image)	83.8 nm	78.6 nm
R_a (1µm x1µm)	14.8 nm	5.93 nm
R_q (1µm x1µm)	19.3 nm	6.93 nm

HA roughness inside the channels as can be seen from this table is consistently higher than outside the micro-channels.

Figure 4.17 shows a plot of roughness (grain size) against the firing temperature of the HA films (inside the channels) on the wet etched pattern 1 samples. The roughness increased with firing temperature.

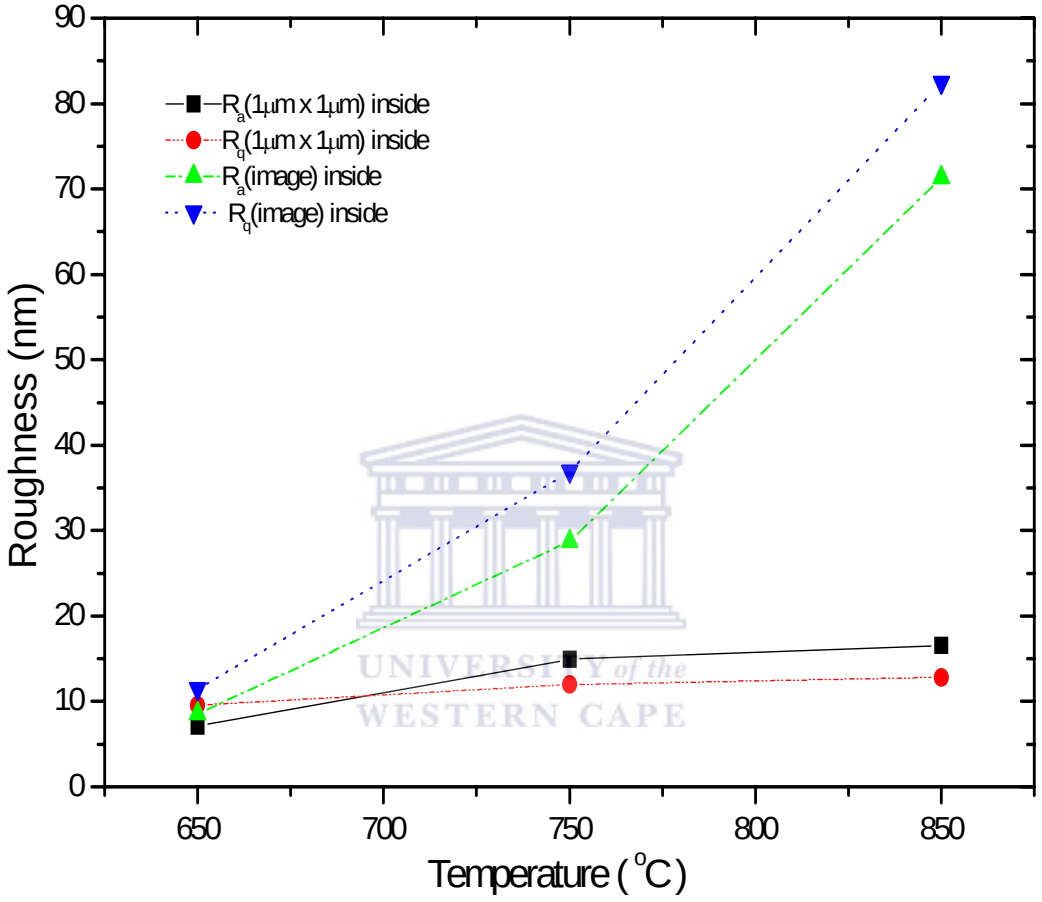

Figure 4. 17: Plot of roughness (R_a and R_q) of an HA film inside the channel of a wet etched pattern 1 substrate against the firing temperature. The roughness increased with the firing temperature. This implies the grain size increased with temperature.

The comparison of roughness of HA films on wet etched patterned substrates with the roughness of unpatterned substrates is shown in the linear fit of Figure 4.18. The

roughness on the patterned substrates increased with temperature while on the un-patterned substrates shows no or less growth. In the temperature range investigated, there was a linear increase of roughness (grains). The rate of increase of roughness with temperature inside and outside the micro-channels was almost the same as the slopes are almost equal i.e. 0.04755 nm/^{o}C and 0.04045 nm/^{o}C for HA films inside and outside respectively. However, the roughness inside was greater than outside the channels and also greater than on the un-patterned substrates.

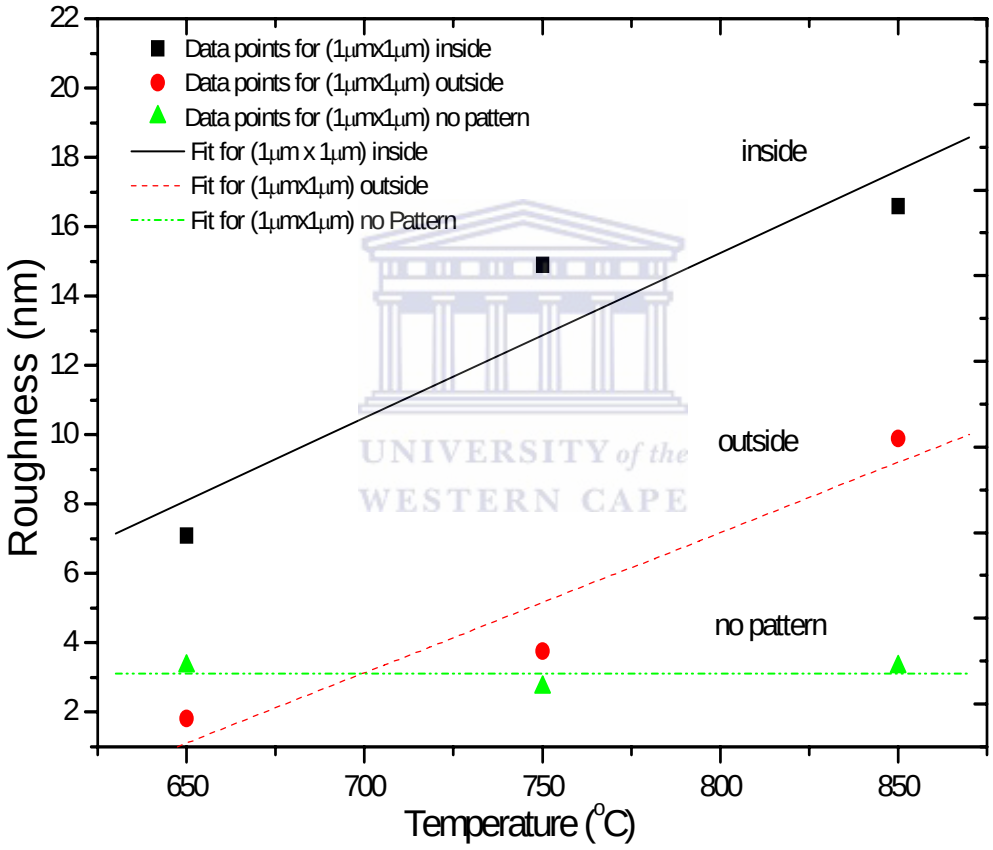

Figure 4. 18: Comparison of roughness of HA films on wet etched patterned substrates with those on unpatterned substrates. Slopes are the same for the patterned samples both inside and outside the channels while the non-patterned is almost zero.

The effect of geometry on microstructure was established by determining the roughness of the surfaces. As was observed from the AFM micrographs, the HA grains contributed to most of the surface roughness. Therefore the roughness was correlated with grain size. The more rough the region, the more and bigger the grain sizes are. Through the comparisons of surfaces inside the channels and outside the channels as well as the films from non patterned substrates, the effects were observed. The correlation of grain size and roughness in this study is only applicable to the smaller grains and not the larger grains. This can be observed from the micrographs as only the sizes of the smaller grains are comparable to the roughness while larger grains do not.

The investigation of HA microstructure in different regions of the patterned samples exhibited some manifestly different morphologies. Regions with higher surface roughness and hence large HA grain sizes exhibited grains which appeared faceted, pyramidal and elongated. This elongation may be due to the fact that the film was formed by spinning the sol at very high speeds where large radial forces are present. This is reasonable since the solidification occurs during the spinning process. Lopatin *et al*. in his work with sol gel derived HA also found that films appeared to consist of grains which were faceted and elongated with an aspect ratio of 2 [1]. This effect was also observed by Brinker *et al*. in his work with silica gels. They found that the shear forces found during spinning caused film alignment [25]. This is because spinning establishes shear fields that are able to influence the structure of the depositing film. Therefore, during spinning, a stronger gradient normal to the substrate is established in which the shear stress increases with radius and spin rate. Consequently, these shear stresses would induce alignment of the precursor species parallel to the direction of the applied shear [25].

Comparison of the image inside the channel for the dry etched pattern 1 of the film fired at 850^{o}C in Figure 4.12 with the image taken outside the channel in Figure 4.13 show a distinct difference in the roughness and grain size. The roughness inside the channel was approximately three-fold (as shown in Table 4.2) that of the surface outside, with the surface inside the channel having larger grain sizes. Similar results are confirmed in

Figures 4.14, 4.15 and 4.16 and Table 4.3. This is suspected to be due to the sol trapped in the channels and more importantly the confinement offered by the channels to nucleation sites. Since these sites are close to each other then as the temperature is increased the grains grow and coalesce to form bigger grains and these are the ones responsible for the increased roughness. The outside of the channels has fewer grains as most of the sol has been swept by the radial forces during the high speed spinning as well as there are less nucleation sites per given area.

A plot of roughness (grain size) against the firing temperature revealed that the grain growth does not increase continuously with the increase in temperature but becomes constant at some point. Despite the fact that solidification of a film occurs during the spinning process, the increase in viscosity is not sudden such that solidification happens suddenly. It seems that solidification and thus also grain growth (which is thermally dependant) occurs gradually as shown in Figure 4.17. The grains grew slowly until the temperature of 750^{o}C was attained and then stabilized. The value for the roughness for the whole image is not a good indicator of the film. This is because one big hump on the surface that is relatively smooth surface will to a large extent make the roughness reading (for the entire image) read higher than expected. This is the reason for the observed deviations with the graph from the (1μm x 1 μm) square.

The plot for the film on a non-patterned substrate in Figure 4.18 shows virtually no growth of grains despite the temperature increase. This is suspected as alluded to earlier to be due to the fact that the nucleation sites are far apart such that there is less aggregation of grains during growth [26]. Therefore it is suspected that the "open area," on the flat surface, allows the sol to be swept out by the high radial forces thereby increasing the distance between nucleation sites hence the constant grain size observed.

Grain growth rates with temperature for patterned substrates (inside and outside the channels) in Figure 4.18 reveal that grains grow faster inside than outside the channels as well as on the unpatterned substrates. Furthermore despite having the same growth rates, their different offsets of the respective lines on the graph indicate that grains inside the

channels at a particular temperature are greater than outside the channels. Two reasons are proposed for this observation.

Firstly planar (flat) surfaces, that is, the non-patterned substrates and the outside of the channels allow the HA sol to be swept by the radial forces due to the high speed spinning process hence leaving less sol on the surface. Conversely, for the inside channel, the walls of the channels provide a confinement to the sol despite the radial forces trying to drive it away. In addition to this, as evaporation during the spinning process proceeds subsequently increasing the viscosity, it seems the radial forces are not large enough to drive away all the sol out of the channels. More importantly, in addition to this, the channels also confine the nucleation sites, such that there are more sites per given area. As the temperature is increased, the grains grow and coalesce to form bigger ones because of them being close together in the channels.

Secondly, the patterns have larger surface areas than the flat areas hence these provide many sites for grain nucleation and growth than the flat surfaces (non-patterned and outside channels).

The calculation of crystallite sizes of HA fired at 850^{o}C from XRD spectra was calculated using the Scherrer formula [27] in equation 4.1.

$$d = \frac{0.9\lambda}{\Delta_{2\theta}\cos\theta} \tag{4.1}$$

Where d is the crystallite size, λ = 0.15404 nm for wavelength of Cu k_{α} X-rays and $\Delta_{2\theta}$ the full width at half maximum (FWHM) at angle 2θ. The results yielded 14.08 nm, 20.74 nm and 34.4 nm for the un-patterned, dry etched and wet etched substrates respectively. These are compared with AFM results as shown in Table 4.4.

Table 4. 4: Roughness and crystal size results of HA coatings fired at 850 ^{o}C Wet etched samples are rougher and hence have larger grain sizes than the dry etched and un-patterned samples.

	Roughness (AFM) and Crystal size (XRD)	
Sample	AFM results	XRD results
Un-pattered	3.32 nm	14.08 nm
Dry etched	9.40 nm	20.74 nm
Wet etched	16.64 nm	34.40nm

These results agree with the AFM results as it can be clearly seen that wet etched samples have larger grain sizes than the dry etched samples and the un-patterned samples in that order. As was pointed out earlier in the chapter, wet etched channels have tapered edges and hence offer enough surface area for nucleation than the sharp edged channels (dry etched). Due to larger surface areas offered by wet etched channels, the grains grow and coalesce to form large grains. This is the suspected reason why grains in wet etched substrates are larger than grains in dry etched substrates. The results show similar trend. This also gives some support to the method that was used in this thesis of correlating grain sizes with roughness. However, the sizes are as expected not the same from the two

measurement methods because XRD results are just averaged since there is a difference in distribution of sizes of grains on one sample as has been found from AFM results. In addition to this, the X-ray beam spans the whole patterned sample, not on one region only and so the crystallite size measurements are just averages. In addition to this, as has been alluded to earlier, the correlation of grain size and roughness in this study is only applicable to the smaller grains and not the larger grains. This is because only the sizes of smaller grains are comparable to the roughness and not the larger grains.

From a materials science perspective, the present study of the grain size distribution in fact seems to explain the results of Adams *et al*. [20], who found a marked, preferential and high density growth of osteoblasts inside the channels of the HA coated, geometrically configured titanium surfaces than outside of the channels. Since HA has a high affinity for osteoblasts, the many and large grains observed inside the channels attract the cells and also offer a better anchorage of the cells through their cytoskeleton filaments on the grains which is less on the flat surfaces. Additionally, the high roughness inside the channels provides enough surface area for anchorage of the cells. This makes sense since surface roughness has been found by many researchers to influence cell response [5].

Adams *et al.* [20] showed that patterned substrates have an influence on cell behaviour. They used orientation angle and form index as measures of cell response. The orientation angle is the measure of orientation of cells along the channels. The smaller the angle the more oriented the cells are. The results show that cells were more oriented on patterned substrates than the unpatterned substrates. This is shown in Table 4.5. Furthermore, form index (aspect ratio) which measures the elongation is in mathematical terms maximum length of the cell divided by the maximum width. The larger the value is, the more elongated the cell is. Similarly from these results, it was found that cells in patterned substrates had a larger form index than cells on the unpatterned substrates.

There is interestingly some consistence with the roughness results. The roughness value is higher for the patterned substrates than the unpatterned substrate. This shows a relationship between the effect of substrate geometry on cell response (in terms of orientation angle and form index) with roughness. These results show on a materials

level why among many factors there is a preferential growth and alignment of cells on well defined topography as explained above.

Table 4. 5: Table showing the relationship between cell behaviour and surface roughness.

	HA/Ti (patterned)	HA/Ti (Unpatterned)
Orientation angle [20]	13.94^{o}	43.27^{o}
Form Index [20]	3.19	2.3
Roughness (results of this study)	16.64 nm	3.28 nm

4.5 Conclusion

From this experiment, it has been established that RBS could not be used to conclusively indicate an effect of geometry on HA microstructure.

However, XRD and surface analysis techniques (SEM and AFM) offer a better way of characterizing the film on these geometrically configured substrates. Using atomic force microscopy and XRD, the following have been observed:

1. Geometrically configured substrates have an effect on the HA microstructure evolution. Patterned substrates have a marked effect on the grain growth of the

HA films on the substrates while the unpatterned substrates showed a constant grain size over the temperature range investigated

2. The grain size on the configured substrates is greater than the grains on the unpatterned substrates.
3. Surface roughness and grain size in the channels of the configured substrates are larger than that on the outside of the channels.
4. Wet etched surfaces have larger grains than the dry etched surfaces.

In light of the above, geometrically configured substrates have shown that they can be used to influence film roughness and grain size. This could have implications in the improvement of the bone/implant interface as the patterns would offer optimal HA crystallinity as well as roughness to provide better osteointegration and anchorage of bone cells to the patterned implant surface.

References

[1] Von Recum A.F., Shannon C.E., Cannon E.C., Long K.J., Van Kooten T.A., Meyle J., "Surface roughness, porosity and texture as modification of cellular adhesion," Tissue Engineering 2(1996)241-253

[2] Singhvi R., Stephanopoulos G., Wang D.I.C., "Review: Effects of substratum morphology on cell morphology," Biotechnol. Bioeng. 43(1994)764-771.

[3] Duncan A.C., Weisbuch F., Rouais F., Lazare S., Baquey C.H., "Laser micro-fabricated model surfaces for controlled cell growth," Biosensors and Bioelectronics 17(2002)413-426

[4] Boyan D.B., Hummert T.W., Dean D.D., Schwartz Z., "Role of material surfaces in regulating bone and cartilage cell response," Biomaterials 17(1996)137-146

[5] Anderson A.S., Olsson P., "The effects of continuous and discontinuous groove edges on cell shape and alignment," Experimental Cell Research 288(2003)177-188.

[6] Walboomers X.F., Croes H.J.E., Ginsel L.A., Jansen J.A., "Growth behaviour of fibroblasts o micro-grooved polystyrene," Biomaterials 19(1998)1861-1868

[7] Kaiser J.P., Reinmann A., Bruinink A., "The effect of topographic characteristics on cell migration velocity," Biomaterials 27(2006)5230-5241

[8] Dunn G.A., Heath J.P., "A new hypothesis of contact guidance in tissue cells," Experimental Cell Research 101 (1976) 1-14

[9] Rovensky Y.A., Slavnaya I.L., and Vasiliev J.M., "Behaviour of fibroblast-like cells on grooved surfaces," Experimental Cell Research 65(1971)193-201.

[10] Rovensky Y.A. and Slavnaya I.L., "Spreading of fibroblast like cells on grooved surfaces," Exp. Cell. Res., 84(1974)199-206.

[11] Maroudas N.G., "Growth of fibroblasts on linear and planar anchorages of limiting dimensions," Experimental Cell Research 81(1973)104-110.

[12] Brunette D.M., Kenner G.S., and Gould T.R.L., "Grooved titanium surfaces orient growth and migration of cells from human gingival explants." J Dent. Res. 62(1983)1045-1048.

[13] Chehroudi B., Gould T.R.L., Brunette D.M., "Effects of a grooved titanium-coated implant surface on epithelial cell behavior in vitro and in vivo." J Biomed Mater Res 23(1989)1067-1085.

[14] Den Braber E.T., de Ruijter J.E., Smits H.T.J., Ginsel L.A., von Recum A.F., and Jansen J.A., " Effect of parallel surface microgrooves and surface energy on cell growth,". J Biomed Mater Res 29(1995)511-518.

[15] Den Braber E.T., de Ruijter J.E., Smits H.T.J., Ginsel L.A., von Recum A.F., and Jansen J.A., "Quantitative analysis of cell proliferation and orientation on substrata with uniform parallel surface micro-grooves," Biomaterials 17(1996)1093-1099.

[16] Chesmal K.D. and Black J. "Cellular responses to chemical and morphologic aspects of biomaterial surfaces. A novel in vitro system," J Biomed Mater Res. 29 (1995) 1089-1099

[17] Meyle J., von Recum A.F., Gibbesch B., Huttemann W., Schlagenhauf U., and Schulte W., "Fibroblast Shape Conformation to Surface Micro-morphology," Journal of Applied Biomaterials, 2(1991)273-276.

[18] Curtis A., Wilkinson C., "Topographical Control of Cells," Biomaterials 18(1997)1573-1583

[19] Lenhert S., Meier M.B., Meyer U., Chi L., Wiesman H.P., Biomaterials 26 (2005) 563-570.

[20]. Adams D., Smith R.D., Malgas G.F., Massia S.P., Alford T.L., Mayer J.W., " The influence of Geometrically Configured Sol-Gel Derived Hydroxyapatite Substrates on Osteoblast Response," Key Engineering Materials 284-286 (2005)569-572

[21] Lopatin C.M., PhD thesis, Arizona State University, 1999

[22] JCPDS Card No. 9-432.

[23] http://www.memsnet.org/mems/processes/etch.html , Etching processes, (2007)

[24] Uhlmann D.R., Weinberg M.C, Teowee G., J. Non. Cryst. Solids 100(1988)154

[25] Brinker C.J., Scherer G.W., Sol-Gel science, Academic press, Boston, pgs 823-826,1990

[26] Brinker C.J., Scherer G.W., Sol-Gel science, Academic press, Boston, pg 334,1990

[27] Cullity B.D., Elements of Crystal Diffraction, Addison-Wesley Publishing Company, Philippines, 2nd Edition, pg 284, 1978

Chapter 5

Summary and Recommendations

5.1 Summary

Sol-gel derived HA was successfully developed using Lopatin's method [1] and deposited on metal substrates. Its crystallinity was confirmed by using XRD. The results from the research give a fundamental understanding on the surface properties of HA after plasma immersion implantation as well as when it is deposited on geometrically configured substrates.

The plasma immersion ion implantation (PIII) experiment was done in the quest to investigate the feasibility of PIII in improving adhesion resistance of HA on titanium substrates with a goal of improving the adhesion of HA on implants which is a common failure mode for implants. Tape test results from the experiment indicated that ion plasma treatment may increase the adhesion strength of HA on the implanted titanium substrates. Furthermore, densification was enhanced when HA was irradiated. However, irradiation disturbed the crystallinity as XRD results showed a diminishing of intensity of peaks of implanted HA.

The effects of geometrically configured substrates on HA microstructure evolution was investigated and this study proposes as one of the reasons from a materials science perspective why cells behave preferentially on micro-grooved substrates. XRD and AFM results showed that grain size increased with temperature. HA grains inside the micro-

channels were larger than outside the channels and on the planar substrates. The sizes were correlated from the roughness of the surfaces. The result proposes that these grains are the reason why cells grow more in channels than outside the channels.

In vivo, this roughness has an advantage as the asperities are able to retain clots and these are believed to be the medium in which cells migrate to the implant surface during the healing process [2]. Furthermore, the rough surfaces are believed to provide a greater surface area for protein adsorption and physical structures onto which fibrin clots can better attach. Finally it is also believed that the initial stability of an implant is more likely to be achieved with implants with rough surfaces and that the bone/implant interface shear strength correlates positively with the degree of surface roughness [3]. Therefore the present study has shed some light on how to achieve and apply all these through the combination of surface microfabrication and surface chemistry.

5.2 Recommendations

- Since cell response is dependent on the quality (crystallinity, porosity, density *etc*) of HA, a further characterization is needed with regard to the kinetics of HA at temperatures of 600-850 ^{o}C.
- Correlations of the present results of geometrical effects on HA properties with in vitro tests is needed.
- To provide an alternative method of HA deposition on titanium substrates, titanium need to be plasma implanted to provide surface energy for the spontaneous nucleation of calcium phosphates after incubation in simulated body fluid.
- Since bone cells are known to be mechano-sensitive, Finite element modeling is needed to simulated stress fields on different geometries and sizes with a goal of optimizing cell response.

References

[1] Lopatin C.M., PhD thesis, Arizona State University, 1999

[2] Davies J.E., "Mechanism of Endosseous Integration," Int. J. Prosthodont. 11(1998)391-401

[3] Lee T.Q., *et al.,* "Initial stability comparison of modular hip implants in synthetic femurs," Orthopedics 21(1998)885